JOURNAL OF GEOPHYSICAL RESEARCH, VOL. 98, NO. B12, PAGES 21,677–21,712, DECEMBER 10, 1993

Space Geodetic Measurement of Crustal Deformation in Central and Southern California, 1984–1992

KURT L. FEIGL,[1,2] DUNCAN C. AGNEW,[3] YEHUDA BOCK,[3] DANAN DONG,[1,4] ANDREA DONNELLAN,[4,5]
BRADFORD H. HAGER,[1] THOMAS A. HERRING,[1] DAVID D. JACKSON,[6] THOMAS H. JORDAN,[1]
ROBERT W. KING,[1] SHAWN LARSEN,[5,7] KRISTINE M. LARSON,[3,8] MARK H. MURRAY,[1,9]
ZHENGKANG SHEN,[6] AND FRANK H. WEBB[4,5]

We estimate the velocity field in central and southern California using Global Positioning System (GPS) observations from 1986 to 1992 and very long baseline interferometry (VLBI) observations from 1984 to 1991. Our core network includes 12 GPS sites spaced approximately 50 km apart, mostly in the western Transverse Ranges and the coastal Borderlands. The precision and accuracy of the relative horizontal velocities estimated for these core stations are adequately described by a 95% confidence ellipse with a semiminor axis of approximately 2 mm/yr oriented roughly north-south, and a semimajor axis of approximately 3 mm/yr oriented east-west. For other stations, occupied fewer than 5 times, or occupied during experiments with poor tracking geometries, the uncertainty is larger. These uncertainties are calibrated by analyzing the scatter in three types of comparisons: (1) multiple measurements of relative position ("repeatability"), (2) independent velocity estimates from separate analyses of the GPS and VLBI data, and (3) rates of change in baseline length estimated from the joint GPS+VLBI solution and from a comparison of GPS with trilateration. The dominant tectonic signature in the velocity field is shear deformation associated with the San Andreas and Garlock faults, which we model as resulting from slip below a given locking depth. Removing the effects of this simple model from the observed velocity field reveals residual deformation that is not attributable to the San Andreas fault. Baselines spanning the eastern Santa Barbara Channel, the Ventura basin, the Los Angeles basin, and the Santa Maria Fold and Thrust Belt are shortening at rates of up to 5 ± 1, 5 ± 1, 5 ± 1, and 2 ± 1 mm/yr, respectively. North of the Big Bend, some compression normal to the trace of the San Andreas fault can be resolved on both sides of the fault. The rates of rotation about vertical axes in the residual geodetic velocity field differ by up to a factor of 2 from those inferred from paleomagnetic declinations. Our estimates indicate that the "San Andreas discrepancy" can be resolved to within the 3 mm/yr uncertainties by accounting for deformation in California between Vandenberg (near Point Conception) and the westernmost Basin and Range. Strain accumulation of 1–2 mm/yr on structures offshore of Vandenberg is also allowed by the uncertainties. South of the Transverse Ranges, the deformation budget must include 5 mm/yr between the offshore islands and the mainland.

INTRODUCTION

Determining the velocity field in the vicinity of the Pacific-North America plate boundary in central and southern California (Figure 1) is a long-standing problem in tectonics. While most of the motion between these plates occurs on the San Andreas fault, the deformation extends for a substantial distance on either side of this structure. Such off-fault deformation is evident in geologic structures, seismicity, paleomagnetic declinations, and geodetic networks. Measuring that deformation with space geodesy is the primary objective of this study, which seeks to quantify the velocity field in this intercontinental plate boundary zone.

Geological and Seismological Indicators

Deformation in the southern Coast Ranges (SCR in Figure 1) is characterized primarily by strike-slip motion on the San Andreas, Hosgri, Rinconada, and other parallel faults [e.g., *Dibblee*, 1977]. Away from the San Andreas fault (SAF), the deformation includes a compressional component oriented perpendicular to the trace of the SAF as evidenced by subparallel fold axes [*Page*, 1966, 1981] and thrust faulting earthquake focal mechanisms [*Dehlinger and Bolt*, 1988]. The rate of shortening has been estimated at 7–13 mm/yr from a balanced cross section extending from the SAF to an offshore point west of the Hosgri fault [*Namson and Davis*, 1990]. On the other (northeast) side of the SAF, there is also evidence of compressional strain, notably the anticlinal structures associated with oil production [*Callaway*, 1971] and the 1983 Coalinga earthquake [*Stein and King*, 1984].

Farther south, the part of the Santa Maria Basin to the northeast of Point Arguello forms a tectonic transition zone between probable strike-slip motion on the San Gregorio-Hosgri fault system [*Hall*, 1978, 1981], and compression in the western Transverse Ranges (WTR) and Santa Barbara Channel (SBC) to the south [*Crouch et al.*, 1984; *Namson and Davis*, 1990].

The Santa Barbara Channel is undergoing north-south shortening, as indicated by earthquake focal mechanisms [*Yerkes and Lee*, 1979] and geological investigations of folding and faulting [*Yeats*, 1981, 1983]. The average rate of shortening is 2–9 mm/yr, estimated from 1.8 km over the last 0.2–1.0 m.y. [*Yeats*, 1983].

There is substantial deformation of Quaternary structures accommodating convergence across the Transverse Ranges. For example, *Namson and Davis* [1988] propose an average conver-

---

[1] Department of Earth, Atmospheric and Planetary Sciences, Massachusetts Institute of Technology, Cambridge.

[2] Now at Centre National de Recherche Scientifique, Toulouse, France.

[3] Institute of Geophysics and Planetary Physics, Scripps Institution of Oceanography, La Jolla, California.

[4] Now at Jet Propulsion Laboratory, Pasadena, California.

[5] Seismological Laboratory, California Institute of Technology, Pasadena.

[6] Department of Earth and Space Sciences, University of California, Los Angeles.

[7] Now at Lawrence Livermore National Laboratory, Livermore, California.

[8] Now at Department of Aerospace Engineering, University of Colorado, Boulder.

[9] Now at U.S. Geological Survey, Menlo Park, California.

Paper number 93JB02405.
0148-0227/93/93JB-02405$05.00

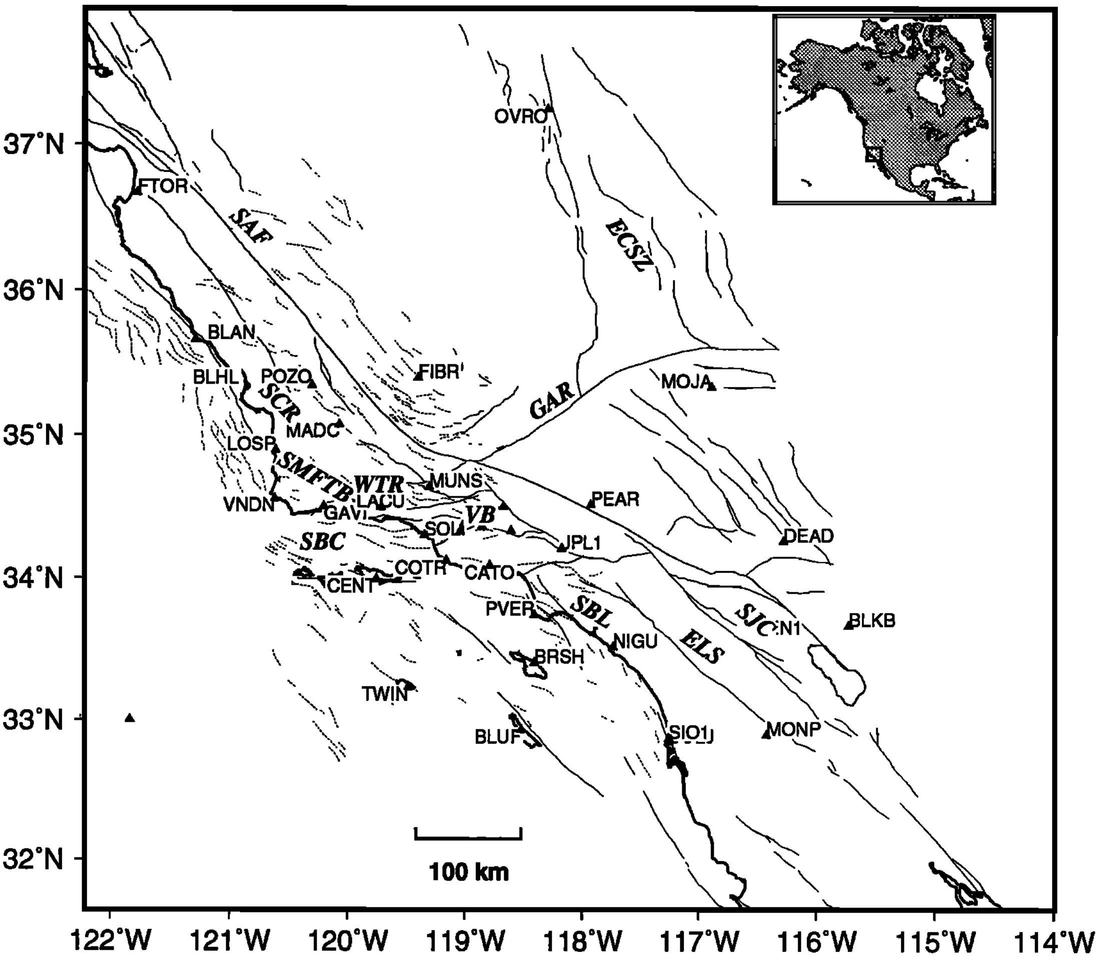

Fig. 1. Generalized map of California showing traces of major Quaternary faults (solid lines) and Neogene fold axes from *Stein and Yeats* [1989] (dashed lines). The GPS stations (triangles) are labeled with the four-character codes listed in Table 1. The tectonic domains (in italics) include the Santa Maria Fold and Thrust Belt (SMFTB), the southern Coast Ranges (SCR), the western Transverse Ranges (WTR), the Ventura Basin (VB), the Santa Barbara Channel (SBC), the southern Borderlands (SBL), and the Eastern California Shear Zone (ECSZ). Major faults include the San Andreas (SAF), the Elsinore (ELS), San Jacinto (SJC), and the Garlock (GAR). Stations not labeled here are labeled in Figures 5 and 6.

gence rate of 18–27 mm/yr over the past 2–3 m.y. for a cross section between Ventura and the White Wolf fault in the Great Valley. *Yeats* [1983] proposes accelerated deformation near Ventura during the past 0.2 m.y. with 22 mm/yr occurring across this region of the Ventura basin alone.

In the region between Ventura and Los Angeles, *T. L. Davis et al.* [1989] find convergence rates south of the SAF of 8–16 mm/yr. Along the frontal fault of the San Gabriel Mountains (between VB and JPL1 in Figure 1), *Weldon and Humphreys* [1986] conclude that the rate of convergence is negligible, while *Bird and Rosenstock* [1984] propose convergence rates of the order of 10 mm/yr.

The deformation in the Borderlands south of the Santa Barbara Channel is much less well known. The overall structural grain and most earthquake slip vectors trend northwest to southeast [*Bent and Helmberger*, 1991], but the July 1986 Oceanside earthquake [*Hauksson and Jones*, 1988; *Pacheco and Nábělek*, 1988] and the San Clemente fault [*Legg et al.*, 1989] do not fit this pattern.

Although the San Andreas fault is generally considered to be the major seismic hazard in this region (indeed, it ruptured in a major ($M = 7.8$) earthquake in 1857), most of the seismic moment release in this century has not been associated with rupture of the SAF [*Ellsworth*, 1990]. This is apparent in the map of all events of magnitude (M_L) greater than 4.0 in the past 60 years (e.g., Figure 4 of *Hutton et al.* [1991]). Between 1812 and 1987, four large earthquakes contribute 70% of the moment release to produce an average slip rate of 17–20 mm/yr [*Ekström and England*, 1989]. Of these four events, two, the 1872 Owens Valley ($M_w = 7.5$–7.7) and the 1952 Kern County ($M_w = 7.3$–7.5) earthquakes, were not associated with the San Andreas fault [*Ellsworth*, 1990]. The recent Landers ($M_w = 7.3$) earthquake [*Sieh et al.*, 1993] provides another example of substantial seismic moment release not associated with the SAF.

Large (approximately 30°) paleomagnetic declinations observed in post-Miocene rocks in the western Transverse Ranges suggest clockwise rotations about vertical axes [*Luyendyk*, 1991]. When averaged over the last 5 to 20 m.y., these data imply rotation rates of the order of 6°/m.y. (0.1 μrad/yr), which can be explained by models that accommodate simple shear on rotating blocks [*Luyendyk*, 1991] or by "bookshelf" or "collapsing ladder" faulting [*Jackson and Molnar*, 1990]. Although these models invoke finite rotations over several million years, the instantaneous rate of rotation appears to be of the same order of magnitude [*Jackson and Molnar*, 1990] and can be resolved by our geodetic network.

The San Andreas Discrepancy

While there is abundant evidence for regional deformation off the SAF, the most quantitative argument is the deviation from the vector equality required by rigid plate tectonics [*Minster and Jordan*, 1984]. The starting point is the vector velocity of the Pacific plate with respect to the North America plate, which represents the integrated rate of deformation across the "wide, soft boundary" [*Atwater*, 1970] separating the two tectonic plates. From this vector, one subtracts a vector for the direction and rate of slip on the SAF in central California. The resulting nonzero vector has been named the "San Andreas discrepancy" [*Minster and Jordan*, 1984]. A large part of this residual motion may be explained by extension in the Basin and Range Province [*Minster and Jordan*, 1987], estimated from very long baseline interferometry (VLBI) to be 9 ± 1 mm/yr at N29 ± 4°W [*Argus and Gordon*, 1991]. Subtracting this value from the "discrepancy" yields a remainder (the "modified discrepancy") estimated to be 6 ± 2 mm/yr at N20 ± 17°W [*Argus and Gordon*, 1991]. This motion must be accommodated to the west of the Basin and Range, most likely in onshore California [*Sauber*, 1988; *Argus and Gordon*, 1990; *Savage et al.*, 1990; *Ward*, 1990].

The discrepancy is reduced by an additional 2 mm/yr when recent revisions in the magnetic time scale are taken into account. The current plate motion model, NUVEL-1 [*DeMets et al.*, 1990], averages velocities over the time since the normally magnetized chron in the 2A sequence of paleomagnetic anomalies, taken to be at 3.03 Ma in the time scale of *Harland et al.* [1982]. Recent revisions in the time scale suggest that this chron is several percent older [*Hilgren*, 1991; *McDougall et al.*, 1992; *Cande and Kent*, 1992]. A reasonable approach is to use an average value of 3.16 Ma from these three studies, which means that the NUVEL-1 rates must be scaled by a factor of 0.959 (C. DeMets, personal communication, 1993). Throughout the rest of this paper, we shall use these slower rates and refer to them as "rescaled NUVEL-1."

Previous Geodetic Studies

The triangulation networks established along the California coast in the late 1800s form the basis of much of the subsequent geodetic work [*Bowie*, 1924; 1928]. Resurveys led to the eventual detection of a "slow drift" of roughly 50 mm/yr of the crust west of the SAF [*Whitten*, 1956]. The historical survey data have been used to infer dextral angular (engineering) shear strain rates of at least 0.2 μrad/yr for most of the western Transverse Ranges [*Snay et al.*, 1983, 1986, 1987]. Many of these historical stations have been reoccupied with the Global Postioning System (GPS) as part of our study.

Trilateration networks monitored by the U.S. Geological Survey (USGS) straddle the major segments of the SAF system. As summarized by *Lisowski et al.* [1991], the velocity field determined by trilateration in central and southern California is dominated by right-lateral shear associated with the SAF system. Indeed, they can explain all the deformation observed in their networks by shear alone, requiring remarkably little dilatation. Observed changes in line lengths in the USGS networks have been modeled as due to strike-slip motion on dislocations buried at depths of tens of kilometers beneath the major faults. Inferred displacement rates for the SAF north of the Big Bend are 32–36 mm/yr [*Eberhart-Phillips et al.*, 1990; *Lisowski et al.*, 1991], consistent with the geological inference of 34 mm/yr [*Sieh and Jahns*, 1984]. Given the success of these models, the shear component of the SAF motion in central California may be regarded as a relatively well-understood signal.

Using VLBI, *Clark et al.* [1987] estimated that the velocity of Vandenberg with respect to Mojave was some 7 mm/yr slower than the 48 mm/yr predicted by the NUVEL-1 plate motion model [*DeMets et al.*, 1990]. This result implied deformation offshore of Vandenberg or east of Mojave. By excluding Mojave from the stable North America plate, *Ryan et al.* [1993] estimated the motion of Vandenberg relative to the North American plate to be within 1 mm/yr of the value predicted by the rescaled NUVEL-1. VLBI data also allowed *Ward* [1990] to attribute approximately 6 mm/yr to deformation in the Coast Ranges, west of the SAF. Since this motion is northward with respect to North America, it would appear to include a fault-normal component as well as right-lateral shear.

The southern Coast Ranges are actively deforming, as has been observed by triangulation [*Savage and Burford*, 1973], trilateration [*King et al.*, 1987], and a comparison of triangulation and GPS [*Shen*, 1991; *Shen and Jackson*, 1993]. Most of this motion appears to be right-lateral shear describable by a simple model of a dislocation in the plane of the fault [e.g., *Lisowski et al.*, 1991]. Other models, allowing motion normal to the fault [*Harris and Segall*, 1987; *Segall and Matthews*, 1988], additional tectonic blocks [*Cheng et al.*, 1987] or time dependence [*Li and Rice*, 1987], suggest that the deformation away from the San Andreas is more complex than simple shear from constant slip on a buried screw dislocation.

Another deviation from simple shear occurs in the western Transverse Ranges, where several geodetic studies have measured active compression. In the area south of Santa Maria, a significant component of compression has been estimated from a comparison of historical triangulation surveys [*Bowie*, 1924, 1928; *Savage and Prescott*, 1978] with GPS observations [*Feigl et al.*, 1990; *Shen and Jackson*, 1993]. The Santa Barbara Channel is also actively shortening, as shown by comparisons of GPS data with historical triangulation measurements [*Webb*, 1991] and 1970s trilateration [*Larsen*, 1991; *Larsen et al.*, 1993]. In the Ventura basin, comparison of GPS observations in 1987 with triangulation from the 1950s has measured rapid shortening [*Donnellan*, 1992; *Donnellan et al.*, 1993a], but at rates less than half the geological estimates for the last 0.2 m.y. [*Yeats*, 1981, 1983].

Our Geodetic Studies

GPS and VLBI observations, especially when combined, offer several advantages over classical terrestrial techniques. First, they retain high precision (less than 10^{-7}) over lines longer than 30 km. Second, they measure the Cartesian vector between two stations rather than the distance or direction only. Third, they measure with respect to a single reference frame. Taken together, these improvements in geodetic technique allow us to estimate a precise, self-consistent relative velocity field over most of central and southern California.

The southwest United States has been the ideal location to study tectonic motions with GPS measurements [*Dixon*, 1991; *Hager et al.*, 1991] because the Department of Defense optimized the initial (Block I) satellite constellation to provide the best accuracy for testing in this region. Measurements made in California as early as June 1986 have shown both short-term repeatability and agreement with VLBI for horizontal coordinates at the sub-centimeter level for intersite distances up to 400 km [*Dong and Bock*, 1989; *Blewitt*, 1989; *J. L. Davis et al.*, 1989; *Dixon et al.*, 1990; *Larson and Agnew*, 1991; *Murray*, 1991]. This accuracy implies that we can determine velocities at the level of a few millimeters per year in 5 years with annual measurements. The sites for which we determine velocities using repeated GPS and VLBI are shown in Figure 1. The following section describes the techniques for collecting the various types of data: VLBI from the global network, GPS in the California region, and GPS at globally distributed stations.

DATA

Between 1984 and 1992, over 1700 VLBI experiments were performed using a global array of radio telescopes [*Clark et al.*, 1985] under the sponsorship of the National Aeronautics and Space Administration (NASA) [*Coates et al.*, 1985] and the National Oceanic and Atmospheric Administration (NOAA) [*Carter et al.*, 1985]. Our analysis includes 1618 of these experiments, described by *Ryan et al.* [1993]. About 170 of these experiments have included at least one fixed and one mobile antenna in central or southern California.

Most of the GPS observations used in our analysis were obtained in over 20 experiments between 1986 and 1992. Twelve stations make up the "core" network extending along the California margin from San Simeon to San Clemente Island (Figure 1). These core sites, listed in Table 1, were all occupied at least five times in the 5 years. During the six experiments involving the core network, GPS receivers also occupied three or more VLBI sites within California to provide a regional anchor for the network. In addition to the core experiments, we also conducted more than a dozen smaller experiments to increase the spatial density of the network in regions of tectonic interest. These small experiments often included sites also measured by VLBI, trilateration, or historical triangulation. A complete list of stations with identifying codes and approximate positions is given in Table 1. The field experiments are listed in Table 2. The configurations of the tracking sites available for each experiment are listed in Table 3.

Between 1986 and 1989, all of the field observations were made using Texas Instruments (TI) 4100 receivers; between 1990 and 1992, most were made using Trimble 4000 SST receivers. As part of our March 1990 campaign, we occupied seven stations with both TI 4100 and Trimble receivers in two successive 4-day experiments. The receivers used at the permanent tracking stations were more diverse and changed over time (Table 3). They included TI 4100, MiniMac 2816AT, Trimble 4000 SST, and Rogue SNR-8 receivers.

Altogether, the GPS data set includes useable observations for over 100 days between June 1986 and May 1992. Subsets of these data are described in detail in several preliminary analyses. Experiment 0 is described by *Blewitt* [1989] and *Dixon et al.* [1990], and experiment 3 by *Dong and Bock* [1989]. The first 2.7 years of data in experiments 0, 2, 7, 8, 11, and 14 are analyzed by *Larson* [1990a,b]. This analysis is extended to include a 1991 occupation of several sites in the Channel Islands (experiment SB1) by *Larson and Webb* [1992] and *Larson* [this issue]. Details on the occupations of specific sites are given by *Murray* [1991] for the core sites, by *Donnellan* [1992] and *Donnellan et al.* [1993a] for the Ventura basin, by *Feigl* [1991] for Vandenberg, by *Shen* [1991] for the Coast Ranges, and by *Larson* [1990a] and *Larsen* [1991] for the Channel Islands.

To improve the accuracy of the coordinates of the global GPS tracking sites used to analyze the California campaigns, we also include data from two additional GPS data sets. A global GPS campaign was conducted for 23 days in January–February 1991 under the auspices of the International Earth Rotation Service (IERS) with the coordination of the Jet Propulsion Laboratory (JPL). We analyze the data obtained from the 21 Rogue receivers, which provide a sufficiently strong global network to improve significantly the coordinates of six of the sites (Algonquin, Tromso, Wettzell, Kokee, Scripps, Pinyon, and JPL) used in our California experiments [*Herring et al.*, 1991; *Blewitt et al.*, 1992]. In addition, we have included 119 days of data obtained between October 1991 and May 1992 from 35 global sites as part of the operations of the Permanent GPS Geodetic Array (PGGA) in California [*Bock and Shimada*, 1990; *Bock*, 1991; *Lindqwister et al.*, 1991; *Blewitt et al.*, 1993; *Bock et al.*, 1993]. Four of the global sites (Algonquin, Tromso, Wettzell, and Kokee) and three PGGA sites (Scripps, Pinyon, and JPL) were also observed during several occupations of the core network.

DATA ANALYSIS

We analyze the GPS and VLBI observations in two steps. In the first step, we perform separate least squares analyses of the GPS phase and VLBI group delay data in each individual day ("session"). In these single-session solutions, we estimate the sta-

TABLE 1. List of Stations

ID	PID^a	Stamping or Location^b	Lat°N	Lon°W	Height^c, m
ALAM	DZ1334	ALAMO 1925	34.7985	120.2568	460
ALVA	DZ1732	ALVADO 1933	34.5927	120.6170	290
BLAN^d	FV1009	NAVY DEPT 12 NAVAL DISTRICT	35.6646	121.2845	-25
BLHL^d		BLACK HILL 1881 (R.M)	35.3587	120.8317	170
BLUF^d	TZ1974	BLUFF 1933, San Clemente Island	32.9268	118.5185	300
BOLD	TZ1946	BOULDER 1933	32.8958	118.4682	560
BOUC	DX5081	BOUCHER 2 1975	20.3347	116.9193	1660
BPA3		BP ARIES 3, Owens Valley Radio Obs	37.2320	118.2836	1180
BRSH	DY2150	BRUSH 1876, Catalina Island	33.4070	118.4049	450
CATO		Castro Peak	34.0858	118.7858	830
CATW		Catalina Island West	33.4598	118.5687	510
CENT^d	DY3159	CENTER 1934, Santa Cruz Island	33.9948	119.7529	390
CHAF	EW7861	CHAFFEE 2 1923 1941	34.3006	119.3310	310
COTR	EW6129	Cotar, Pt. Mugu	34.1202	119.1540	-30
CSTL	FV1421	Castle Mount	35.9389	120.3403	1330
DEVL	EW8070	DEVILS PEAK 2 1951, Santa Cruz Island	34.0291	119.7844	700
ECHO	EW7224	ECHO ROCK C. A.	34.2249	118.0550	1720
ELMO	EW7230	MERCED R. S. 1923 NO. 4 1972	34.0302	118.0951	180
FIBR^d	FU1972	A 364 1953, Buttonwillow	35.3985	119.3940	50
FTOR		NASA GSFC 7266, Ft. Ord	36.6698	121.7733	20

TABLE 1. (continued)

ID	PID	Stamping or Location	Lat°N	Lon°W	Height, m
FOR0		NASA GSFC 7421 1990, Ft Ord	36.5894	121.7721	250
FOR2		NASA GSFC 7421 RM2, Ft. Ord	36.5897	121.7716	250
GAVI	DZ1256	Gaviota	34.5018	120.1988	710
GRAS	DZ1327	GRASSY USGS 1959	34.7306	120.4141	330
HAPY		HAPPY 1959	34.3580	118.8501	670
HAP2		HAPPY2 1992	34.3280	118.8771	330
HOPP		HOPPER 1941	34.4777	118.8655	1340
JPLM		Mesa, JPL, Pasadena (PGGA)	34.2048	118.1732	420
JPL1	EW1949	JPL1 ARIES 1 1975, Pasadena	34.2047	118.1710	440
LACU[d]	EW8022	La Cumbre, Santa Barbara	34.4944	119.7139	1160
LIND		BUREAU OF RECLAM LINDA 1955	34.9599	120.2997	180
LOSP[d]	DZ1559	Mt. Lospe, Vandenberg AFB	34.8937	120.6062	460
LOVE		LOMA VERDE RESET 1961	34.4963	118.6687	730
MADC[d]		MADRE ECC 1980	35.0756	120.0671	960
MILL	DZ1261	MILLER 1974	34.5101	120.2297	90
MOJ1	FT1572	NCMN 1983 RM 1, Mojave Station	35.3316	116.8908	930
MOJA[d]		TI 4100 phase center, Mojave Station	35.3316	116.8882	900
MOJF		FRPA-1 phase center, Mojave Station	35.3316	116.8882	900
MOJM		MiniMac phase center, Mojave Station	35.3316	116.8882	900
MONU	DC1438	MONUMENT PEAK NCMN 1983	32.8918	116.4228	1840
MPNS		MT PINOS USC&GS 1941	34.8128	119.1454	2660
MUNS		MUNSON (TPC) (USCE) 1971	34.6358	119.3006	2110
NIGU	DX5266	NIGUEL A 1884 1981	33.5145	117.7303	240
OCOT	DB1234	OCOTILLO NCMN 1982	32.7901	115.7962	0
OVRO		MOBLAS 7114 1979, Owens Valley R. O.	37.2326	118.2938	1180
PARG	DZ1175	PT ARGUELLO 1933	34.5549	120.6160	-10
PEAR		Pearblossum NCMN 1983	34.5121	117.9224	890
PINY	DX3617	PINYON FLAT NCMN 1981	36.6092	116.4588	1270
PIN1		Pinyon 1 PGGA	33.6122	116.4582	1260
PIN2		Pinyon 2 PGGA	33.6121	116.4576	1260
PL9A	EW7395	PICO L 9 A 1967	34.3295	118.6007	1100
POZE	FV0810	K 66 1927	35.3474	120.2955	770
POZO	FV0811	L 561 1957	35.3460	120.2987	730
PTDU	EW4215	POINT DUME RESET 1947	34.0016	118.8067	60
PVER[d]		PALOS VERDES ARIES 1976 1980	33.7438	118.4036	70
ROKY	FV1829[e]	Rocky Butte 2, RM 1	35.6653	121.0596	1050
RUS1	DZ1778[e]	RUSTAD 1933 RM1	34.5708	120.6270	180
SAFE		PICO L 9 C	34.3304	118.6013	1100
SBA2	EW7997	SANTA BARBARA 2 1956, S. Barbara Is.	34.4041	119.7160	140
SBIS	DY3066	SANTA BARBARA ISD 2 1940	33.4721	119.0413	160
SCLA		SANTA CLARA 1898	34.3257	119.0392	660
SCRE	EW8055	Santa Cruz East	34.0547	119.5647	60
SCRW	EW8085[e]	Santa Cruz West 2, RM 1	34.0732	119.9180	180
SIO1	DC2121	Scripps 1 PGGA	32.8678	117.2523	10
SIO2		Scripps 2 PGGA	32.8675	117.2524	10
SIVP		Sierra Vista Park	34.0660	118.0120	90
SJOS	FV1440	SAN JOSE 1884 1956	35.3152	120/2696	1150
SJUA	DX4280	San Juan (1886)	33.9138	117.7381	540
SLUI	FV1464	San Luis	35.2778	120.5618	870
SMIG	DZ1512[e]	NEW SAN MIGUEL RM 2 1934	34.0396	120.3866	210
SNPA	EW7538	SANTA PAULA NCMN 1981	34.3879	118.9988	180
SNP2		SANTA PAULA 1941	34.4404	119.0096	1480
SNRI	DZ1207	SOLEDAD 1872 1934, Santa Rosa Island	33.9509	120.1057	440
SNTZ		LA COUNTY COVINA C7 RM NO 1	34.0125	117.8837	360
SOLI	EW7886	SOLIMAR 1974	34.2983	119.3427	-10
SOLJ	DC1849	Mt Soledad, La Jolla	32.8399	117.2525	220
SYNZ		SANTA YNEZ 11917 1990 CSG DET 1	34.5305	119.9860	1220
TEPW		Tepusquet Witness	34.9100	120.1867	950
TWIN	DY2177	TWIN 964, San Nicholas Island	33.2318	119.4790	200
VAND		VLBI STA 7223, Vandenberg AFB	34.5561	120.6164	-10
VNDN[d]		VLBI STA 7223 RM 1 1983 DET 1 GSS	34.5563	120.6162	-10
VSLR		TLRS STA 7880 Vandenberg AFB	34.5560	120.6164	-10
VICE	DY1011	E 788 1946	33.7419	118.4107	40
WHIT		Whitaker Peak	34.5674	118.7428	1220
WHT3		Whitaker Peak	34.5675	118.7427	1220
WORK	DY0230[e]	WORKMAN HILL RESET 1978	33.9917	118.0029	420
YAM2		USGS ELEV 2749 FT	34.8525	119.4844	810
YUMA		Yuma (Arizona) NCMN 1983	32.9391	114.2031	238

[a] PID is the "Permanent IDentification" number assigned by the National Geodetic Survey.

[b] Stampings are listed in uppercase; lower or mixed case gives location or description.

[c] Coordinates are geodetic with respect to the NAD 83 ellipsoid.

[d] Core site.

[e] A reference mark (RM) has been used and the PID refers to the main monument.

TABLE 2. List of Experiments

Exp.	Dates	Days	Rcvrs	Area or Objective	California Sites Observed						
0	Jun. 1986	4		VLBI sites and	BLUF	BOLD	BOUC	CATW	HATC	LAJO	MACA
				Channel Islands	MOJ1	MONU	NIGU	OTAY	PINY	PVER	SANT
					SOLJ	TWIN	VNDN	YUMA			
1	Dec. 1986	5	9	Greater Los	BLHL	FTOR	LOSP	MOJA^a	OVRO	POZO	POZE
				Angeles Basin	PVER	SNPA	VNDN				
2	Jan. 1987	5	12	core network	BLAN	BLHL	CENT	COTR	FIBR	FTOR	LACU
					LOSP	MADC	MOJA	OVRO	VNDN		
3	Jan. 1987	5	12	Historical and	BRSH	CHAF	DEVL	FIBR	FTOR	GAVI	LACU
				core sites	MILL	MOJA	OVRO	PVER	SNRI	SOLI	VNDN
					VSLR						
4, 5, 6	Jan. 1987			VLBI sites	BLAC^a	COTR^a	LACU^a	MONU^a	NIGU^a	OCOT^a	PEAR^a
					PINY^a	PVER^a	SAND^a	SOLJ^a	YUMA^a		
7	May 1987	4	6	central network	BLHL	CENT	MOJA	OVRO	PVER	VNDN	
8	Sep. 1987	4	7	central network	BLHL	CENT	FTOR	MOJA	OVRO	PVER	SCRE
					SCRW	VNDN					
9	Sep. 1987		7	historical sites	CHAF^a	CSTL^a	DEVL^a	ECHO^a	ELMO^a	GRAS	MOJA
					NIGB^a	PVER	SBA2^a	SJUA^a	SLUI^a	SOLI^a	TEPT
					TEPW	VNDN					
				Los Angeles and	CATO	DELT^a	ECHO^a	ELMA^a	ELMO^a	HAPY	HOPP
				Ventura Basins	LOVE	MOJA	PTDU^a	PVER	SAFE	SCLA	SIVP^a
					SNP2	SNTZ^a	VICE^a	WORK^a			
10	Mar. 1988	4		Channel Islands	BLUF	BRSH	CENT	MOJA	NIGU	PVER	SBIS
					SMIG	SOLJ	VNDN				
11	Mar. 1988	4	12	core network	BLAN	BLHL	CENT	FIBR	FTOR	LACU	LOSP
					MADC	MOJA	OVRO	PVER	TWIN	VNDN	
12	Mar. 1988	4		VLBI sites	BLAC^a	BOUC^a	JPL1^a	MACA^a	MOJA^a	MONU^a	PEAR^a
					PINY^a	SNPA^a	YUMA^a				
13	Mar. 1989	4		Channel Islands	BLUF	BRSH	MOJF	MOJM	NIGU	PVER	SOLJ
					TWIN	VNDN					
14	Mar. 1989	4	11	core network	BLAN	BLHL	CENT	FIBR	JPL1	LACU	LOSP
					MADC	MOJF	MOJM	OVRO	PVER	VNDN	
15	Apr. 1989	3	4	Santa Maria Basin	GAVI	GRAS	MILL	MOJM	PARG	VNDN	
16	Apr. 1989	3		Ventura Basin	CATO	HOPP	MOJF	MOJM	MUNS	PVER	SAFE
					SNPA	YAM2					
VF1	Feb. 1990	10	2	Santa Maria Basin	ALAM	ALVA	GAVI	GRAS	LOSP	MOJM	RUS1
					SYNZ	VNDN					
17	Mar. 1990	4	7	core network	BLHL	CENT	JPL1	MADC	MOJA	OVRO	PVER
				(TI 4100)	VNDN						
18	Mar. 1990	4	17	core network	BLAN	BLHL	BLUF	BPA3	BRSH	CENT	CEN1^a
				(Trimble)	CEN2	CEN3	FIBR	FOR0	FOR2	JPL1	LACU
					LOSP	MADC	MOJM	OVRO	PIN2	PVER	SIO2
					VNDN						
VB1	Jun. 1990	9	6	Ventura Basin	CATO	COTR	HAPY	HOPP	LACU	LOVE	MPNS
					MOJM	MUNS	PL9A	PVER	SAF3	SAFE	SCLA
					SNP2	SNPA	SOLI	WHIT	YAM2		
VF2	Sep. 1990	14	3	Santa Maria Basin	ALAM	ALVA	GAVI	GRAS	LIND	LOSP	MADC
					MOJM	RUS1	VNDN				
20	Feb. 1991	4	16	core network	BLAN	BLHL	BLUF	BRSH	CENT	FIBR	LACU
					LOSP	MADC	MOJM	NIGU	OVRO	POZO	PVER
					SOLI	TWIN	VNDN				
SB1	Jun. 1991	4	8	Channel Islands^b	CENT	DEVL	GAVI	LACU	MOJM	OVRO	PIN1
					PVER	ROCH	SIO1	SNRI	SOLI	VAND	VNDN
VB2	May 1992	7	15	Ventura Basin	CATO	GOLD	HAP2	HAPY	HOPP	JPLM	LACU
					LOVE	MOJM	MPNS	MUNS	PIN1	PVER	SAFE
					SIO1	SNPA	SNP2	SOLI	WHT3	YAM2	

a Site observed but not included in the solutions.

b SB1 included 22 Caltrans sites not listed.

tion coordinates, atmospheric parameters, Earth orientation parameters (for VLBI), orbital elements (for GPS), and phase ambiguities (for GPS). In the second step, we estimate station velocities in "multisession" solutions which combine the estimates and covariance matrices from all sessions. Station coordinates and orbital parameters are also estimated in the multisession solutions in a consistent and non-redundant manner.

As detailed in the appendix, this two-step process has two advantages. First, it allows us to handle the data easily. The single-day solution condenses the information in the large (up to 1 Mbyte/station/day) data set into a few compact files which may then be used to perform multisession solutions easily and quickly. Second, it affords a rigorous solution to the problem of an inhomogeneous tracking network, where the set of stations changes from day to day and year to year. Since this ("fiducial") network determines the frame to which the estimated vectors are referred, naively comparing a vector estimated on two days with different networks can lead to an inaccurate estimate of its rate of change. The magnitude of the error can reach 1 part in 10^7 for the early observations of our network [*Larson et al.*, 1991]. As discussed in the appendix, our approach minimizes the effect of the shifting fiducial geometry by imposing the constraints on the coordinates in a consistent manner. This is particularly important for GPS tracking stations that have been used only a few times.

TABLE 3. Global Tracking Sites

Experiment	Date	KOKE	PENT	YKNF	PLAT	FTDV	AUST	CHUR	RICH	ALGO	WSFD	WETT	TROM	ONSA	TSUK
0	Jun. 1986					•			•		•				
1	Dec. 1986				•		•								
2	Jan. 1987				•		•	•		•	•				
3	Jan. 1987				•		•	•		•	•				
4,5,6	Jan. 1987														
7	May 1987			•			•				•				
8	Sep. 1987			•	•			•			•				
9	Oct. 1987			•							•				
10	Mar. 1988			•	•	•	•	•	•		•	•	•	•	
11	Mar. 1988			•	•			•	•	•	•		•		
12	Mar. 1988			•		•	•		•		•		•	•	
13	Mar. 1989								•		•				•
14	Mar. 1989	•		•					•		•	•	•	•	
15	Apr. 1989	•		•					•		•	•	•		
16	Apr. 1989	•									•	•	•	•	
VF1	Feb 1990	•							•		•				
17	Mar. 1990								•	•	•				
18[a]	Mar. 1990	•		•	•			•	•	•	•	•		•	•
VB1	Jun. 1990	•		•					•		•	•		•	•
VF2	Sep. 1990								•		•				
20	Feb. 1991	•							•		•				
SB1[b]	Jun. 1991	•	•						•		•	•			•
VB2	May 1992	•	•	•					•	•	•			•	

Station	Location	Description
KOKE	Kokee Park, Hawaii	NGS tracker Apr 88–Jul 90 (TI, FRPA); 3028-S Jan 91– (Rogue)
PENT	Penticton, British Columbia	887006 Mar 91– (Rogue)
YKNF	Yellowknife, NW Terr.	869211 Jan 87–Jul 89 (TI) ; 889201 Jul 89–Dec 90 (TI), Jan 91– (Rogue)
PLAT	Platteville, Colorado	NCMN 1981 (7258) (TI)
FTDV	Ft Davis, Texas	Harvard RM4 (TI)
AUST	Austin, Texas	Computer (TI)
CHUR	Churchill, Manitoba	774030 (TI)
RICH	Richmond, Florida	Timer 1962 Jun 86 (TI), Feb 88–Feb 89 (TI, FRPA); NGS tracker (MiniMac) Feb 89–May 92
ALGO	Algonquin Rad. Obs. Ont.	ALGO RMA Dec 86–Mar 88 (TI) ; North Pier Nov 88–Dec 90 (TI), Jan 91– (Rogue)
WSFD	Westford, Mass.	Haystack OCP3 Jun 86 (TI) ; WVR tower Oct 86–Aug 88 (TI), Aug 88–Jan 89 (TI, FRPA), Feb 89– (MiniMac)
WETT	Wettzell, Germany	1000 GPS Nov 87–Jul 89 (TI); 7595 Jul 89–Jul 91 (MiniMac); 7598 Jul 91– (Rogue)
TROM	Tromso, Norway	TSS GPSM Dec 87–Jul 90 (TI) ; TSS II May 90– (Rogue)
ONSA	Onsala, Sweden	3-1 Dec 87–Jan 91 (TI), May 91– (Rogue)
TSUK	Tsukuba, Japan	CIGNET '88-'91 Jul 88–Dec 91 (MiniMac); CIGNET '91 Dec 91– (MiniMac)

[a] Experiment 18 included data also from a TI receiver on monument 867001 at the Pacific Geosciences Centre, Pat Bay, British Columbia.

[b] The SB1 analysis used global orbits estimated with data from three southern hemisphere sites as well as those shown.

The velocities estimated from the joint VLBI and GPS solution are given in Table 4 and are discussed in the appendix. Because most of our sites are west of the SAF, we transfer the North American frame in which velocities are estimated to the Pacific frame using the revised NUVEL-1 model. These velocities are shown in Figure 2 with respect to the Pacific plate. In Table 4 and the following discussions, we quote the uncertainty as one standard deviation. As discussed in the appendix, these uncertainties are obtained by scaling the formal values by a factor of 2 to reflect the scatter in the position estimates and the presence of systematic errors. For one-dimensional quantities quoted in the text and Table 4, these scaled standard deviations should be multiplied by an additional factor of 1.96 for testing hypotheses at the 95% confidence level. In the maps of the velocity fields, the ellipses denote the area of 95% confidence in two dimensions, after scaling.

The precision and accuracy of the relative horizontal velocities estimated for the core stations are adequately described by a 95% confidence ellipse with a semiminor axis of approximately 2 mm/yr oriented roughly north-south, and a semimajor axis of 3 mm/yr oriented east-west. As discussed in the Appendix, this level of uncertainty is supported by short- and long-term scatter and good agreement in velocity with independent VLBI and GPS solutions. Further calibration is provided by the rates of shortening estimated by comparing our estimated line lengths with those estimated from trilateration. The velocity estimates are not sensitive to errors in ties between GPS and VLBI monuments, because these ties were not used. On the other hand, they may be sensitive to the orbital reference frame established by the available tracking stations. This sensitivity is most pronounced in the east velocity component for stations observed only two or three times. For these stations, noted in Table 4, the actual uncertainties in eastward velocity may be as large as 5 mm/yr.

TABLE 4. Velocities with Respect to the Pacific Plate

	East			North			
Station	Obs.	Res.	Unc.	Obs.	Res.	Unc.	Cor.
BLAN[a]	4.0	1.4	1.2	−2.0	−3.4	0.9	0.091
BLHL[a]	2.6	−0.0	0.9	−1.8	−2.5	0.6	0.064
BLKB7269	24.3	2.6	1.5	−32.4	−12.7	2.2	−0.092
BLUF[a]	0.4	0.7	1.3	0.4	2.9	0.9	−0.066
BRSH	−0.4	−0.2	1.3	−2.2	0.8	0.9	0.079
CATO	0.3	−0.6	0.9	−6.4	−2.3	0.8	−0.091
CENT[a]	1.9	2.5	0.8	−2.4	−0.2	0.6	−0.014
COTR[b]	0.5	0.2	1.4	−2.0	1.8	1.1	0.153
DEAD7267	25.1	1.8	3.5	−33.8	−13.7	5.1	0.166
DEVL	−0.2	0.3	1.2	−0.7	1.4	0.9	0.198
FIBR[a]	19.6	1.0	1.0	−23.6	−6.5	0.7	0.120
FTOR	−1.4	−3.3	1.4	−0.1	0.0	1.6	−0.047
GAVI	−1.0	−1.4	1.3	−3.4	−2.6	0.9	0.114
GRAS	−1.7	−2.9	1.4	−0.8	−0.5	1.1	−0.072
HAPY	4.3	2.2	1.3	−6.0	−1.0	1.0	−0.087
HOPP	6.4	3.1	0.9	−12.0	−6.4	0.7	−0.149
JPL1	2.7	−0.7	1.1	−11.5	−6.3	0.9	−0.047
LACU[a]	−0.6	−0.8	0.7	−6.3	−3.7	0.6	0.000
LOSP[a]	1.4	−0.1	0.8	−3.1	−3.2	0.6	0.095
LOVE	4.1	−0.6	1.1	−13.7	−7.6	1.0	−0.064
MADC[a]	4.0	0.3	1.1	−6.5	−4.0	0.8	0.035
MOJA[a]	23.9	−2.0	0.3	−26.6	−7.8	0.3	−0.067
MONP7274	−0.8	−2.6	0.7	−8.6	−6.8	0.9	0.019
MUNS	1.1	−1.1	0.9	−11.1	−5.1	0.8	−0.130
NIGU	−1.3	−1.6	1.2	−4.3	−0.8	0.8	0.029
OVRO[a]	20.1	−3.0	0.5	−28.0	−7.1	0.5	0.029
PEAR7254	14.4	−0.9	1.6	−14.6	−2.6	2.4	0.036
PIN1	13.3	2.5	1.0	−13.2	−3.0	0.9	−0.063
POZO[b]	4.5	−0.1	1.2	−5.5	−2.9	0.7	0.083
PRES7252	8.7	−9.0	0.8	−15.9	1.2	1.1	−0.008
PVER[a]	0.7	0.4	0.6	−5.2	−1.7	0.5	−0.033
SAFE	3.0	0.1	0.8	−9.9	−4.8	0.7	−0.107
SCLA[b]	2.9	1.6	2.8	−7.1	−2.4	2.0	−0.242
SNP2	4.9	2.7	1.3	−12.7	−7.4	1.0	−0.180
SNPA	1.9	0.1	0.8	−8.7	−3.7	0.6	0.024
SNRI	−0.3	0.2	1.4	−1.8	−0.5	1.0	0.276
SOLI	0.0	−0.2	0.9	−8.0	−4.1	0.7	0.086
SOLJ	−2.0	−2.5	2.4	−5.9	−4.1	1.7	−0.127
TWIN	−1.2	−0.6	1.2	−0.8	1.3	0.8	−0.065
VNDN[a]	0.3	−0.4	0.4	−1.0	−1.0	0.4	−0.044

Velocities are in millimeters per year.

Obs., observed; Res., residual; Unc., uncertainty after scaling by 2.

Cor., correlation coefficient between east and north components.

[a] core site observed at least 5 times.

[b] site observed only 2 times, or 3 times with $\sqrt{\chi^2/f} > 2$.

REMOVAL OF A MODEL OF THE EFFECTS OF THE SAN ANDREAS FAULT

In Figure 2, the dominant feature in the velocity field is the simple shear associated with the San Andreas fault system. Indeed, at this scale it is difficult to discern any other features. Since the SAF motion is not the primary object of our study, we choose to remove a reference model for velocities associated with the fault and to examine the residual velocities.

A simple (and conventional) model attributes this shear to slip at depth on the SAF and associated faults below an upper locked portion of the fault. Our GPS network is too sparse, with too little coverage near the faults, to reliably estimate parameters in such a model. The best constraints on the rates of slip and locking depths come from the more densely spaced trilateration surveys of the U.S. Geological Survey (USGS). For the SAF northwest of its intersection with the San Jacinto fault, the rate of slip estimated from inversion of the geodetic data (32–36 mm/yr [*Eberhart-Phillips et al.*, 1990; *Lisowski et al.*, 1991]) is consistent with the value of 34 mm/yr inferred from geology [*Sieh and Jahns*, 1984], which we adopt here. The locking depth in the model is 25 km between Parkfield and San Gorgonio Pass but shallower elsewhere (Table 5 and Figure 3). For an infinitely long fault slipping at velocity v_S beneath a locking depth d, the predicted velocity v is parallel to the fault and increases with distance x from the fault in an arctangent sigmoid curve: $v = (v_S/\pi)\tan^{-1}(x/d)$ [e.g., *Savage and Burford*, 1973]. Owens Valley Radio Observatory (OVRO) is our farthest regional site (~ 250 km) to the northeast of the SAF; TWIN on San Nicholas Island is our farthest site (~200 km) to the southwest. For a locking depth of 25 km, almost 32 of the total 34 mm/yr velocity due to deep slip on the SAF is expected to accumulate between OVRO and TWIN.

While this simple model is useful for a rough estimate of the amount of deformation associated with the SAF, the actual fault geometry is more complicated. For example, the locking depth probably varies along strike [*Lisowski et al.*, 1991]. In addition, the SAF takes a left step near its intersection with the Garlock fault in the region of the Big Bend and forms three splays in southern California. To include the effects of this relatively well-mapped complexity, we use a model that includes slip on the San Andreas, San Jacinto, Elsinore, and Garlock faults (Table 5). We choose not to include the Eastern California Shear Zone [*Dokka and Travis*, 1990a,b; *Savage et al.*, 1990] in our model because the locus of the shear is not well determined.

We calculate the relative site velocities using *Okada's* [1985] expressions for velocities due to slip on a buried planar disloca-

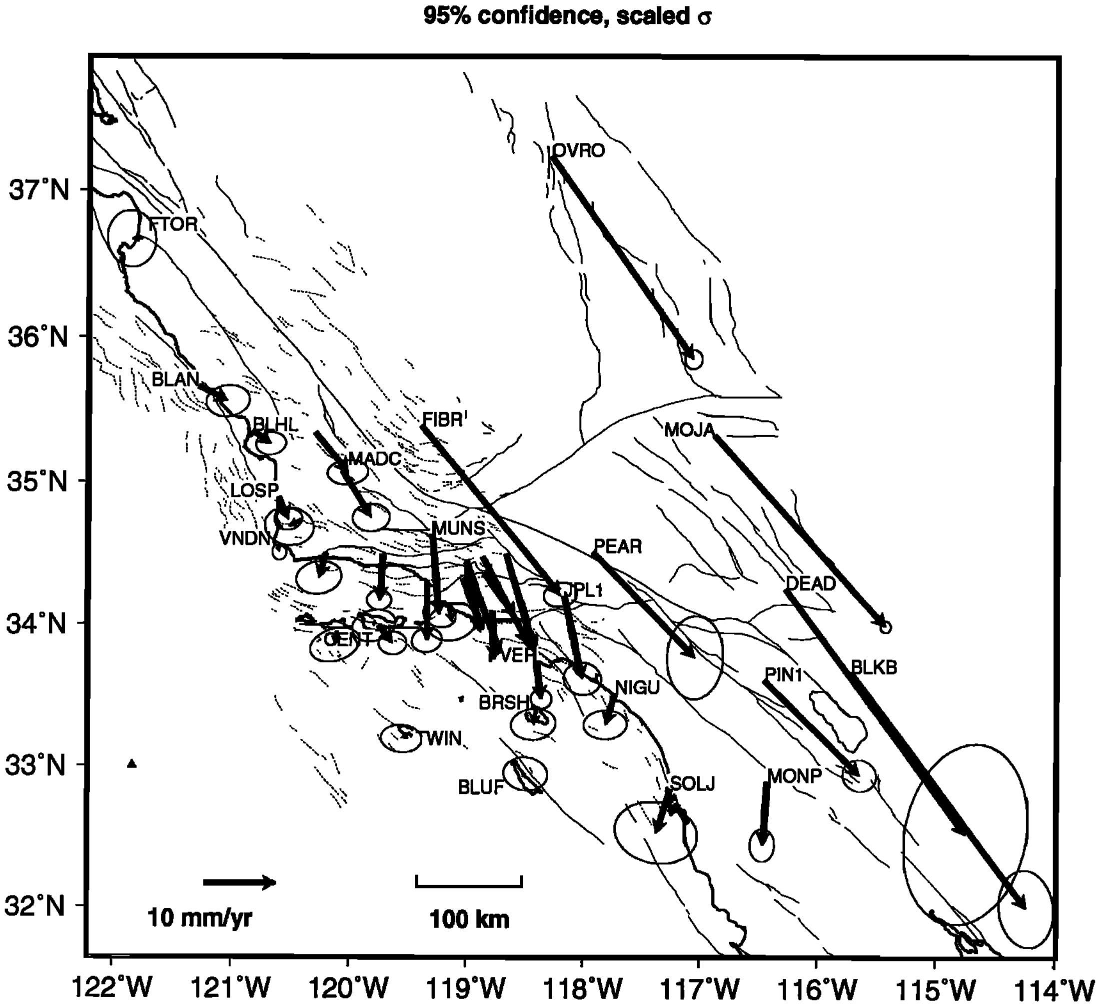

Fig. 2. Observed velocity of stations relative to the Pacific plate estimated from the combined GPS and VLBI data set. The velocities are estimated in the reference frame fixed on North America as described in the appendix and then transferred to the Pacific plate using the rescaled NUVEL-1 prediction for the relative motion of the two plates. The ellipses denote the region of 95% confidence, after scaling the formal uncertainties by a factor of 2, as described in the text. For clarity, the ellipses are not shown for the sites in the Ventura Basin. As listed in Table 4, they are similar in size to the ellipse at MUNS.

TABLE 5. Fault Segments for Dislocation Model

Fault Segment	Origin Longitude W	Origin Latitude N	Length km	Azimuth	Slip Rate mm/yr	Locking Depth km	Remarks
SA 1	121°13'	36°36'	∞	318°	34	10	
SA 2	120°35'	35°58'	111	321°	34	1	*Burford and Harsh* [1980]
SA 3	119°23'	34°55'	197	318°	34	25	*Harris and Segall* [1987]
SA 4	119°23'	34°55'	118	106°	34	25	*Eberhart-Phillips et al.* [1990]
SA 5	118°22'	34°40'	141	118°	34	25	*Eberhart-Phillips et al.* [1990]
SA 6	117°15'	34°10'	77	107°	19	25	H. Johnson personal communication, 1992
SA 7	114°08'	34°00'	∞	133°	19	15	H. Johnson personal communication, 1992
GAR	118°56'	34°49'	160	57°	10	10	*Eberhart-Phillips et al.* [1990]
ELS	117°40'	33°54'	2000	125°	5	15	H. Johnson personal communication, 1992
SJC	117°32'	34°18'	2000	132°	10	10	H. Johnson personal communication, 1992

tion in an elastic half-space with uniform elastic moduli. For simplicity, we assume a Poisson material and ignore the effects of sphericity and variation of moduli with depth. Figure 3 shows the velocities predicted by the dislocation model plotted by assigning zero velocity to the point shown near the SW corner of the map, approximately 250 km offshore and 375 km from the SAF. For a point this far from the SAF, the velocity predicted by the arc tangent function, relative to points much farther outboard on the Pacific plate, is still almost 1 mm/yr.

In addition, there are spatial variations in the model velocity field induced by the Big Bend and Garlock faults. The left step of the SAF in the region of the Big Bend results in compression along the direction of plate motion, with extension perpendicular to this direction. The net effect, in the reference frame of the

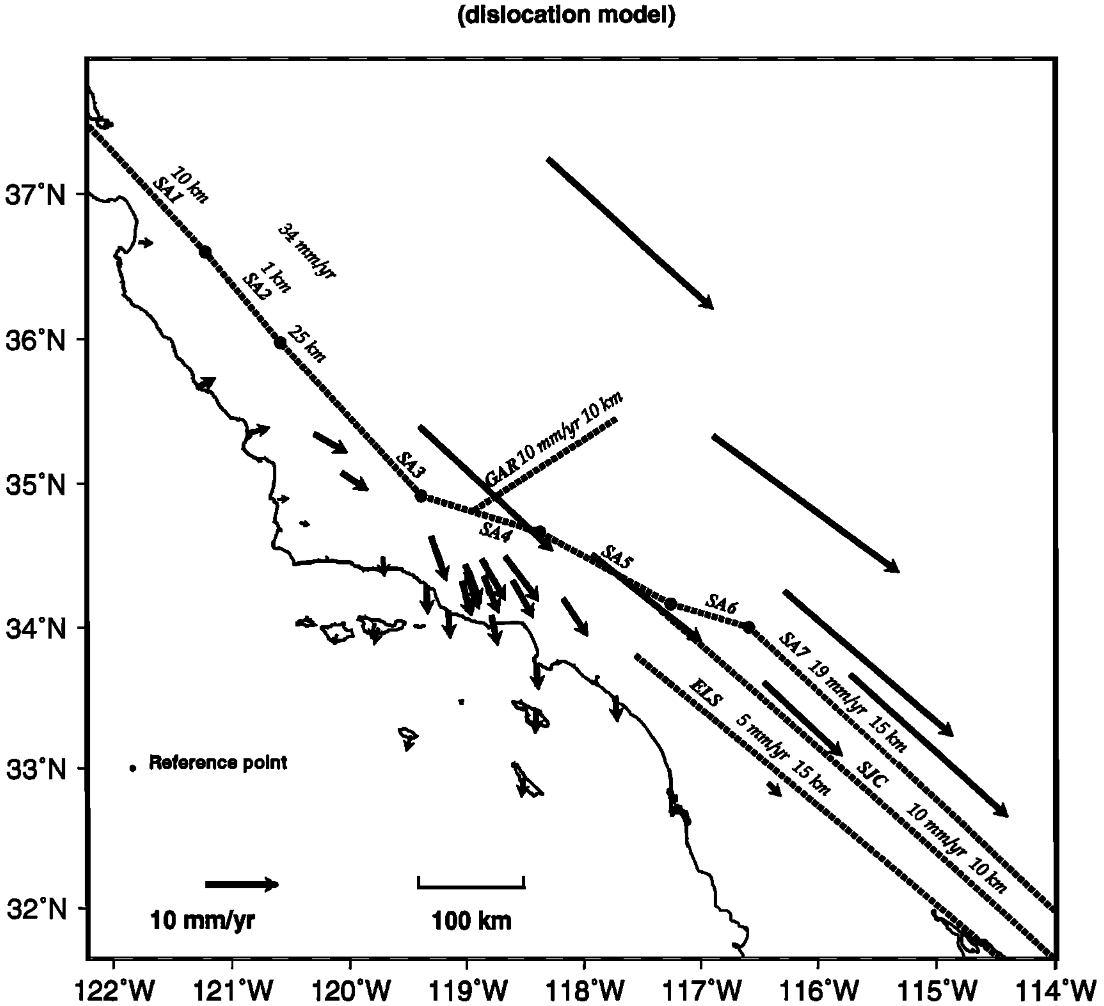

Fig. 3. Velocities predicted by our a priori model, which includes the relative motion of the Pacific and North America plates as well as deep slip on the fault segments listed in Table 5. The faults are modeled as slipping at the indicated rate below the indicated depth. The reference frame is the same as in the previous figure, with the offshore point at (33°N, 121°50'W) assigned zero velocity. The modeled faults include the San Andreas (SA1–SA7), the Garlock (GAR), the San Jacinto (SJC), and the Elsinore (ELS).

Pacific plate, is clockwise rotation and fault-normal velocity in the region south of the Big Bend. The fault-normal velocities of the three most northerly sites on the west side of the SAF are the result of the combined effect of the Big Bend and of the shallow locking depth used in their vicinity.

In the following discussion, we consider the residual velocity field: the difference between the observed field (Figure 2) and that predicted by the dislocation model (Figure 3). Figure 4 shows the residual field, relative to the offshore point. These residual velocities are thus referred to a frame essentially fixed on the Pacific plate. The magnitude of the overall shearing and rotation is now substantially diminished, revealing a number of interesting features.

The only group of sites with residual velocity not resolvably different from zero is in the region of the southern Channel Islands, where San Nicolas (TWIN), San Clemente (BLUF), and Santa Catalina (BRSH) islands all have residual velocities less than 2 ± 2 mm/yr, consistent with their being on the Pacific plate. Their observed velocities to the south or SW with respect to the Pacific plate (Figure 2) can be explained almost entirely by our model for the effects of deep slip on the SAF and associated faults (Figure 4).

There is substantial convergence normal to the SAF in the region spanning the southern Channel Islands, the Los Angeles basin, and the Mojave desert. For example, the residual shortening of a line oriented S35°W between MOJA and BLUF (on San Clemente Island) is 10.3 ± 1.0 mm/yr, with about half of this occurring across the Los Angeles basin between Pasadena (JPL1) and Palos Verdes (PVER), as discussed below. The residual velocities of stations MUNS, PEAR, and their neighbors point toward the SSW (relative to the Pacific plate), nearly perpendicular to the trace of the SAF.

Similar fault-normal velocities are evident in the residual velocity field northeast of the Big Bend, where the fault-normal (S49°W) component of the residual velocity is 8.2 ± 0.6 mm/yr at OVRO and 4.9 ± 0.8 mm/yr at FIBR. Because of the lack of stations in this area, the best measure of the rate of compression is 3.3 ± 1.0 mm/yr for the fault-normal component of the residual velocity between OVRO and FIBR.

Figure 5 shows the details of the residual velocity field plotted relative to Vandenberg (VNDN). To the north of VNDN, the velocities are dominated by shear parallel to the trace of the SAF (S41°E). The residual fault-parallel motion of LOSP, MADC, and FIBR increases systematically to the NE, with rates of 2.2 ± 0.4,

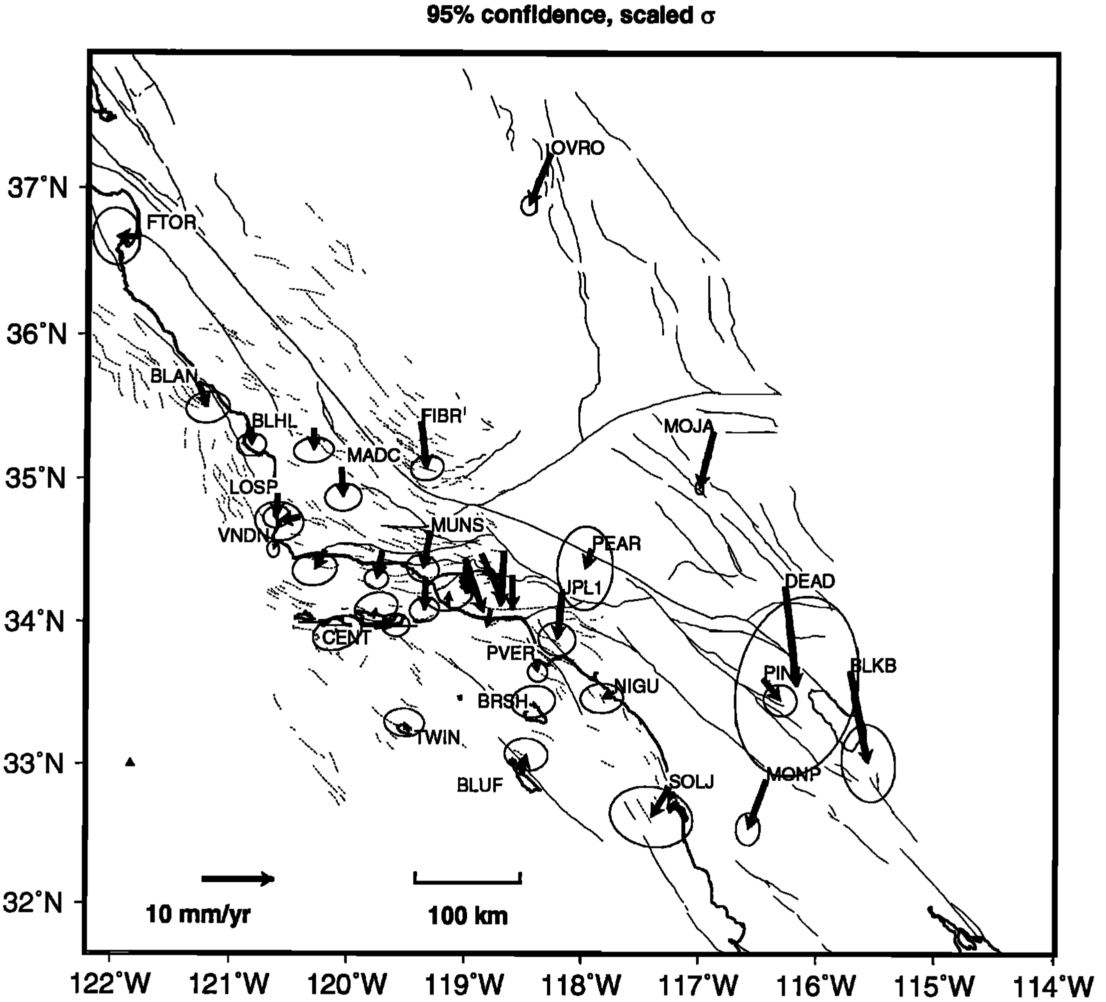

Fig. 4. Residual velocities, showing the observed velocity field (Figure 2) minus our model (Figure 3). Residual velocities are plotted relative to the offshore point (dot at 33°N, 121°50'W) on the Pacific plate. Confidence ellipses are 95%, as in Figure 2.

3.7 ± 0.8, and 6.7 ± 0.6 mm/yr, respectively, relative to VNDN. To the northwest, sites BLAN, BLHL, and POZO have fault-parallel residual velocities of 3.4 ± 1.0, 2.0 ± 0.6, and 2.6 ± 0.8 mm/yr with respect to VNDN. These are the residual values after removal of the SAF shear, which is less than 1 mm/yr on the coast and 4 to 5 mm/yr for POZO and MADC, respectively, according to the reference fault model. The fault-normal component of the residual velocity in this area of the Southern Coast Ranges is small for all sites, with the largest value occurring at FIBR, which shows 2.2 ± 0.8 mm/yr of residual fault-normal compression with respect to VNDN. There is a change in the deformation pattern near the Santa Maria Fold and Thrust Belt. Convergence across the Santa Barbara Channel and the western Transverse Ranges is clearly evident in the LACU–CENT and MUNS–COTR vectors, respectively. The motions of LACU, MUNS, and SOLI with respect to VNDN suggest clockwise rotation in the western Transverse Ranges. These motions will be discussed in their regional contexts below.

Figure 6 shows the residual velocity field plotted with respect to Palos Verdes, including interesting residual velocities of sites near the Ventura and Los Angeles basins. The residual convergence rate across the Ventura basin reaches 5.1 ± 1.2 mm/yr for SCLA-SNP2, with rapid clockwise rotation apparent. In the Los Angeles basin, the residual convergence of site JPL1 toward PVER is 5.0 ± 1.0 mm/yr at S12°W ± 14°. This compressive regime seems to extend to Catalina Island, where BRSH has a northward (N13°W ± 30°) residual velocity of 2.6 ± 1.0 mm/yr relative to PVER. A large group of sites (BLUF, BRSH, TWIN, CENT, and COTR) have northerly velocities of 3–5 mm/yr relative to PVER. This motion produces large velocity gradients in the neighboring regions. The velocity of this group of stations with respect to the mainland (PVER, NIGU, and SOLJ) indicates shear in the Gulf of Santa Catalina. Similarly, rotation of the blocks to the south of the Ventura basin results in left-lateral strike slip on the Santa Monica lineament between COTR and PVER, while the Santa Barbara Channel absorbs compression between SOLI and CENT.

Velocity Gradient Tensor

We have calculated the velocity gradient tensor **L** [*Malvern*, 1969] in each of the triangular subnetworks spanning the California network. The triangles are optimally close to equilateral and thus constitute a "Delaunay triangulation" [*Davis*, 1986; *Gold*, 1975; *Watson*, 1982]. The symmetric part of **L** is the strain rate tensor, whose eigenvalues and eigenvectors are written according to the convention of *Prescott et al.* [1979] and *Feigl et al.* [1990]. The antisymmetric part of **L** gives a local measure of the average vorticity, or rate of rotation. The observed values of

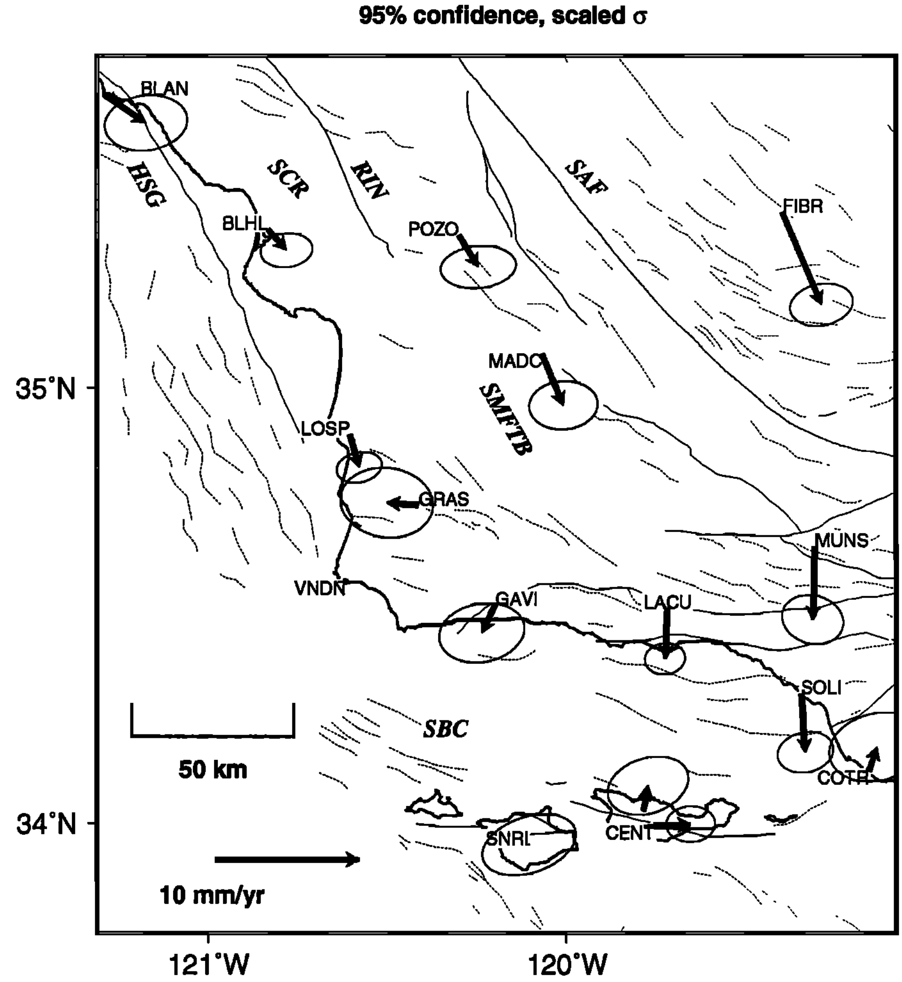

Fig. 5. Residual velocities plotted relative to Vandenberg (VNDN). Note that the velocity scale is double that of Figure 4. Confidence ellipses are 95%, as in Figure 2. The tectonic features include the San Andreas fault (SAF), the Santa Barbara Channel (SBC), the Hosgri fault (HSG), the Rinconada fault (RIN), the Santa Maria Fold and Thrust Belt (SMFTB), and the southern Coast Ranges (SCR).

the velocity gradient tensor are given in Table 6. These are dominated, in general, by the shearing and rotation associated with the simple shear regime of the SAF.

The strain rates calculated from the residual horizontal velocity field are shown in terms of their principal axes in Figures 7 and 8 and listed with their uncertainties in Table 6. Very high rates of residual strain are apparent in the Ventura basin, while lower, but nonetheless interesting, rates remain in the southern Coast Ranges and the Santa Barbara Channel.

Figures 9 and 10 show the antisymmetric part of the velocity gradient tensor, the average rate of rotation about a vertical axis, calculated for the residual horizontal velocity field. Before comparing these rotation rates to those inferred from paleomagnetic declinations [e.g., *Luyendyk*, 1991], we mention several details. First, the rotation rates estimated from the geodetic data are referenced to the Pacific plate. Although such a frame is not identical to the paleomagnetic frame defined by the apparent magnetic North pole, the difference between them in this case is small enough to neglect. Second, we emphasize that Figures 9 and 10 show residual rotation rates, after removing transient shear in our simple dislocation fault model. Such a model is necessary if we are to compare rates over two different sampling times. The geodetic measurements span a period of 5 years, considerably shorter than a seismic cycle. In contrast, the paleomagnetic declinations measure finite rotation accumulated during the last 6–16 m.y., and thus represent the average over many seismic cycles.

With these caveats in mind, we note that the geodetic residual rotation rates do not agree everywhere with the paleomagnetic values summarized by *Jackson and Molnar* [1990]. In much of the Transverse Ranges, the average rate of clockwise rotation since the Miocene is 5–6 °/m.y. [*Luyendyk*, 1991]. In contrast, the geodetic residual rotation rate varies from 3 ± 2°/m.y. counterclockwise in the eastern end of the Santa Barbara Channel (triangle CENT-COTR-SOLI in Figure 9) to 7 ± 2°/m.y. clockwise in the Ventura basin (CATO-HAPY-SAFE in Figure 10). Around Santa Cruz Island (CENT), the paleomagnetic declinations are larger than elsewhere in the Transverse Ranges, indicative of rapid clockwise rotation. Yet the geodetic residual rates are less than 0.5 ± 1°/m.y. for the five triangles around CENT (Figures 9 and 10). In the coastal part of the Santa Maria Basin, neither the paleomagnetic declination nor the geodetic residual field yields a rotation rate resolvably different from zero (Figure 9) [*Hornafius et al.*, 1986]. Thus the residual geodetic and paleomagnetic observations of rotation rate differ by an amount which varies with location.

Why do the two types of observations disagree? The most likely possibility is that rotation rates are not constant in

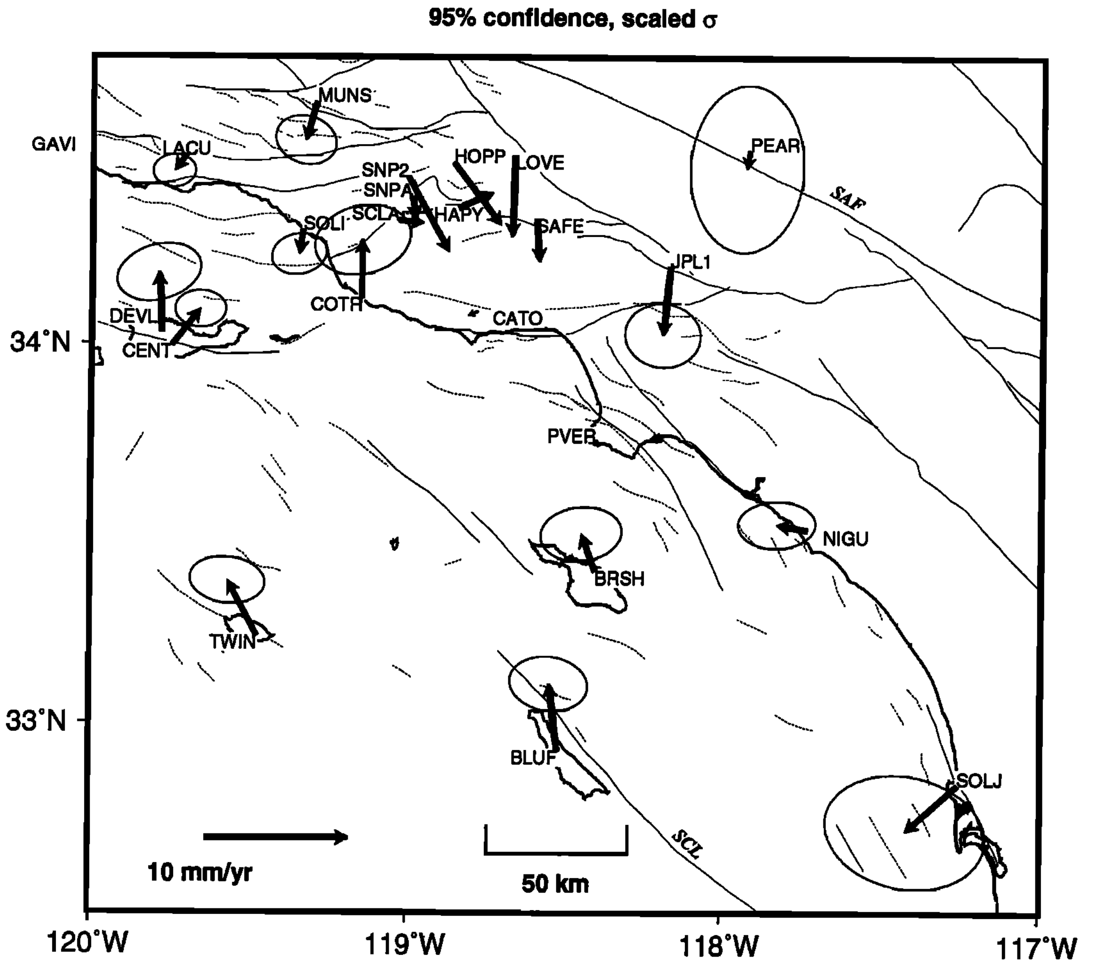

Fig. 6. Residual velocities plotted relative to Palos Verdes (PVER). Confidence ellipses are 95%, as in Figure 2. For clarity, ellipses are not shown for the stations in the Ventura Basin. The size of these ellipses are comparable to that of MUNS. The tectonic features include the San Andreas fault (SAF) and the San Clemente fault (SCL).

geological time. This might occur as faults rotate out of the position in which their slip is favored [*Scotti et al.*, 1991]. In this case, the area south of the Ventura basin appears to be the currently rotating element [*Yeats*, 1983]. It may also be that our elastic dislocation fault model overpredicts the amount of rotation due to elastic strain and leaves too little to inelastic strain. Yet another possibility is that our geodetic stations provide a sample of the velocity field which is too coarse in space. Rather than speculate on these possibilities, we prefer at this point simply to present our geodetic estimates, saving detailed modeling for a future study.

TECTONIC INTERPRETATION

Northeast of the San Andreas Fault

There is substantial residual velocity parallel to the SAF for sites to the northeast of this structure (Figure 4). The sites farthest to the northeast, OVRO and MOJA, have residual velocities with fault-parallel components of 3.2 ± 0.4 mm/yr (at S41°E) and 4.5 ± 0.4 mm/yr (at S68°E), respectively, relative to the Pacific plate. Near the fault, site FIBR has 5.4 ± 0.8 mm/yr of residual velocity parallel to the SAF (at S41°E). These rather large residuals could be reduced by modifying the simple dislocation model we have used to describe the effects of the major faults in the region. The possible changes include (1) decreasing the relative velocity of the Pacific plate relative to the North American plate, which provided the reference frame in which the velocities were determined; (2) increasing the rate of slip v; (3) reducing the locking depth d; or (4) including deep slip on other faults. An additional possibility, discussed in a later section, is that the simple model of uniform slip at the geological rates on these faults is inadequate. In this case, time-dependent effects of strain accumulation during the seismic cycle must be considered.

The first two factors are unlikely to be the most important ones. The plate rate has already been reduced by 2 mm/yr by the rescaling of the NUVEL-1 motion model. Using the highest proposed rates of slip for the SAF, 36 mm/yr [e.g., *Lisowski et al.*, 1991], would account for only a quarter of the residual fault-parallel velocities. In addition, it seems logically inconsistent to use a slip rate other than the geological average in this simple model.

There is some evidence from our measurements that the locking depth on the SAF should be shallower. Station MADC, the site on the southwest side of the SAF nearest to FIBR, has a fault-parallel residual velocity of 3.2 ± 0.8 mm/yr, indicative of some 2 mm/yr of unmodeled shear between these two sites straddling the SAF. Near the fault, the residual shear could be reduced by modeling the fault with a shallower locking depth, but this would enlarge the residuals of the other stations southwest of the fault.

TABLE 6. Velocity Gradient Tensor

Delaunay Triangle	Extensive Eigenvalue (0.1 ppm/yr)			Compressive Eigenvalue (0.1 ppm/yr)			Rotation Rate (deg/m.y.)			Compressive Azimuth (deg)		
	Obs.	Res.	Unc.	Obs.	Res.	Unc.	Obs.	Res.	Unc.	Obs.	Res.	Unc.
BLAN-BLHL-LOSP	0.5	0.3	0.5	-0.3	-0.5	0.4	-0.0	-1.3	1.6	112	102	29
BLAN-BLHL-POZO	0.5	0.1	0.3	-1.0	-0.4	0.4	5.4	1.9	1.8	-3	-21	13
BLAN-FTOR-POZO	0.4	0.4	0.1	-0.5	-0.4	0.3	0.1	-1.7	0.8	49	77	10
BLAN-LOSP-VNDN	0.2	0.1	0.3	-0.7	-0.8	0.2	4.1	3.0	0.8	24	27	15
BLHL-LOSP-POZO	0.5	0.1	0.2	-0.1	0.0	0.1	3.8	0.8	0.7	17	80	13
BLKB-DEAD-MOJA	2.2	1.7	3.4	-1.0	-0.7	1.9	-7.8	-6.8	11.0	111	109	30
BLKB-DEAD-PIN1	1.6	0.4	0.3	-2.4	-1.5	0.7	11.7	4.0	1.8	9	24	4
BLKB-MONP-PIN1	1.6	0.7	0.3	-0.8	-0.2	0.1	13.6	6.5	1.1	11	59	4
BLUF-BRSH-NIGU	-0.0	-0.1	0.4	-0.5	-0.4	0.2	0.9	0.7	1.3	24	31	21
BLUF-BRSH-TWIN	0.2	0.1	0.1	-0.5	-0.4	0.2	0.2	-0.1	0.9	9	8	15
BLUF-NIGU-SOLJ	0.1	0.3	0.3	-0.4	-0.4	0.2	2.0	2.0	0.9	48	59	14
BRSH-NIGU-PVER	-0.2	-0.2	0.3	-0.8	-0.7	0.2	1.9	1.4	1.1	-6	-3	17
BRSH-PVER-TWIN	0.1	0.1	0.2	-0.8	-0.7	0.3	1.3	0.7	1.1	-10	-10	12
CATO-COTR-SCLA	0.1	-0.0	0.5	-1.6	-1.3	0.9	7.7	6.4	3.7	7	14	22
CATO-COTR-TWIN	0.7	0.7	0.4	-0.4	-0.5	0.2	4.7	4.3	1.3	52	60	14
CATO-HAPY-SAFE	-0.0	0.3	0.5	-0.6	-1.0	0.4	9.1	7.4	1.9	56	68	41
CATO-HAPY-SCLA	1.4	1.2	1.3	-0.6	-0.5	0.8	3.0	1.3	4.1	-41	128	25
CATO-JPL1-PVER	0.4	0.2	0.2	-1.0	-0.8	0.2	3.2	1.5	0.8	9	23	5
CATO-JPL1-SAFE	0.3	-0.0	0.2	-0.9	-0.6	0.4	4.9	3.0	1.4	-4	14	13
CATO-PVER-TWIN	0.2	0.2	0.1	-0.5	-0.3	0.1	1.2	0.7	0.6	4	12	8
CENT-COTR-SOLI	-0.1	-0.2	0.3	-2.4	-2.2	0.4	-2.6	-3.4	1.8	-4	-7	7
CENT-COTR-TWIN	-0.0	0.1	0.2	-0.4	-0.6	0.2	1.0	0.1	0.7	127	120	19
CENT-GAVI-LACU	0.4	0.3	0.2	-1.0	-0.8	0.2	1.2	-0.4	0.8	28	24	7
CENT-GAVI-SNRI	0.7	0.8	0.4	-0.3	-0.3	0.2	0.9	-0.4	1.1	3	-1	14
CENT-LACU-SOLI	0.4	0.2	0.2	-1.1	-1.0	0.2	1.8	0.2	0.7	33	33	6
CENT-SNRI-TWIN	0.7	0.8	0.5	-0.3	-0.3	0.1	2.5	1.8	1.0	-14	-21	9
COTR-SCLA-SOLI	1.1	0.8	1.0	-2.6	-2.3	0.7	0.6	-0.9	3.8	-10	-11	8
DEAD-MOJA-PEAR	1.0	0.6	0.3	-0.2	-0.3	0.2	4.9	1.9	1.2	25	45	10
DEAD-NIGU-PEAR	1.0	0.4	0.3	-1.2	-0.4	0.2	9.3	3.1	1.1	-2	26	5
DEAD-NIGU-PIN1	1.2	0.4	0.1	-2.8	-1.5	0.7	6.0	0.2	1.6	-7	3	4
FIBR-LOVE-MUNS	1.4	0.2	0.3	-1.8	-0.2	0.1	9.6	2.7	0.8	-14	13	2
FIBR-LOVE-PEAR	2.0	0.8	0.4	-1.5	-0.2	0.2	8.0	-1.1	1.3	-22	118	4
FIBR-MADC-MUNS	1.2	-0.0	0.2	-1.7	-0.2	0.1	12.4	2.0	0.5	-5	2	2
FIBR-MADC-POZO	1.8	0.4	0.2	-1.2	-0.1	0.3	10.5	1.7	1.2	7	39	4
FIBR-MOJA-OVRO	0.3	0.0	0.0	-0.2	-0.1	0.0	0.8	0.3	0.1	12	60	4
FIBR-MOJA-PEAR	0.3	-0.1	0.1	-1.2	-0.5	0.2	3.4	0.8	0.5	-13	2	4
FIBR-OVRO-POZO	3.0	0.5	0.2	-0.2	-0.2	0.0	4.5	1.1	0.5	36	45	2
FTOR-OVRO-POZO	0.8	0.2	0.1	-0.5	-0.2	0.1	3.4	0.7	0.3	15	38	2
FTOR-OVRO-PRES	0.5	0.4	0.0	-1.5	-0.2	0.2	5.1	0.0	0.4	-6	38	2
GAVI-GRAS-MADC	1.3	1.1	0.7	-0.3	-0.2	0.2	6.5	3.8	1.6	17	22	10
GAVI-GRAS-VNDN	0.8	0.8	0.5	-0.7	-0.7	0.3	0.4	-1.0	2.0	65	63	12
GAVI-LACU-MADC	0.1	0.2	0.3	-0.4	-0.2	0.1	4.7	2.0	0.8	-7	-0	17
GAVI-SNRI-VNDN	0.1	0.0	0.1	-0.7	-0.7	0.4	2.0	1.1	1.1	45	40	14
GRAS-LOSP-MADC	0.3	0.1	0.2	-1.7	-1.6	0.5	5.4	3.0	1.8	-25	-31	9
GRAS-LOSP-VNDN	-0.3	-0.4	0.2	-1.6	-1.7	0.7	-0.4	-1.6	1.7	116	116	15
HAPY-HOPP-LOVE	-1.3	-2.0	0.7	-4.7	-4.1	0.9	5.6	2.2	3.6	-9	-4	11
HAPY-HOPP-SNPA	2.4	1.9	0.8	-4.7	-4.1	0.9	3.0	-0.1	3.6	-11	-9	5
HAPY-LOVE-SAFE	-0.2	-0.1	0.6	-3.0	-3.0	0.6	7.7	4.1	2.6	18	33	9
HAPY-SCLA-SNPA	1.3	1.0	1.1	-3.1	-2.7	2.6	-8.9	-10.7	11.4	5	9	25
HOPP-LOVE-MUNS	1.8	2.1	0.7	-3.7	-4.0	1.4	-10.6	-13.7	5.1	42	49	8
HOPP-MUNS-SNP2	1.3	1.6	0.7	1.0	0.5	1.1	-0.8	-3.1	4.6	3	69	165
HOPP-SNP2-SNPA	1.4	0.7	0.8	-8.2	-7.6	2.3	7.2	4.8	7.0	-25	-27	8
JPL1-NIGU-PEAR	2.7	0.8	0.6	-1.2	-0.8	0.2	5.7	-3.6	2.0	-14	132	5
JPL1-NIGU-PVER	-0.1	-0.3	0.2	-1.1	-0.8	0.2	2.7	0.9	0.7	-5	13	7
JPL1-PEAR-SAFE	1.6	1.1	0.4	-1.1	-0.1	0.5	10.3	0.8	1.7	-28	92	8
LACU-MADC-MUNS	0.2	-0.1	0.2	-0.5	-0.2	0.2	5.7	1.6	0.8	9	28	11
LACU-MUNS-SOLI	0.5	0.2	0.2	-0.8	-0.4	0.2	3.9	0.5	1.1	15	29	8
LOSP-MADC-POZO	0.4	0.3	0.3	-0.1	0.0	0.2	3.5	1.1	1.1	9	50	18
LOVE-PEAR-SAFE	1.6	0.0	0.3	-2.1	-1.3	0.6	4.0	-2.7	2.2	-8	-9	6
MONP-PIN1-SOLJ	0.6	0.5	0.2	-1.1	-0.1	0.2	6.5	3.4	0.8	-33	105	6
MUNS-SNP2-SOLI	1.7	1.4	0.5	-0.8	-0.4	0.2	4.3	2.3	1.4	12	23	6
NIGU-PIN1-SOLJ	1.2	0.4	0.1	-0.2	0.3	0.2	4.9	2.0	0.9	-1	-35	7
SCLA-SNP2-SNPA	-2.2	-2.2	3.1	-12.4	-11.9	5.8	-8.0	-9.6	15.8	126	124	19
SCLA-SNP2-SOLI	1.2	0.8	0.8	-4.8	-4.3	2.2	1.9	-0.6	7.4	-11	-10	14

Obs., observed; Res., residual; Unc., uncertainty after scaling by 2.0.

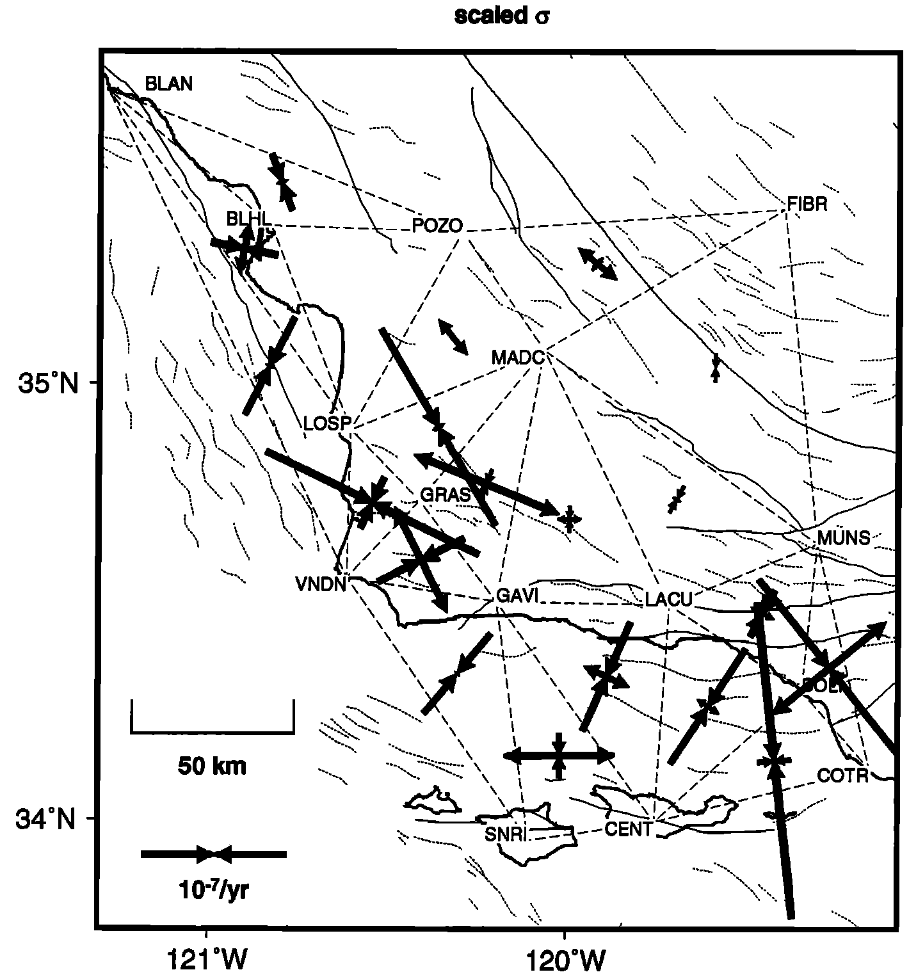

Fig. 7. Principal axes of the horizontal strain rate tensors in the area around Vandenberg, calculated for the residual velocity field shown in Figure 5. In each Delaunay triangle, the inward pointing arrows represent compression; outward pointing arrows represent extension. If neither principal strain rate is larger in magnitude than its uncertainty or if the orientation of the axes has an uncertainty greater than 30°, then the axes are not plotted. Values and uncertainties for all triangles are given in Table 6.

There is independent geodetic evidence that we have neglected important structures near the northeast edge of our network. Sites OVRO and MOJA are near the Eastern California Shear Zone, which from terrestrial geodetic evidence accumulates approximately 8 mm/yr of fault-parallel velocity across it [*Savage et al.*, 1990]. A rate of this magnitude is sufficient to explain the fault-parallel components of the residual velocities we estimate at these two stations.

In addition to the fault-parallel component of residual velocity, the sites northeast of the SAF have a significant component of velocity to the SW, perpendicular to the trace of the SAF. This fault-normal velocity cannot be explained by adjusting the locking depths of our model faults. For example, there is fault-normal compression of 5.7 ± 0.5 mm/yr between OVRO and BLAN. The existence of this compression is consistent with the formation of the anticlinal structures that trap petroleum [*Callaway*, 1971] and the thrust mechanism of the 1983 Coalinga earthquake [*Stein and King*, 1984]. To our knowledge, this is the first determination of the total rate of shortening across these structures.

Southern Coast Ranges

The residual velocities in the southern Coast Ranges (Figure 5) are predominantly parallel to the SAF. One possible explanation for these residuals is that the locking depth for the SAF is too shallow in the simple reference model. As discussed above, it seems more likely that the modeled depth is too deep, in which case the residual fault-parallel velocities are more likely the result of strain accumulation on some other structure. The San Simeon strand of the Hosgri-San Gregorio fault system [*Pacific Gas and Electric*, 1988], a plausible candidate for such strain accumulation, lies between our stations at Point Piedras Blancas (BLAN) and Black Hill (BLHL), near Morro Bay. These two stations exhibit a relative residual velocity of 1.7 ± 0.7 mm/yr, a result only marginally different from no deformation. Despite its unexpected left lateral direction (S57E ± 42°) direction, this vector is not sufficiently precise to exclude activity on the fault. Even if the fault were active, these stations would capture very little motion between them if the fault were locked to great depth, because both stations are quite close to the fault (less than 5 and 15 km for BLAN and BLHL, respectively). For example, if the fault were locked to 25 km depth, and slipping at 2 mm/yr below that depth, the arc tangent dislocation calculation would predict less than 0.5 mm/yr of motion between BLAN and BLHL. Although such strain accumulation would be right-lateral, it would be difficult to detect with our geodetic measurements. Nonetheless, there is a slight difference between our short-term geodetic left-lateral rate and the long-term, right-lateral rates of

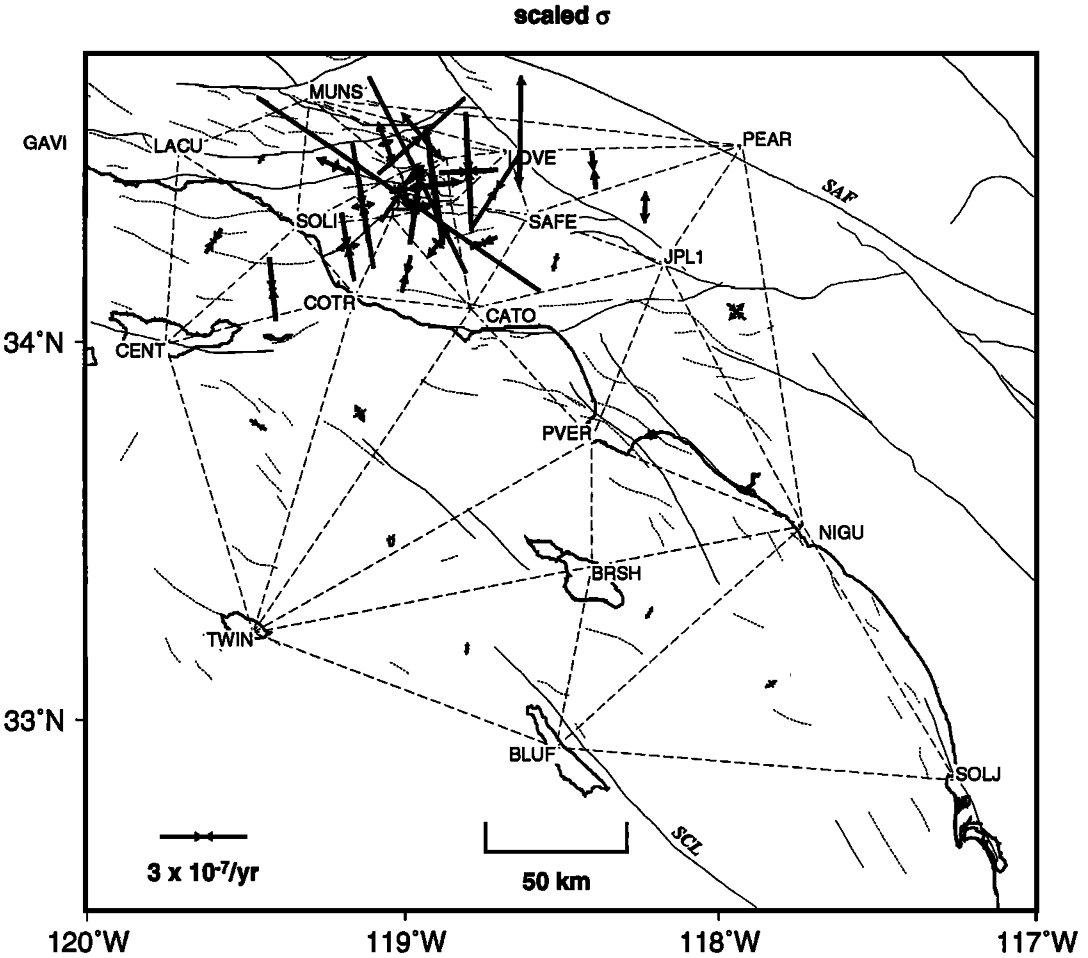

Fig. 8. Principal axes of the horizontal strain rate tensors in the area around Palos Verdes, calculated for the residual velocity field shown in Figure 4. Plotting conventions as in Figure 7. Note that the scale for the strain rate is different from that of the previous figure by a factor of 5.

1.25 ± 0.5 mm/yr inferred from trenching and the 1–3 mm/yr inferred from offset terraces and drainages [*Pacific Gas and Electric*, 1988]. Given such a small ratio of signal to noise, however, the two types of estimates are compatible, unless the fault is slipping near the surface.

The significant fault-parallel residual velocities of sites POZO and MADC indicate a shortcoming in the reference model. As discussed above, these residuals would be increased by a model with a locking depth less than 25 km. To decrease their magnitude would require an implausibly deep locking depth on the SAF. An alternative explanation is strain accumulation on a previously unrecognized onshore structure, or on an offshore structure, such as the Hosgri fault.

In the San Luis trilateration network, fault-normal compression has been inferred by *Harris and Segall* [1987] using data collected between 1959 and 1984. Although such motion is kinematically compatible with the notion that the San Andreas fault is "weak" [*Zoback et al.*, 1987; *Mount and Suppe*, 1987], it has not been observed by *Lisowski et al.* [1991] for other USGS trilateration networks, or by *Shen and Jackson* [1993] from the combination of GPS and early triangulation data. *Dong* [1993] finds fault–normal extension for the same network from a data set that includes USGS trilateration data from 1980 to 1990, but the extension rate is not statistically significant. Our GPS estimates provide independent evidence on this apparent contradiction. Although BLHL is the only station common to both our GPS network and the trilateration network of *Harris and Segall* [1987] and *Dong* [1993], an approximate comparison is possible. Between BLHL and Chiches (near POZO), *Harris and Segall* [1987] find a fault-normal velocity of 3 ± 3 mm/yr. The fault-normal (N49°E) component of our residual velocity between BLHL and POZO is 0.5 ± 1.2 mm/yr, which is not significantly different from zero or from the analysis of the 1980–1990 USGS trilateration data [*Dong*, 1993]. A less direct comparison involves lines spanning the SAF, such as BLHL to FIBR, almost 50 km off the fault on the east side. For this line, we find 3.6 ± 1.0 mm/yr of residual fault-normal compression, which is less than the 6.1 ± 1.7 mm/yr rate of residual fault-normal shortening between BLHL and a point 10 km east of the SAF estimated by *Harris and Segall* [1987] but greater than the value inferred by *Dong* [1993]. A balanced cross section including this area, but extending offshore across the trace of the Hosgri fault system, yields 6–13 mm/yr of shortening [*Namson and Davis*, 1990], apparently indicating more deformation than measured in our network, but distributed over a larger region.

Santa Maria Fold and Thrust Belt

Of the five stations in the Santa Maria Fold and Thrust Belt, LOSP and MADC exhibit residual motions significantly different from zero at 95% confidence (Figure 5). In particular, the residual

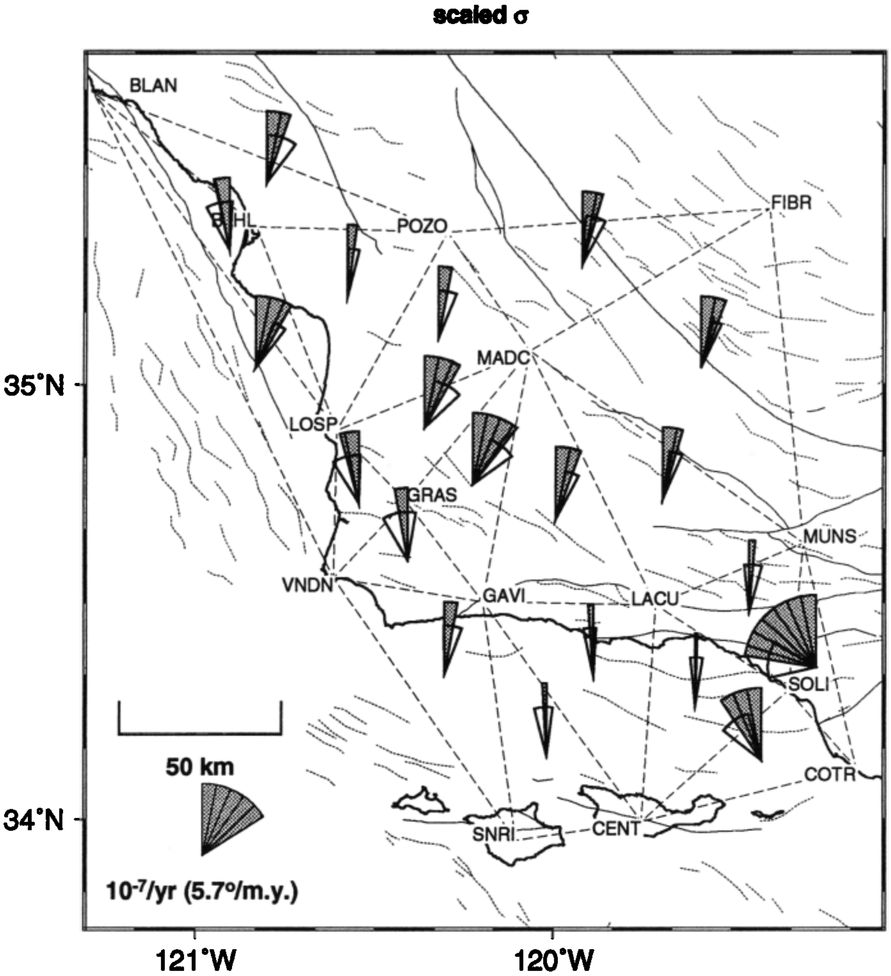

Fig. 9. Average rotation rates inferred from the residual velocity field for the area around Vandenberg. The rates are shown as gray fans, in which each fold denotes 20 nrad/yr (1.1°/m.y.). The white wedge represents plus or minus one standard deviation, after the formal uncertainties have been scaled by a factor of two. If the uncertainty on the rotation rate exceeds 88 nrad/yr (5°/m.y.), the rotation rate is not shown. Values and uncertainties for all triangles are given in Table 6.

velocity of MADC with respect to VNDN implies 2.3 ± 0.8 mm/yr of shortening and 3.1 ± 0.8 mm/yr of right-lateral strike slip in the frame defined by the local (N60°W) strike of the folds. The shortening component can be interpreted in terms of active shortening on the WNW-ESE trending folds in the area. The rate of shortening is compatible with the geological rate of 2–5 mm/yr estimated from a balanced cross section [*Namson and Davis*, 1990] but smaller than the 6 ± 1 mm/yr estimated by a comparison of GPS and historical survey data [*Feigl et al.*, 1990]. The latter study, however, assumed uniform strain in the SMFTB, no net rotation, and no strain accumulating from the locked SAF. All three of these hypotheses are suspect in light of the spatially varying strain rates (Figure 7), the suggestion of rotation (Figure 9), and the 4 mm/yr of relative motion between VNDN and MADC in our fault model (Figure 3).

The amount of right-lateral strike slip shear, however, is larger than expected, given the lack of faults active in the Quaternary [*California Division Mines and Geology*, 1992]. One explanation would be unmodeled strain accumulation on the SAF; in light of the evidence for a shallower locking depth for the SAF, this explanation seems unlikely. Alternatively, strain accumulation on the offshore Hosgri fault [*Hall*, 1978; 1981] may be indicated, although modeling this fault seems to require an implausibly deep locking depth (> 25 km) and/or a rapid slip rate (> 10 mm/yr) to explain the fault-parallel residual velocities at POZO and MADC. A geometrically simple solution would be right-lateral shear accumulating on a NW striking fault between VNDN and the Southern Coast Ranges (LOSP, BLHL, MADC, POZO, and BLAN), but there is little geological evidence for Quaternary activity on such an onshore structure [*Sylvester and Darrow*, 1979; *Clark et al.*, 1984; *Pacific Gas and Electric*, 1988]. An additional possibility is that our model of elastic strain accumulation on the SAF is too simple because it neglects viscoelastic effects through the earthquake cycle. But since the uncertainties are a substantial fraction of the residual velocities in this region, we postpone interpretation of our results in this area until we have more data. A program to continue and densify the measurements is currently underway.

Santa Barbara Channel

Across the Santa Barbara Channel, we find up to 4.9 ± 1.0 mm/yr of residual shortening (CENT–LACU in Figure 5), with the principal compressive strain oriented NE-SW (Figure 7). Similarly, a combination of trilateration and GPS measurements indicates northeast trending convergence of 6.4 ± 0.9 mm/yr between 1970 and 1988 [*Larsen et al.*, 1993]. Part of this deformation may be attributable to fault-bend folding on the offshore Oak Ridge and Blue Bottle trends described by *Shaw and Suppe*

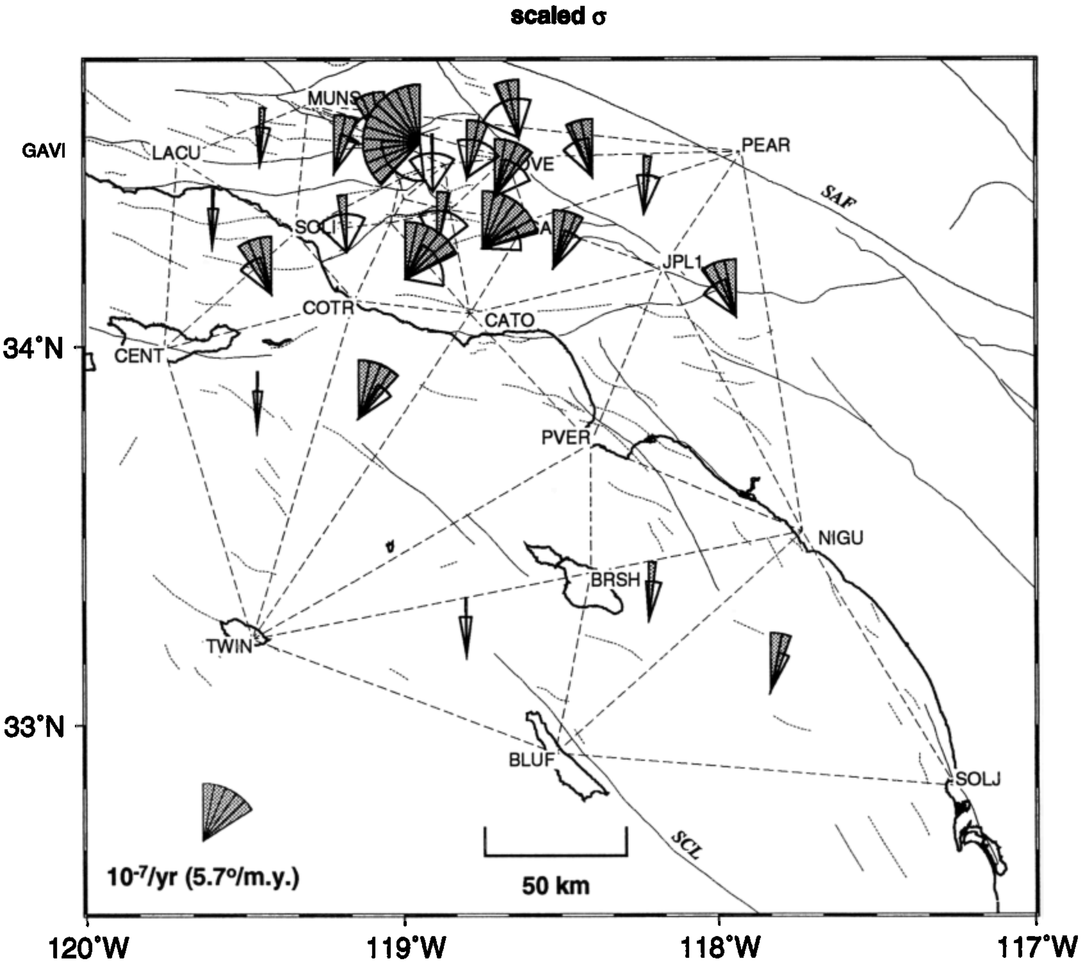

Fig. 10. Average rotation rates inferred from the residual velocity field for the area around Palos Verdes. Plotting conventions as in Figure 9.

[1991]. In the central third of the channel, in the area bounded by Santa Cruz Island (CENT), La Cumbre Peak (LACU), and Gaviota Peak (GAVI), we find more left-lateral shear across a vertical plane striking ENE than we do to the east, where the strain is essentially uniaxial. *Larsen et al.* [1993] suggest a change in the deformation pattern between these two regions, with uniaxial strain to the east and left-lateral strike slip to the west. Our observations are consistent with a change between the eastern and central thirds of the channel, although we find some dilatational strain, in addition to strike slip, in the central section.

Ventura Basin

The rapid convergence observed across the Santa Barbara Channel continues to the east into the Ventura basin, where the close spacing of the GPS stations allows us to locate large gradients in velocity. The convergence rate across the basin is 5-8 mm/yr [*Donnellan et al.*, 1993, this issue]. The convergence takes place within the narrow basin, resulting in a maximum shear strain rate of 0.6 ± 0.1 μrad/yr, with the azimuth of maximum compression oriented approximately N-S, averaged over the east and central parts of the basin [*Donnellan et al.*, this issue]. This strain rate is almost twice that associated with the San Andreas fault in this region. The areal dilatation rate, $-5 \pm 1 \times 10^{-7}$ yr^{-1}, is larger in magnitude than any other observed in California. The deformation pattern in this area is consistent with slip on thrust faults, inferred from seismological and geological observations, loading the upper 5–10 km of the faults that bound the basin [*Donnellan et al.*, 1993]. The residual velocities of 5–8 mm/yr across the basin are less than half those proposed previously [*Yeats*, 1983]. One way of reconciling the geologically inferred rates of slip on the faults bounding the basin with the geodetically observed convergence rates is if the faults maintain their (relatively steep) near-surface dips to great depths, rather than flattening out into sub-horizontal décollements [*Yeats and Huftile*, 1992]. Alternatively, the fault geometries used previously could be correct, with an error in the inferred time of deformation (P. Molnar, written communication, 1992).

Los Angeles Basin

The residual velocity of Palos Verdes (PVER) with respect to the Jet Propulsion Laboratory (JPL1), north of Pasadena, implies 0.2 ± 1.2 mm/yr of right-lateral shear and 5.0 ± 1.2 mm/yr of shortening in a coordinate system defined by the local strike of the SAF (N75°W). A balanced geological cross section provides a minimum rate of 3.8–6.8 mm/yr of shortening over the last 2–4 m.y. along a line including, but longer than, the segment between PVER and JPL1 [*T. L. Davis et al.*, 1989]. Assuming uniform strain, the section between PVER and JPL1 is shortening at 2.5–4.5 mm/yr, consistent with our measurement. There are two interpretations of our measurement being near the upper bound of the geological determination. This may mean that the geologic rates are near the upper limit of the published rates and that the structures accumulating strain are nearly completely spanned by this baseline. Alternatively, strain could be accumulating on the frontal fault of the San Gabriel Mountains, as proposed by *Bird and Rosenstock* [1984], although at a rate lower than they proposed. Identification of the features responsible for accommodating the shortening should be possible with geodetic measurements currently underway [*Hudnut et al.*, 1991; *Shen et al.*, 1991].

Possible Time Dependent Complications

The period of our observations between 1986 and 1991 may be considered to be interseismic. During this interval, the only important ($M > 6$) earthquake to occur in the vicinity of our network was the (M_w) 6.9 Loma Prieta event [*USGS Staff*, 1990; *Kanamori and Satake*, 1990]. Although it produced coseismic slip of approximately 2 m [*Lisowski et al.*, 1990], it probably did not displace our benchmarks, all but one of which were over 100 km away. The only station in our network likely to have been displaced by the coseismic motion is at Fort Ord, which moved 49 ± 4 mm to the southeast [*Clark et al.*, 1990]. Although such a displacement would ordinarily be resolvable by GPS, it does not appear in our result because our GPS observations at Fort Ord involve different bench marks before (FTOR) and after (FTO2) the earthquake. In the multisession solutions, the positions of the two monuments are not tied together. The velocities of all the marks at Fort Ord (both GPS and VLBI) are assumed to be equal in the preseismic and postseismic periods.

The Whittier Narrows earthquake ($M_w = 6.0$) [*Hauksson et al.*, 1988] event occurred on October 1, 1987, during our survey in the Santa Maria area. Although we made observations following the earthquake, we were unable to find stations which both had been previously occupied and were sufficiently close to the epicenter. The stations at JPL and Palos Verdes, the core sites closest to the epicenter, are too far away to have measurable coseismic displacement.

A more serious time-dependent complication in our analysis may result from the simplicity of the model which we use to remove approximately the effects of deep slip on the SAF. We know that the Earth is not an elastic half-space, and we suspect that faults do not slip with uniform velocity below some locking depth. During the interseismic period, viscoelastic effects are likely to be important. We have chosen to ignore these effects in our simple reference model because the parameters to be used in a more realistic model are not well constrained. Some of the residual velocity field may well result from ignoring these effects.

A time-dependent velocity field during the interseismic interval would result either from temporally varying slip on the fault plane, with more rapid slip immediately following an earthquake [e.g., *Thatcher*, 1983], or by viscoelastic relaxation in an intracrustal or subcrustal asthenospheric layer [e.g., *Li and Rice*, 1987]. *Savage* [1990] has shown that the surface deformation for an elastic lithosphere overlying a viscoelastic half-space can be simulated by an appropriate variation of slip rate on a fault embedded in an elastic half-space. For either model, early in the earthquake cycle, the fault-parallel velocities are greater than the geologic average, while late in the earthquake cycle, the velocities fall behind the geologic average. For some choices of parameters, early in the earthquake cycle, sites near the fault have higher velocities than those farther away; the plot of velocity versus distance from the fault is no longer monotonic, as it is for the simple arc tangent model. In these models, the deep slip velocity that would be inferred from a simple inversion of velocities near the fault would not match the geologically inferred rate, except by coincidence. In addition, the slip rate inferred from observed velocities near the fault would differ from that inferred from velocities observed farther away.

Some of the residual velocities that we find after subtracting the predictions of a simple model of faults slipping at their geological rates from our measured velocities may well be evidence for time-dependent velocities such as those addressed by *Savage* [1990]. Before using our observed velocities to infer reliably the existence of slip on other structures, it will be necessary to address this problem.

Resolution of the San Andreas Discrepancy

The kernel of the San Andreas discrepancy argument is that not all of the deformation at the plate boundary is accommodated on the SAF [*Minster and Jordan*, 1984, 1987]. The part of the Pacific-North America relative motion that is accommodated neither on the SAF nor in the Basin and Range has been named the "modified discrepancy" [*Argus and Gordon*, 1991]. It is the deformation we expect to observe in California. Since it is based on a plate motion model, this vector is a geologic estimate, and thus averages over many seismic cycles. Our geodetically observed vectors, on the other hand, span much less than the typical recurrence time for a great earthquake. To account for the elastic strain accumulation during this inter-seismic time period, we consider the velocity predicted by the reference model of elastic strain accumulation due to deep slip on known faults. The velocity estimates from these three sources, geodetic observation, elastic modeling, and geological estimation, can be compared to describe the partitioning of the Pacific-North America motion.

The first question that we address is how much of the motion between the Pacific and North American plates occurs on shore. In Figure 11a, we compare the geodetic estimate and two geological values from plate motion models for the motion of Vandenberg (VNDN) with respect to North America. The geodetically observed velocity of VNDN is within the 95% confidence ellipse for the values predicted by both the original and the rescaled (slower) NUVEL-1 plate motion models. From this we infer that the bench mark at VNDN is riding on the Pacific plate to within 3 mm/yr. Although the geodetic observation is closer to the rescaled NUVEL-1 velocity than to the original NUVEL-1 value, we cannot reject the original value with any reasonable degree of confidence. Similarly, the NUVEL uncertainties are large enough to allow some 1–2 mm/yr of motion offshore of Vandenberg. The relative motion between VNDN and the southern Channel Islands (Figure 4) suggests that this is the case, although the magnitudes of their relative velocities are less than the uncertainties in the plate rates. Since we have no stations in the Pacific Ocean offshore of Vandenberg, the only other measurement bearing on this problem is the 3.0 ± 0.3 mm/yr of change in distance between VNDN and Kokee Park, Hawaii, a station presumably on the Pacific plate. Although this result is suggestive of deformation offshore of VNDN, it may also be due to volcanic deformation at Kokee, local instabilities at either site, or tropospheric biases in Hawaii. The value of 3 mm/yr, then, is best interpreted as the uncertainty with which we can state that VNDN rides on the Pacific plate and that the "missing" motion occurs between VNDN and North America.

The question then becomes, how is this motion distributed? To address this question, we compare the observed and modeled

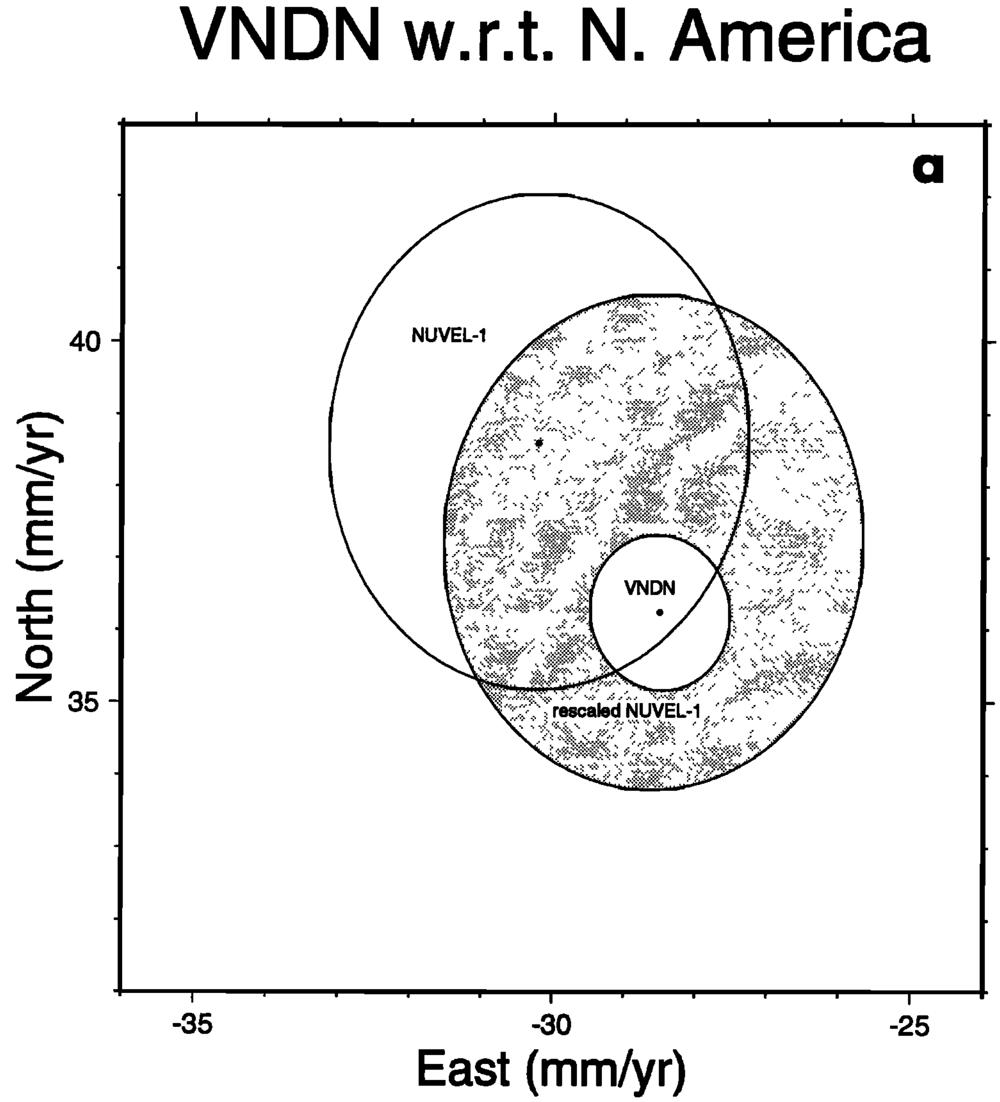

Fig. 11. Partition of the relative velocity between the North America and Pacific plates. (*a*) Three estimates for the total velocity of the Pacific plate with respect to North America: original NUVEL-1 (large white ellipse), rescaled NUVEL-1 (gray ellipse), and our geodetic estimate for Vandenberg (VNDN). (*b*) Three vector sums for the partition of this total velocity, plotted with respect to Vandenberg: geodetic observations (light gray ellipses, with station names labeled in roman text at right), geologic estimates (open arrows with open confidence regions and features labeled in italic text at left), and predictions of the reference elastic model (small solid dots connected by dashed lines). The thick solid lines connecting the geodetic observations with the model predictions are thus residual velocities. Finally, the prediction of the rescaled NUVEL-1 model for North America with respect to VNDN is shown at lower right as a large, dark gray ellipse [*DeMets et al.*, 1990; C. DeMets, personal communication, 1993]. Geologic estimates include the conventional value for slip on the San Andreas fault (SAF) from *Minster and Jordan* [1984]; extension in the Basin and Range (B&R) from the geologic estimate (model A) of *Minster and Jordan* [1987]; and right-lateral strike-slip motion in the Eastern California Shear Zone (ECSZ) from *Dokka and Travis* [1990a]. All confidence regions (ellipses and quadrilateral) are 95%.

velocities in Figure 11b. In Figure 11b, all of the velocities are plotted relative to an origin fixed at VNDN. The gray ellipses are the observed geodetic velocities for a series of stations in California. The solid dots connected by a dashed line represent the velocities of the same sites predicted by the reference elastic dislocation model. The solid lines connecting the observed and modeled vectors are residual velocities. They are small, but significant. The velocities calculated from the reference model all fall outside the 95% confidence ellipses for the observed values. The fault-parallel and fault-normal components of the residuals are similar in magnitude and increase to the east. In addition, the differences in observed velocity between LOSP–VNDN, MADC–LOSP, and FIBR–MADC are larger than predicted by the model. These mismatches cannot easily be corrected by fine tuning the fault model, for example, by decreasing the locking depth on the SAF. As described above, an additional fault west and/or south of MADC seems necessary to bring the elastic model into accord with the observations. But in the absence of known geological structures accumulating strike-slip motion between MADC and VNDN, either structures offshore of VNDN or time-dependent effects are also plausible explanations.

The left-most solid dot on the plot represents the velocity of the "Pacific plate", relative to VNDN, predicted by our reference elastic dislocation model. The reference model, using a locking depth of 25 km on the central section of the SAF, predicts almost 1 mm/yr of elastic strain accumulation offshore of VNDN.

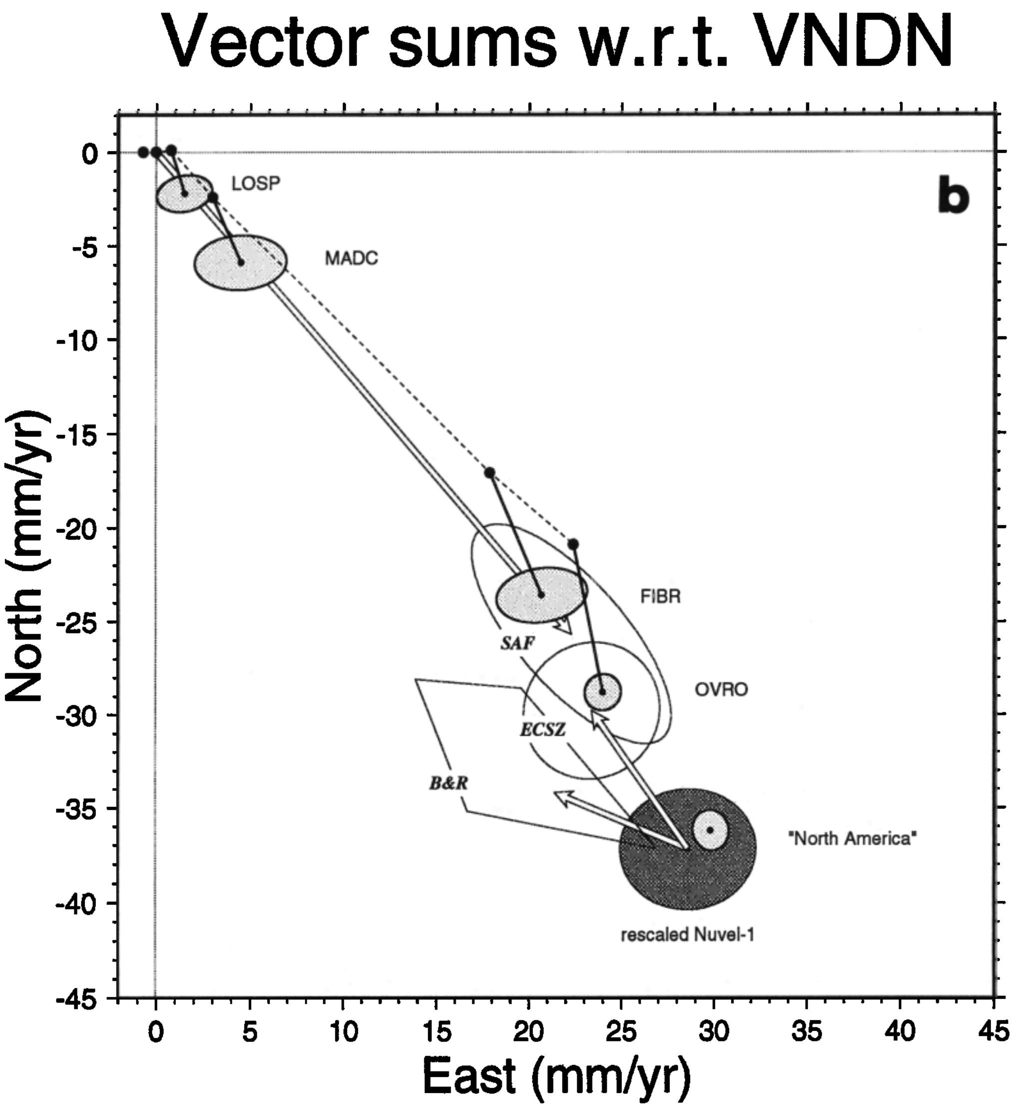

Fig. 11. (continued)

Finally, the small ellipse labeled "North America" represents the observed velocity of the ensemble of sites defining the North American plate with respect to VNDN. It is compatible with the prediction of the rescaled NUVEL-1 plate motion model (large dark gray ellipse), as described above. We note, however, that the NUVEL-1 uncertainties are large enough to include the possibility of 1–2 mm/yr of deformation offshore of VNDN, which we have neglected in this comparison.

A third constraint on how the deformation is partitioned comes from geological estimates, which we summarize by constructing an integral along a path crossing the plate boundary region. Where the path crosses an active structure, the geologically inferred displacement rate and the appropriate strike are added as vector components to the sum. Motions due to block rotations should also be included, although they are difficult to determine from the geologic record. The resulting path integral gives the relative velocity between the endpoints of the path [*Minster and Jordan*, 1984]. The difference between the path integral crossing a plate boundary and the relative velocity vector between the two plates represents the discrepancy vector. The geologic velocity estimates are plotted as open arrows in Figure 11b.

The conventional geological slip rate for the SAF is 34 ± 3 mm/yr at S41 ± 2°E [*Minster and Jordan,* 1984], which we plot relative to VNDN. It is interesting that our elastic dislocation model, which includes deep slip on the SAF, predicts a velocity at OVRO that is comparable in rate (31 mm/yr) but significantly different in orientation (S47E°) from the geologic rate for the SAF. This mismatch is the result of the effects of elastic strain caused by the change of strike of the SAF in the Big Bend region, as well as motion on the Garlock fault.

There are two geological estimates for the velocity to the east of our network. The first applies to a path leaving OVRO to the northeast and represents the extensional deformation in the Basin and Range. Relative to North America, which we plot as the rescaled NUVEL-1 prediction, the Basin and Range moves 8.0 ± 3.3 mm/yr at N64°W ± 10° according to the geologic data in "model A" of *Minster and Jordan* [1987]. The confidence ellipse for this geologic estimate does not overlap the geodetically observed velocity for OVRO. This remaining bit of "discrepancy" can be eliminated with a more northerly azimuth for the Basin and Range vector, as indicated by a VLBI estimate for the velocity of the Sierra Nevada with respect to North America [*Argus and Gordon*, 1991]. It could also be eliminated by including the fault-normal compression we have measured near the SAF.

The second geological estimate involves a path to the south of

OVRO, crossing the Eastern California Shear Zone (ECSZ) [*Dokka and Travis*, 1990a]. The geological estimate of the average slip rate across this structure is 6–12 mm/yr [*Dokka and Travis*, 1990b], which we take to be a 95% confidence interval. Assuming a strike of N35°W± 10° by an eyeball fit, this yields a geologic vector quite similar to the geodetic estimate of 8 mm/yr at N35°W [*Savage et al.*, 1990]. We plot the former quantity as ECSZ relative to the rescaled NUVEL-1 prediction for North America. The 95% confidence ellipse of the ECSZ geologic velocity overlaps the observed geodetic velocity of OVRO, so all the geological deformation along this path seems to be accounted for by the geodetic observations.

The reference elastic model, however, is missing some of the motion captured by the geodetic and geologic estimates. At OVRO, for example, the velocity predicted by the reference model is 7–9 mm/yr short of the geodetically observed value and the ECSZ vector. In this area, the reference model of elastic strain accumulation is oversimplified. It includes neither the ECSZ nor the Basin and Range because we have insufficient information to identify the active structures near OVRO. On the other hand, we can also attribute some of the model's shortcoming to strike-slip motion on structures outboard of MADC and to compressive structures in the vicinity of the SAF, neither of which is included in the simple reference model. Within the context of elastic dislocation models, motion on these structures is sufficient to explain the modified San Andreas discrepancy. We leave more quantitative modeling using simple dislocation models, as well as time-dependent models, to future papers.

CONCLUSIONS

We have developed a new technique to rigorously combine 7 years of VLBI and GPS measurements in a single solution. With it, we have mapped the velocity field in central and southern California with a precision and accuracy as good as 2–3 mm/yr, sufficient to distinguish among some tectonic models.

The dominant signal in the observed velocity field is the shear due to deep slip on the San Andreas and other known faults. After subtraction of a conventional model for the strain accumulation, however, significant shear remains in the residual field throughout the region of our network. This could be due to a combination of an inappropriate choice of model parameters, an oversimplified model, or strain accumulation due to the unmodeled structures such as the San Gregorio-Hosgri fault. Distinguishing among these possibilities should be a high priority for future work.

In addition to unexplained shear, the residual velocity field exhibits significant compressive strain. The Ventura basin, Santa Barbara Channel, Los Angeles basin, and Santa Maria Fold and Thrust Belt are also undergoing active shortening at rates of up to 5 ± 1, 5 ± 1, 5 ± 1, and 2 ± 1 mm/yr, respectively. These rates are consistent with the geological estimates, but tend to fall at the low end of the allowable range. In the southern Coast Ranges, our results corroborate the conclusion of *Shen and Jackson* [1993] that the rate of compression normal to the trace of the San Andreas fault is less than has been proposed on the basis of trilateration measurements. We also find significant compression to the northeast of the SAF.

The rates of rotation about vertical axes in the residual geodetic velocity field differ by up to a factor of 2 from those inferred from paleomagnetic declinations. The reason for the difference probably involves deformation which is nonuniform, either in space or in time.

Our estimates indicate that the "San Andreas discrepancy" can be resolved to within the geological uncertainties of 3 mm/yr by accounting for deformation in California between Vandenberg and the westernmost Basin and Range. Some 1–2 mm/yr of strain accumulation on structures offshore of Vandenberg is also allowed by the uncertainties. South of the Transverse ranges, the accounting must include some 5 mm/yr of motion between the offshore islands and the mainland. The short-term residual velocity field estimated from the geodetic measurements is in good agreement with available long-term geologic rates to within their uncertainties. We therefore have no compelling evidence for invoking changes in the rate of deformation over recent geologic time.

APPENDIX: DATA ANALYSIS

Estimation Strategy

Single-day analysis of the VLBI observations. The VLBI group delay observations are analyzed using the CALC/SOLVK software developed at the NASA Goddard Space Flight Center [e.g., *Ryan et al.*, 1993] and the Harvard-Smithsonian Center for Astrophysics [*Herring et al.*, 1981, 1986, 1990]. For each day, we use a Kalman filter to estimate station coordinates, corrections to IERS Bulletin B values for pole position and the Earth's axial rotation (UT1–AT), corrections to the IAU-1980 nutation series, and stochastic variations in the atmospheric delay and reference clock at each site [*Herring et al.*, 1990]. To avoid distorting the results of our multisession analysis, we perform the single-day solutions with weak constraints on all of the estimated parameters. The VLBI analysis uses 760,521 group delay measurements in 1618 experiments, with typical root-mean-square (rms) scatter of 30 ps (~10 mm) for each experiment.

Single-day analysis of the GPS observations. For each session, we use the GAMIT software [*Bock et al.*, 1986; *King and Bock*, 1993] to analyze carrier beat phase observations. Satellite orbits are obtained by numerically integrating the initial conditions using a force model which includes lunar and solar perturbations, the GEM L2 gravity model [*Lerch et al.*, 1985] truncated to degree and order 8, and a three-parameter model for nongravitational forces. Using these satellite ephemerides, along with nominal values for the site coordinates, values of Earth rotation parameters determined from the VLBI observations, and standard expressions for the precession and nutation, GAMIT computes theoretical values for the carrier phase observations at both the L1 and L2 frequencies for each station-satellite combination. These theoretical values are then subtracted from the observed values to form phase residuals and combined as double differences (between satellites and between sites) in a least squares analysis to estimate station coordinates, orbital initial conditions, and phase ambiguity parameters using the algorithm described by *Schaffrin and Bock* [1988]. Our "observable" is the (doubly differenced) linear combination (LC) of L1 and L2 that eliminates that part of the ionospheric delay inversely proportional to the square of the frequency [e.g., *Bock et al.*, 1986]. Atmospheric effects are treated by estimating the deviation at zenith from the model of *Saastemoinen* [1972], assuming a single set of nominal meteorological conditions (20°C, 1013.25 mbar, 50% relative humidity) at sea level, but accounting for elevation differences among the stations. A fuller description of the theoretical model is given by *Feigl* [1991] and *Murray* [1991].

As is the case for VLBI, the product of the single-session analysis is a set of loosely constrained parameter estimates and their covariance matrix. Before generating such a "loose" solution, however, we must first resolve the phase ambiguities. This is accomplished in a series of four intermediate solutions, performed automatically and sequentially by GAMIT:

1. All parameters are estimated using the LC combination of the L1 and L2 phases. A reference frame is defined by imposing tight constraints on the station coordinates, as described below.

2. With the geodetic parameters held fixed at the values obtained in solution 1, the wide-lane (L2–L1) ambiguity parameters are estimated and, if possible, constrained to integer values. This solution employs the L1 and L2 phases under an ionospheric constraint that varies from 1 to 8 parts in 10^6. If precise pseudoranges at both the L1 and L2 frequencies are available, they are used to help determine the wide-lane ambiguities.

3. With the wide-lane ambiguities held fixed at the values obtained from solution 2, the narrow-lane (L1) ambiguity parameters are estimated, along with all the geodetic parameters, from the LC data. As in solution 1, a reference frame is defined by imposing tight constraints on the station coordinates.

4. With the resolved values of both the wide-lane and narrow-lane ambiguities held fixed to the integer values obtained from solutions 2 and 3, the geodetic parameters are estimated from the LC data.

These four solutions are intermediate steps, performed with the goal of resolving the integer phase ambiguities. The algorithms are those of *Dong and Bock* [1989], except that the values of the geodetic parameters estimated in solution 1 are retained in solution 2. This four-step procedure allows us to resolve more than 90% of the ambiguities in most experiments.

Two additional solutions are neeeded to produce the parameter estimates and covariance matrices for later input into the second (multisession) stage of our analysis. They are performed with orbital and positional constraints that are sufficiently tight to avoid numerical singularity, but sufficiently loose (1 part in 10^5) to avoid contaminating the velocities to be estimated later.

5. The LC solution 1 is repeated via manipulation of the least squares normal equations but with loose constraints on the geodetic parameters. The ambiguity parameters are free to assume real values.

6. Solution 4 with the resolved phase ambiguities constrained to integer values is repeated with loose constraints on the geodetic parameters.

To resolve the ambiguities requires a well-defined reference frame, which we established by constraining the station coordinates in solutions 1, 3, and 4. The values and uncertainties

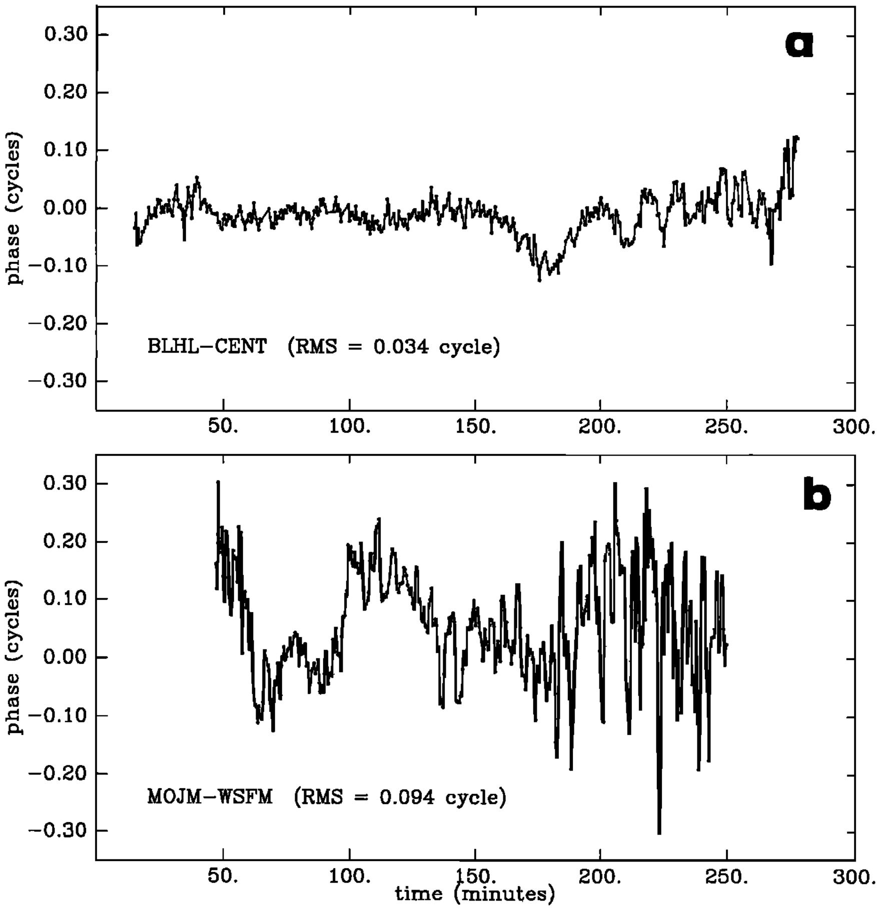

Fig. A1. GPS phase residuals with different noise signatures. The plotted quantity is the residual (observed minus calculated) doubly differenced ionosphere-free ("LC") combination of the L1 and L2 carrier phase. (*a*) For a short (181 km) line between BLHL and CENT, the rms scatter is about 0.034 cycles, or 8 mm. (*b*) For a longer (3904 km) line between MOJM and WSFM, with more multipathing, the rms is larger, about 0.094 cycles (21 mm). Both plots show data from satellites PRN 6 and PRN 11 collected on March 29, 1990.

for these constraints were obtained from a previous multisession analysis of the loose solution 5 with unresolved ambiguities. We applied constraints to the coordinates of all stations, whether in California or elsewhere, thereby minimizing the effect of an error in the coordinates for any one station. For the stations in California, we applied constraints of 10 mm for the horizontal coordinates and 50 mm for the vertical coordinates; for the other stations, we used 50 mm for the horizontal coordinates and 100 mm for the vertical coordinates. In most cases, these values are several times larger than the formal uncertainties obtained from our multisession analysis. We repeat, however, that these tight constraints were only imposed on the intermediate solutions 1, 3, and 4. They were not applied to the solutions 5 and 6 passed to the multisession analysis for estimating velocities. In some cases, our procedure yielded incorrect values for the ambiguities, as indicated by elevated values of χ^2 and/or large differences in position between solutions 5 and 6. In these cases (21 of 113 sessions), we took the conservative approach, and used the real-valued solution 5 for the subsequent estimation of station velocities in the multisession analysis.

A result of the single-day analysis is shown in Figure A1, which provides two examples of doubly differenced, ionosphere-free phase residuals for March 29, 1990. The residuals between the pair of field sites (Black Hill and Center, 181 km apart) have an rms scatter of 0.05 cycles (10 mm), while the scatter for Mojave and Westford is 4 times larger. The difference is probably due to larger unmodeled atmospheric fluctuations and to signal multipathing from highly reflective structures at the VLBI observatories. The unmodeled excursions in phase evident at the tracking sites can systematically affect the estimates of velocity, since the antennas used at these sites, and the sites themselves, have changed over time (Table 3).

An important feature in the residuals is that they are temporally correlated. We accounted for these correlations by assigning large a priori uncertainties to the 30-s samples of the phase observations. The uncertainties are 10 mm for the L1 and L2 carrier phase measurements, equivalent to 64 mm in the doubly differenced ionosphere-free combination. In a slightly different approach, *Larson and Agnew* [1991] accounted for the correlations by compressing the data into 6-min normal points. This is more efficient but may not completely average out the short-period effects of multipath. The scatter in the estimates of relative station positions indicates that the appropriate uncertainty for 6-min samples of the doubly differenced, ionosphere-free combination of the phase measurements is about 0.1 cycles (20 mm) [*Larson and Agnew*, 1991], equivalent to 0.35 cycles (70 mm) for 30-s samples. With this data weighting, the scaled uncertainties for positions estimated from a single session are about 4 mm in the north, 6 mm in the east, and 20 mm in the vertical coordinates, provided that good global tracking coverage is

TABLE A1. Parameter Constraints Used in the Multisession Analyses

Parameter	A Priori	A Posteriori [a]	Stochastic [b]
	Individual California GPS Experiments		
Site positions	10 m	1 m	none
Satellite positions	100 m	1 m	0.1 m/d
Satellite velocities	10 mm/sec	0.1 mm/s	0.01 mm s^{-1} d^{-1}
Eclipsed satellite positions [c]	100 m	1 m	10 m/d
Eclipsed satellite velocity [c]	10 mm/sec	0.1 mm/s	10 mm s^{-1} d^{-1}
Radiation parameters	100%	1%	1%/d
Earth orientation	not estimated		
	VLBI Experiments		
Site positions	10 m	1 m	none
Site velocities	1 m/yr	0.1 m/yr	none
Radio source positions	100 mas	0.1 mas	none
Earth orientation [d]	100 mas	20 mas	10 mas/d
	Global GPS and Combined California Experiments		
Site positions	10 m	1 m	none
Site velocities	1 m/yr	0.1 m/yr	none
Satellite positions	removed [e]		
Satellite velocity	removed [e]		
Radiation parameters	removed [e]		
Earth orientation	100 mas	20 mas	10 mas/d
	VLBI and GPS Combination		
Site positions	10 m	1 m	none
Site velocities	1 m/yr	0.1 m/yr	none
Earth orientation	100 mas	20 mas	10 mas/d

[a] Typical values. In many cases, these values are large because no coordinate system is imposed on the solution. Quantities which are invariant to changes in the coordinate system, such as length and angle, are typically better determined by two orders of magnitude.

[b] All stochastic parameters are modeled as random walks for which the noise in the process increases as the square root of time (see *Herring et al.*, [1990] for dicussion)

[c] This level of constraint is fairly loose and almost uncouples one day's orbit from the next. A daily perturbation of 10 m is between 10 and 100 times larger than the level we expect for most satellites [*Herring et al.*, 1991]. It helps to avoid the effect of unmodeled nongravitational forces on the satellite, especially when it spends part of its orbit in Earth's shadow (in "eclipse").

[d] Earth orientation values are given in milliarc seconds (mas).

[e] For these cases, the rows and columns of the covariance matrix for these parameters are removed before incorporation of the solution in the Kalman filter. This procedure is equivalent to allowing the parameter to adjust freely with no further constraints placed on its value.

available, and phase ambiguities are resolved [*Larson and Agnew*, 1991; *Murray*, 1991].

Multisession analysis. We combine the single-day VLBI and GPS solutions using a Kalman filter program (GLOBK) developed for the combination of VLBI experiments [*Herring et al.*, 1990; *Herring*, 1993; *Dong*, 1993]. Our combined solution contains the positions and velocities of 212 stations obtained from 1797 sessions which collected a total of ~5,300,000 VLBI group delay and GPS doubly differenced carrier phase measurements.

Because each single-day solution is generated with loose constraints on all of the parameters, we are free in the multisession analysis to impose constraints on any of the parameters. Imposing these constraints is a rapid procedure with the GLOBK Kalman filter, allowing us to test the effects of different constraints efficiently. For example, we can constrain the initial conditions and nongravitational force parameters of the GPS satellites to define a single dynamical arc over several days or to allow the orbit to vary stochastically from day to day.

Table A1 lists the a priori and typical a posteriori values of the uncertainties for all parameters estimated in the multisession analyses. For most parameters, the a priori constraints were sufficiently loose that they imposed no significant bias on the estimates. The most notable exceptions are for GPS orbital parameters. For satellites not eclipsed during an observation period, we treated the satellite state vector (initial Cartesian position and velocity) as a random walk with the stochastic process noise set so that the position and velocity can change each day by 10 cm and 0.01 mm/s, respectively. Solar radiation pressure scale factors (direct and Y-bias) were also tightly constrained to allow 1% changes per day. For eclipsing satellites, the constraints on the state vectors were loosened to 10 m/d and 10 mm s^{-1} d^{-1}, effectively decoupling one day's orbit from the next.

The strongest constraints, however, were placed on the station positions and velocities. We varied the station constraints (Table A1) to perform three different solutions, which we used for different purposes: (1) to define a terrestrial reference frame, (2) to establish a set of a priori coordinates sufficiently consistent for resolution of GPS phase ambiguities, and (3) to provide the most robust estimate of the station velocities. For succinctness, we call these solutions "frame," "coordinate," and "velocity" solutions, respectively.

The first step in the frame solution used only VLBI data to define a terrestrial reference frame. Because of the weak

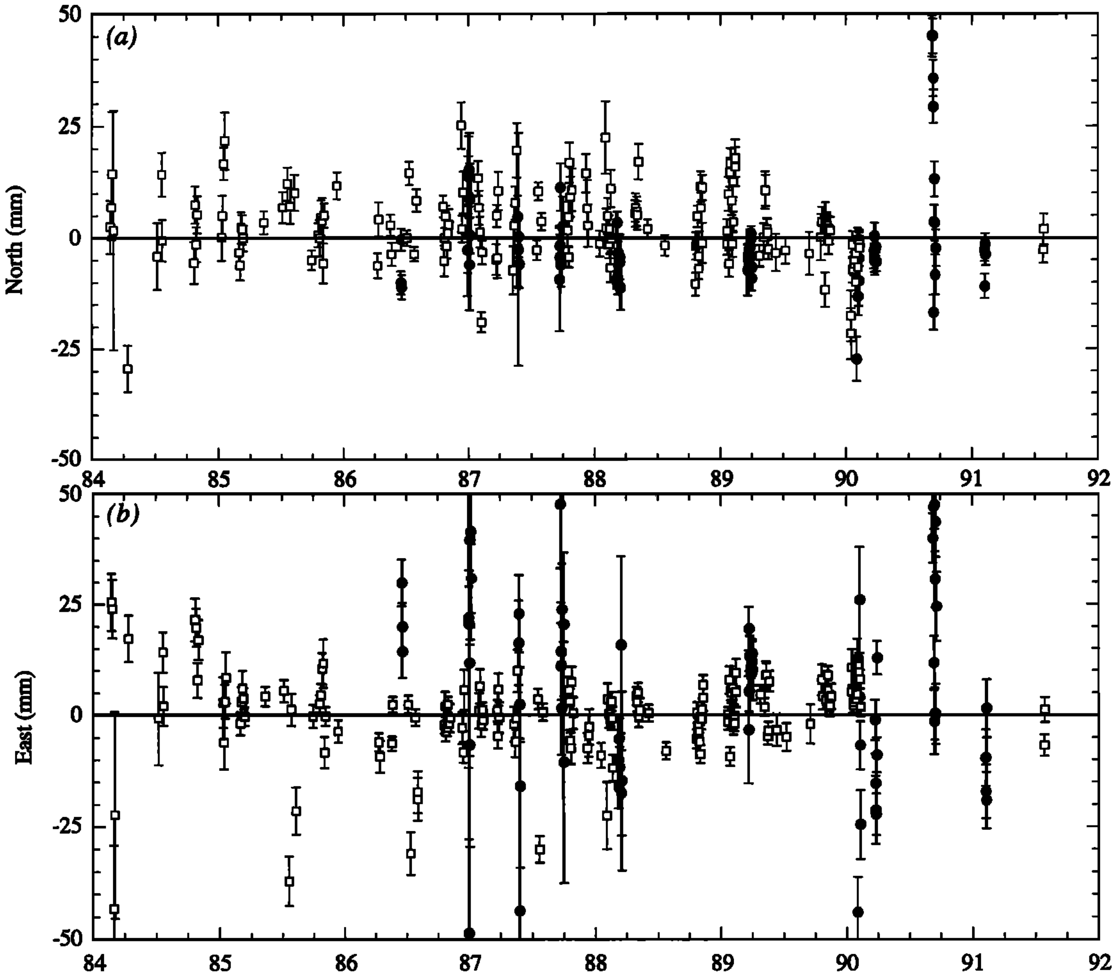

Fig. A2. Evolution with time of the (*a*) north, (*b*) east, and (*c*) vertical components of the relative position vector between Mojave (MOJA) and Vandenberg (VNDN) as determined by GPS (solid circles) and VLBI (open squares). The velocity estimates from the coordinate solution have been removed (28.60, –25.77, and 2.99 mm/yr respectively) and are represented by the horizontal solid line. There have been no offsets introduced into the horizontal coordinates. As discussed in the text, vertical discontinuities corresponding to changes in antennas at Mojave have been removed from the GPS results at 1986.9, 1988.6, and 1989.5.

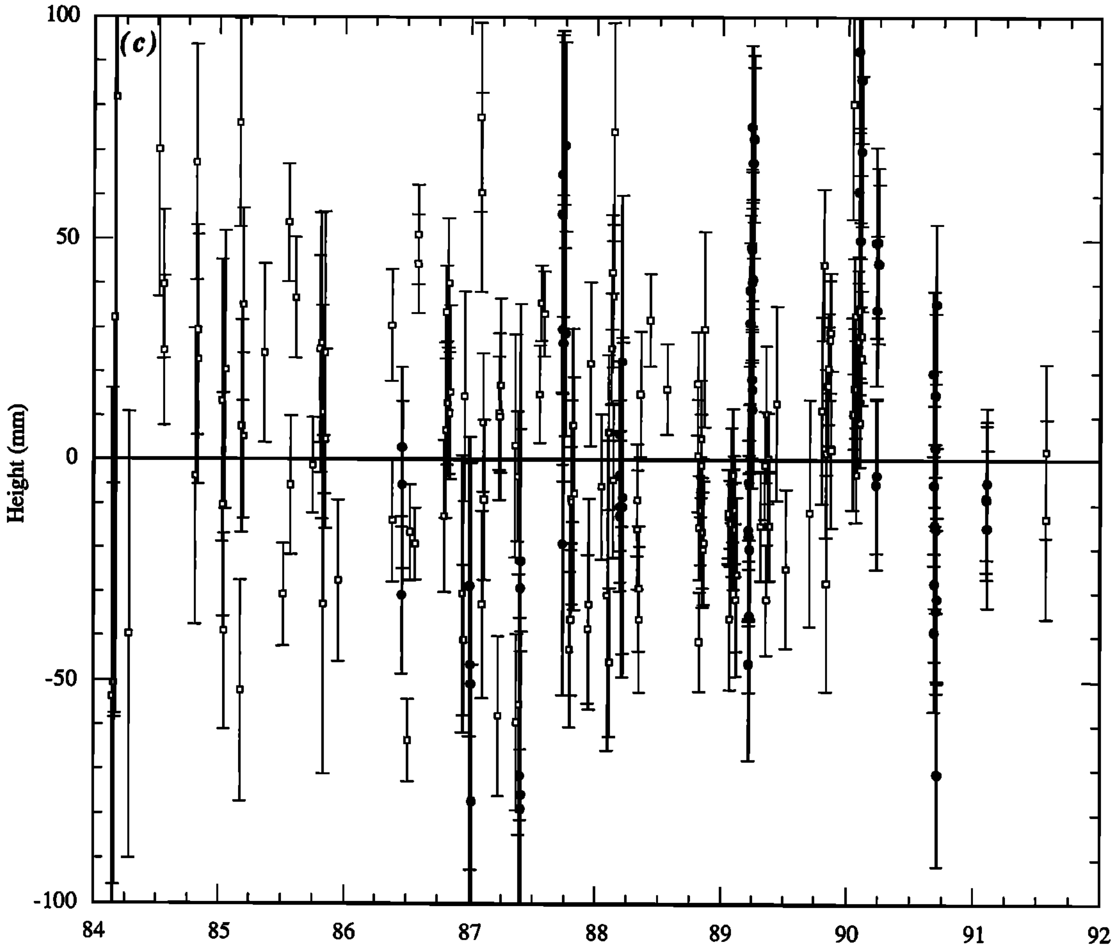

Fig. A2. (continued)

constraints imposed on the VLBI solution, the reference frame for the VLBI analysis is initially only weakly constrained. The weakly defined frame has effectively a twelfth-order rank deficiency; three translations, three rotations, three translation rates, and three rotation rates. To resolve the rank defiency in rate, we determined the three translation and three rotation rates between the weakly constrained frame and our realization of a North American fixed reference frame by minimizing the horizontal velocities in the North American frame of 10 North American VLBI sites (Haystack, Westford, Richmond, Gilmore Greek, Nome, Yuma, Greenbank, Pictown, Flagstaff, and Platteville). To resolve the rank defiency in position, we estimated three rotation and three translation parameters by minimizing the differences between the horizontal coordinates of the same 10 VLBI sites in our frame and the ITRF-1991 reference frame. This latter step does not affect the velocity solution.

In the next step, combining the VLBI and GPS analyses, we adopted this reference frame by fixing the horizontal velocities of three sites (Fairbanks, Westford, and Wettzell) to their VLBI values and constraining the relative positions and velocities of one or more VLBI and GPS monuments at these same locations. This realization of the North American plate is independent of any global plate motion model.

For the coordinate solution, we applied constraints on the horizontal components of the station position and velocity parameters. This imposed the "ties" (vectors) between the multiple benchmarks and antenna phase centers located at the same site. In the coordinate solution, ties were imposed in both horizontal position and velocity. The ties in position have been established by terrestrial surveys. The ties in velocity allow no relative motion between neighboring benchmarks. For example, we assumed that the five different monuments at Westford, Massachusetts, are connected to the same rigid block.

For the velocity solution, we imposed ties in horizontal velocity but not position. The only exception was for Mojave, where we tied the horizontal coordinates of the VLBI and GPS antennas together. Although avoiding the ties in position omits some information, it avoids the (unfortunately likely) possibility of contaminating the estimates of the station velocities with an erroneous tie. The velocity field, shown in Figure 2 and Table 4, yields the relative velocities we interpret in the text. As discussed below, the velocity solution turns out to be quite similar to the coordinate solution.

Discussion of Geodetic Quality

To assess the accuracy of the velocity field given in Table 4, we need to know the temporal and spatial nature of the error spectra of position determinations. In general, these spectra are unknown and difficult to determine. We can, however, examine several statistics from our analysis in an attempt to assess the likely magnitudes of the errors. The components of the error spectra most necessary for assessing the velocity field uncertainty are those with temporal scales comparable to the total duration

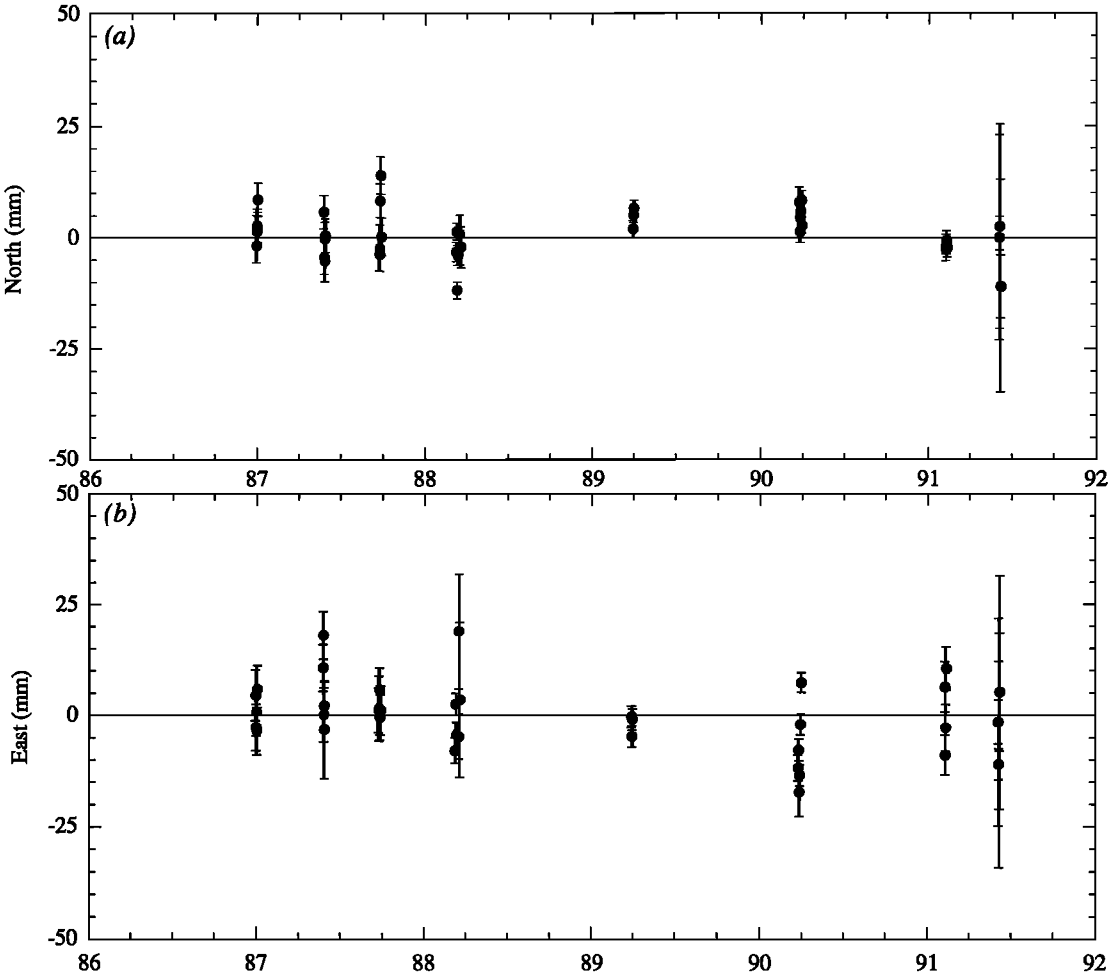

Fig. A3. Evolution with time of the (a) north, (b) east, and (c) vertical components of the relative position vector between Vandenberg (VNDN) and Santa Cruz Island (CENT). The velocity estimates from the coordinate solution have been removed (1.94, −2.64, and 2.34 mm/yr, respectively) and are represented by the horizontal solid line.

(~5 years) and separation (~1 year) of our experiments, and at spatial scales comparable to the baseline lengths in California (50–500 km). Since there is no redundancy in the measurements at these time intervals, we are forced to extrapolate from statistics for shorter time intervals. In doing so, we assume that the noise processes are stationary. This assumption is difficult to justify because there has been an evolution of both the number and type of receivers and satellites over the duration of our data set. There is greater spatial than temporal redundancy in our data, but the most reliable statistics are computed using the entire network. The assumption of spatial homogeneity is also difficult to justify since the velocities between sites separated by larger distances are more likely to be affected by the projection, through the orbits, of the error at the tracking sites than velocities between closely spaced sites.

Short- and long-term precision. In order to assess the precision of our estimates of relative station position, we evaluated their scatter from day to day and year to year. To estimate the scatter, we performed a series of multisession analyses in which we allowed the coordinates of California stations to vary stochastically from day to day or experiment to experiment. In these analyses, the coordinates of all stations outside California were tightly constrained at their values from the coordinate solution. For the GPS experiments, a Kalman filter back solution was necessary in order to apply the appropriate stochastic constraints to the orbital parameters.

Figure A2 shows the behavior of the VLBI and GPS estimates for the north, east, and vertical coordinates of Mojave with respect to Vandenberg, the most frequently observed, and one of the longest California baselines (350 km). The weighted means from the VLBI and GPS estimates differ by 2.8 mm in the north and 9.1 mm in the east, slightly larger than we would expect from errors in the terrestrial survey ties. The height differences are much larger, as discussed below.

To quantify the scatter, we present two statistics: the weighted root mean square (wrms) scatter (often called repeatability), the value of $\sqrt{\chi^2/f}$ (where χ^2 is the chi-square statistic, and f is the number of degrees of freedom). In the north component, the wrms about the weighted mean is 6.9 mm for 150 VLBI sessions and 12.0 mm for 81 GPS sessions. In the east component, the wrms is 6.3 mm for VLBI and 18.0 mm for GPS; in height 27 mm for VLBI and 49 mm for GPS. For both techniques, Figure A2 shows evidence of both short-term and long-term scatter exceeding the formal uncertainties of the estimates. For the VLBI sessions the values of $\sqrt{\chi^2/f}$ are 2.2 in the north, 2.5 in the east, and 1.8 in the height; for the GPS experiments the values are 4.0 in the north, 3.3 in the east, and 2.2 in the height. These values are higher than normal for GPS and VLBI baselines, probably due to unmodeled

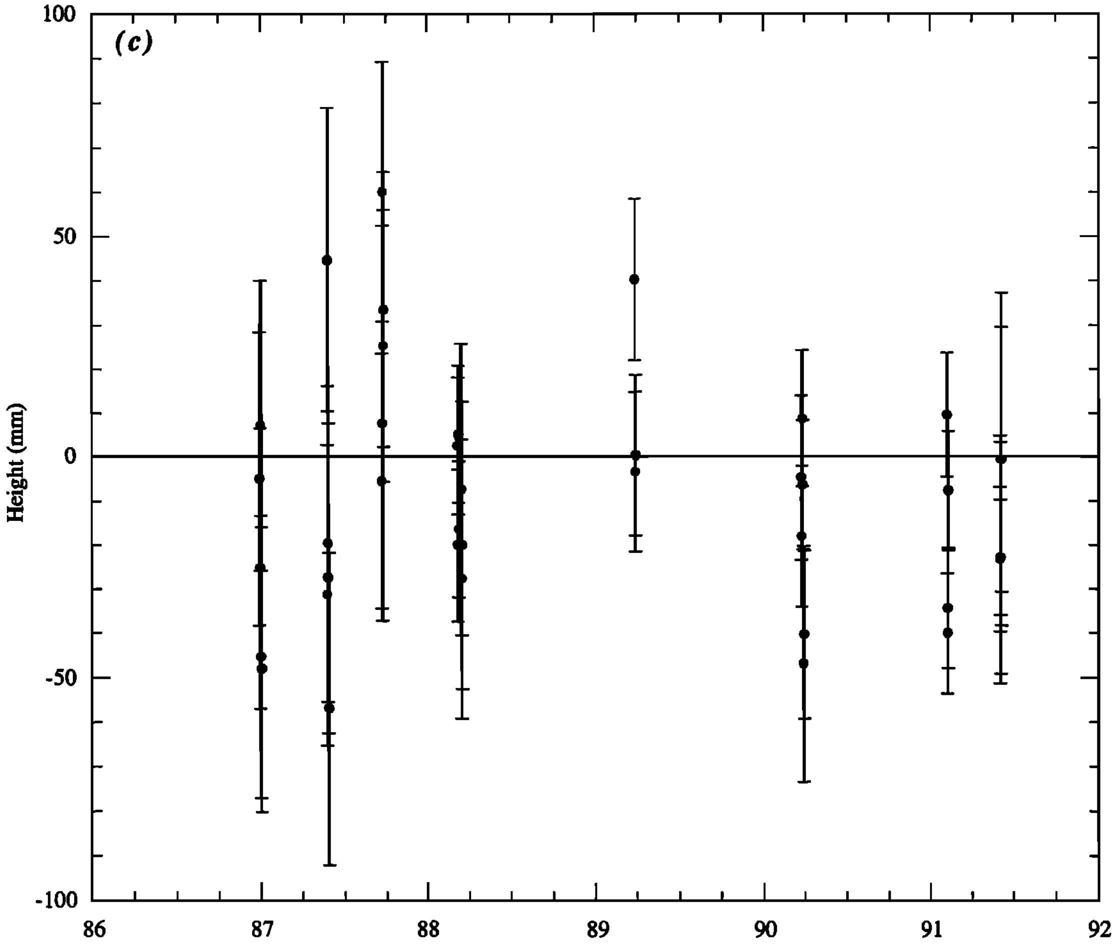

Fig. A3. (continued)

tropospheric effects at Vandenberg, a coastal site subject to atmospheric gradients.

Figure A3 shows the behavior of the estimated coordinates of site Center (CENT) on Santa Cruz Island, with respect to Vandenberg, 101 km distant. For 41 sessions of data, the wrms scatter is 5.0 mm in the north component, 6.8 mm in the east, and 22.0 mm in height. The smaller scatter in the east and vertical components, compared with the Vandenberg–Mojave baseline, is typical for the more closely spaced sites in our GPS core network. For this baseline, phase ambiguities were resolved more consistently than for the longer baselines.

Table A2 summarizes the statistics measuring the short-term precision of the GPS and the long-term precision of both the GPS and VLBI experiments. For each GPS experiment, we list the weighted rms and $\sqrt{\chi^2/f}$ for the north, east, and vertical components of the observed baselines. We also measure the scatter's dependence on baseline length by the slope with which the scatter increases as a fraction of interstation distance. For all experiments except 1 and 18, the short-term scatters are less than ~6 mm in the north component, ~10 mm in the east, and ~30 mm in the vertical, with average values of 4 mm in the north, 7 mm in the east, and 20 mm in the vertical. Most values of the $\sqrt{\chi^2/f}$ statistic for the individual experiments are between 0.8 and 1.5, indicating that the assigned measurement uncertainty is appropriate for the short-term scatter in the estimates. For the major experiments that included widely spaced sites, the baseline dependent term of the scatter is less than 1 part in 10^8 in length.

The multisession analysis has produced good GPS repeatability even for those experiments with few regional sites (7, 8, 9, 15, 16, 17) or poor global tracking (2, 3, 7, 8, 9). The only experiments with wrms scatters in the horizontal coordinates greater than 10 mm were 1 and 18. Experiment 1 (December 1986) had no sites outside California, so the uncertainties for all the baseline estimates are anomalously large. The scatter in Experiment 18 may have been increased by incomplete modeling, for receivers with different sampling times, of variations of the satellite clocks imposed by Selective Availability [*Feigl et al.*, 1991].

The last two entries in Table A2 give the long-term repeatabilities for both GPS and VLBI. For VLBI these values are computed from the scatters in each 24-hour session. The values of the wrms scatter are similar to those obtained for the Mojave-Vandenberg baseline (7 mm for the north component, 6 mm for the east, and 38 mm for the vertical), and the $\sqrt{\chi^2/f}$ is about 1.5. For GPS, we computed the mean values and their uncertainties from each 3- to 5-day experiment and used these values to determine the long-term scatter (Figure A4). The wrms values are similar to the averages for short-term scatter (4 mm in the north, 6 mm in the east, and 23 mm in the vertical), but the values of the $\sqrt{\chi^2/f}$ statistic are about twice those for the individual experiments. This suggests that there is a systematic component of the error within each experiment that is comparable to the short-term scatter and that the noise spectrum is likely to be red; that is, the noise power is larger at low frequencies than at high frequencies. The $\sqrt{\chi^2/f}$ obtained from the long-term scatters is about 1.5 for

TABLE A2. Short-Term and Long-Term Scatter of GPS and VLBI Experiments

			North			East			Up		
Experiment	Year	Number of Lines[a]	wrms[b], mm	ppb	$\sqrt{\chi^2/f}$	wrms, mm	ppb	$\sqrt{\chi^2/f}$	wrms, mm	ppb	$\sqrt{\chi^2/f}$
00	86.5	118	2.5	−1	1.0	1.9	4	0.5	13.4	17	0.6
01	87.0	35	8.0	33	1.2	12.4	34	1.0	31.6	25	1.5
02	87.1	67	4.6	2	0.9	7.8	26	0.8	26.2	42	1.2
03	87.1	115	2.9	3	0.6	5.6	5	0.7	20.0	16	0.5
07[c]	87.5	15	3.2	0	0.7	9.9	−1	1.2	26.7	6	0.7
08	87.8	36	5.3	3	0.9	7.8	28	0.8	33.7	69	0.9
09	87.9	38	5.5	43	0.8	4.3	16	0.6	18.8	45	0.7
10	88.3	46	2.2	0	1.0	3.5	2	1.2	8.8	1	0.5
11	88.3	79	3.0	1	0.8	4.1	3	0.8	21.1	3	0.7
13[c]	89.3	36	2.9	1	1.1	6.4	11	1.7	23.1	−17	1.2
14	89.3	78	2.9	3	1.6	3.7	1	1.5	24.2	−1	1.4
15	89.3	15	3.5	0	1.6	2.7	0	1.0	38.6	−26	2.6
16	89.3	36	3.1	5	1.4	6.8	36	2.2	20.4	−4	1.1
VF1	90.1	18	4.7	0	1.5	4.5	−3	1.2	16.4	−6	1.2
17[c]	90.3	29	4.3	1	1.5	7.0	10	1.6	18.5	15	1.1
18[c,d]	90.3	210	3.6	6	1.0	13.2	37	2.1	24.5	26	1.0
VB1[c]	90.5	65	4.5	10	2.3	5.7	14	2.1	26.0	55	1.8
VF2	90.8	33	4.5	3	1.8	4.2	2	1.4	17.4	49	0.8
20[c]	91.2	136	2.6	1	1.0	6.9	5	1.2	12.7	2	0.8
SB1	91.5	214	5.5	3	0.6	10.1	19	0.6	23.3	21	0.7
VB2	92.5	153	4.3	7	2.2	5.5	16	2.5	24.0	45	1.8
All GPS		156	3.6	2	2.6	5.8	25	2.5	23.0	−11	2.4
All VLBI		90	7.1	−1	1.4	5.5	2	1.5	38.4	−7	1.3

[a] For individual experiments, all baselines less than 500 km in length and which were measured at least twice are included in the calculations of the wrms and $\sqrt{\chi^2/f}$. For the last two entries, at least three measurements are required.

[b] For individual experiments, the wrms and $\sqrt{\chi^2/f}$ are computed about the mean length for each session. For the last two rows, the rms and $\sqrt{\chi^2/f}$ are computed about the best fitting straight line. The length-dependent part of the wrms is given in parts per billion (ppb) of baseline length.

[c] For these sessions, biases are not resolved correctly on some days (as judged by anomalous coordinates relative to the solution with real-valued ambiguities) and the solution with real-valued ambiguities is used in the multisession analyses. This occurrs for 21 sessions, while the biases are correctly resolved for the other 113 sessions.

[d] Only 2 of the 4 days of this experiment are included in the analysis.

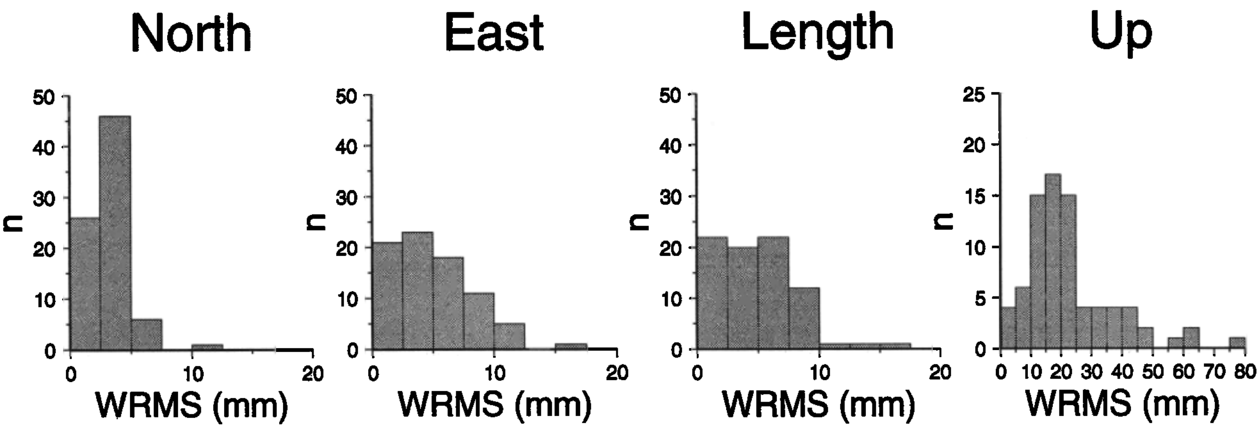

Fig. A4. Histogram of long term scatter for the length, north, east, and vertical components of the GPS-estimated interstation vectors. The values represent the wrms scatter about a straight line estimated for each component. Only stations in California observed over an interval greater than 1.5 years are included.

VLBI and 2.5 for GPS; and the $\sqrt{\chi^2/f}$ of the combined multisession solution (which accounts rigorously for all the correlations among the estimated quantities) is 1.9. These statistics indicate that doubling the formal standard deviations from the combined analysis yields realistic uncertainties if the noise spectrum is flat between 1 and 5 years. Though we doubt that this is strictly true, we have computed the statistic at the longest possible sampling times while averaging as much of the high-frequency noise as possible.

Another approach to calibrating the uncertainties is to compare different solutions. For example, in Figure A5 we show the differences in the estimated velocities, relative to Vandenberg, between the velocity and the coordinate solutions. The largest difference at any of the core sites is 2.5 mm/yr, with the typical

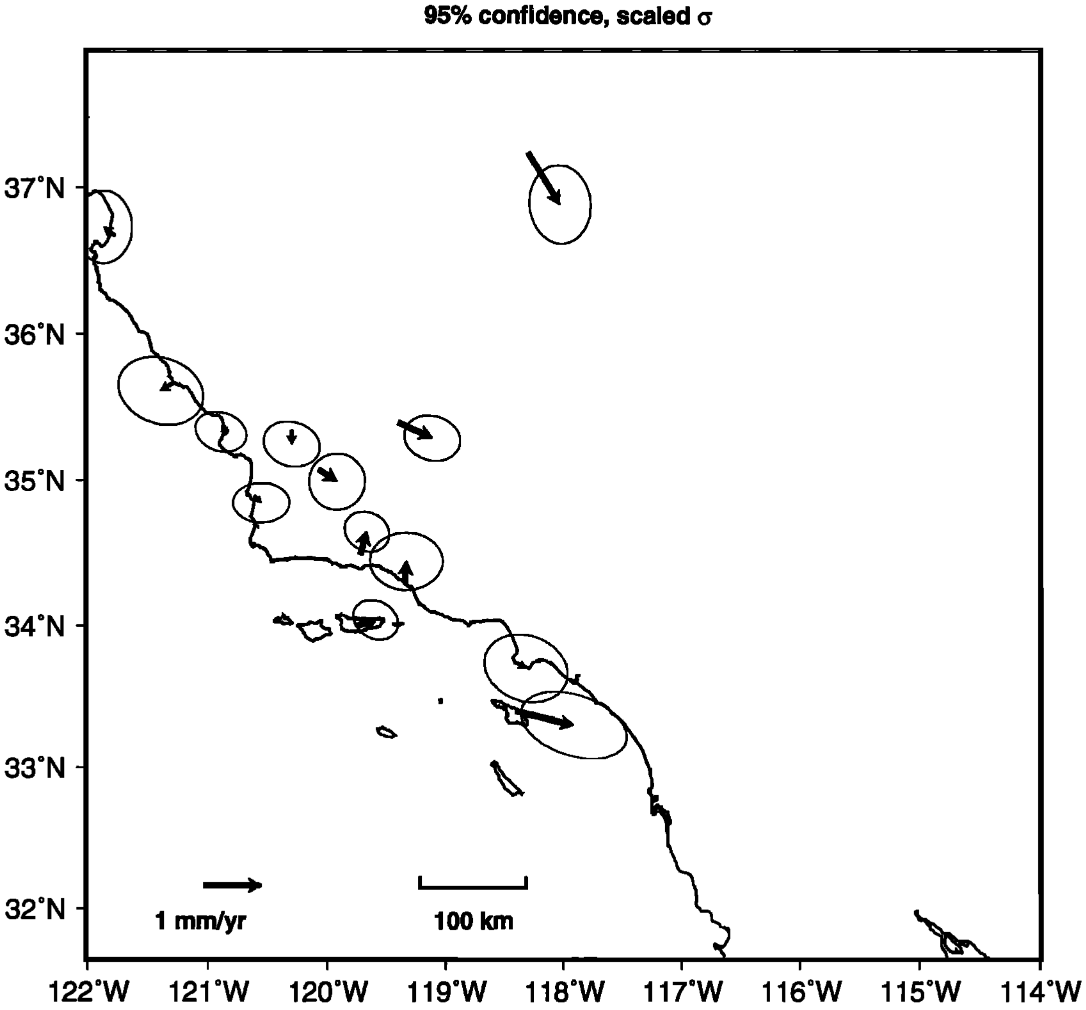

Fig. A5. Differences in velocity estimates, relative to Vandenberg, between the velocity and coordinate solutions for the "core" sites. The ellipses denote the area of 95% confidence for the difference between solutions, after accounting for correlations [*Dong*, 1993] and scaling by a factor of 2, as described in the text. Note that the velocity scale is increased relative to the other figures.

difference being 1 mm/yr. Although these differences could be due to an erroneous tie at any of the common VLBI and GPS sites, they could also indicate large-scale systematic errors in the GPS and VLBI solutions. Such systematic errors might be due to incomplete dynamical models of the satellite orbits, deviations of the phase centers of the GPS receivers, and deformation of the VLBI antennas. Doubling of the formal standard deviations helps to account for these effects in our uncertainties.

As an additional test, we performed an analysis in which the VLBI and GPS velocities in California, except at Mojave, were separate parameters. Constraints on the differential position, where available, and velocity were applied at all sites outside California. The velocities estimated at eight sites with both VLBI and GPS observations are shown relative to the joint GPS+VLBI velocity solution in Figure A6. The differences in velocity estimated by the three solutions are between 1 and 5 mm/yr in both horizontal components. Compared to the joint GPS+VLBI solution, the GPS-only estimates (open arrows) show larger differences in the east component than in north, while the opposite is true for the VLBI-only estimates (solid arrows). The differences are significant at OVRO and VNDN. At the other six stations, the confidence ellipses for the GPS-only estimates, calculated at 95% confidence after doubling the standard deviations, include the VLBI-only and the joint GPS-VLBI estimates. This comparison provides independent evidence that the scale factor derived from our repeatability analysis is not overly optimistic.

Estimates of the vertical component. For both global and regional networks, the relative vertical coordinates of GPS stations are less accurate than the horizontal coordinates. The formal uncertainties in the vertical coordinates are about a factor of 2 larger than for the horizontal, since the observations can be made only in the hemisphere above the horizon and there is a high correlation between estimates of atmospheric parameters and the vertical coordinates. There is often an additional, systematic, component to vertical error introduced by phase center variations of the antenna. This is most problematic when different antennas are used at each end of the baseline, but also important for similar antennas observing at large spatial separations. Finally, ties between the GPS and VLBI antenna phase centers and ground marks are almost invariably less certain for the vertical than the horizontal directions, both in a formal sense and in the likelihood of blunders in the measurements (see, e.g., appendix A of *Murray* [1991] for a discussion of the survey at Kokee Park, Hawaii).

Our attempt to incorporate survey ties at the Mojave site illustrates the potential magnitude of the vertical problem. The June 1986 (experiment 0) observations were made with a TI 4100

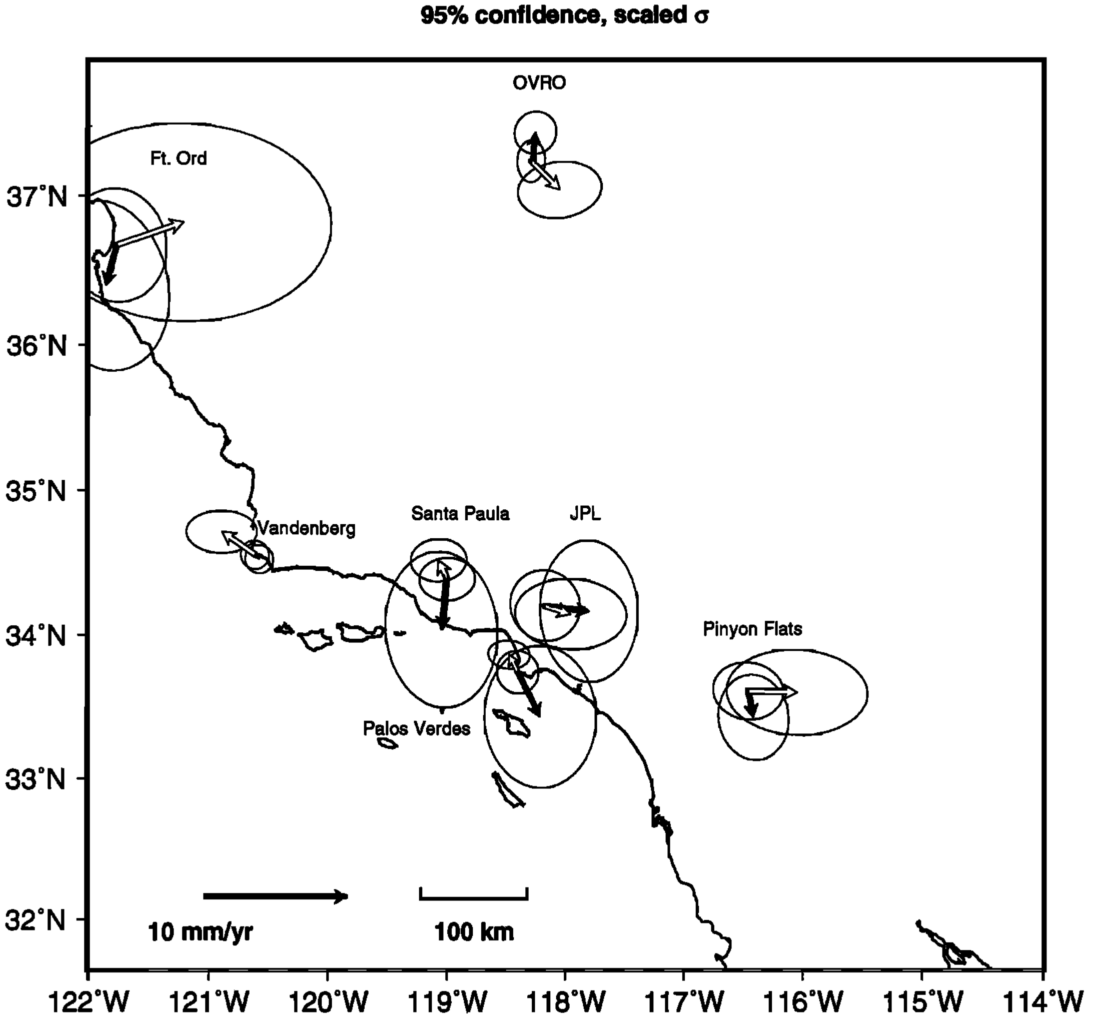

Fig. A6. Comparison of GPS (open arrows) and VLBI (solid arrows) estimates of station velocities, shown with respect to the combined GPS+VLBI velocity solution (ellipses without arrows), in which no ties were imposed between the VLBI and GPS stations in California, except at Mojave. Ellipses as in Figure A5.

antenna set on a tripod above a ground monument (NCMN 1983 RM 1, which we designate MOJ1). From November 1986 to July 1988 (experiments 1–11), a TI 4100 antenna was mounted on the corner of the office building. In July 1988, it was replaced by a FRPA-2 antenna (MOJF), which was used for experiment 14. In February 1989, a MiniMac receiver and antenna were installed nearby, and the TI observations were discontinued the following July. Our experiments in March and April 1989 (experiments 13–16) used both the TI/FRPA-2 and MiniMac observations. All subsequent experiments used only the MiniMac observations. Conventional or GPS surveys have been conducted by us, by the USGS, and by Bendix Field Engineering, and all have formal uncertainties of 10 mm or less. The differences among our estimates of the relative heights of each of the GPS antennas and the (fixed) VLBI antenna (in the sense GPS–VLBI), after applying the tie information are 19 mm for MOJ1, 52 mm for MOJA, 110 mm for MOJF, and 159 mm for MOJM, each with a (doubled) formal uncertainty of about 30 mm. If we exclude MOJF and MOJM from the comparison (and also JPL1, Monument Peak, and Santa Paula, which had only a few occupations), the mean difference (GPS–VLBI) in height for the California sites is 60 mm, with all of the values falling between 19 and 74 mm.

A similar consistent difference (approximately 60 ± 30 mm) is found for the height differences estimated for Platteville, the two sites at Algonquin, and the three GPS antennas used at Westford. This consistency suggests a systematic bias in our estimates of height for all of the California GPS experiments. This result is not surprising, given the limited coverage of the tracking network for these experiments and the fact that we did not constrain any of the height values. Estimates of height from the global GPS experiments do not show this bias. Two of the North American sites, Richmond and Yellowknife, as well as Kokee and the three European sites, have much larger inconsistencies (–340 to +143 mm). Most of these inconsistencies are probably due to the influence of orbital errors and a changing and sometimes weak network of continental- and global-scale GPS tracking stations. Nevertheless, we cannot rule out tie blunders in every case. For this reason we have taken a conservative approach and not applied vertical ties between VLBI and GPS antennas in either our coordinate or velocity solution.

Comparison with previous GPS and trilateration results. In January 1987 (experiment 3), we reoccupied a historical trilateration network spanning the Santa Barbara Channel to estimate strain accumulation by comparing line lengths determined by trilateration and by GPS [*Larsen*, 1991; *Larsen et al.*, 1993, here-

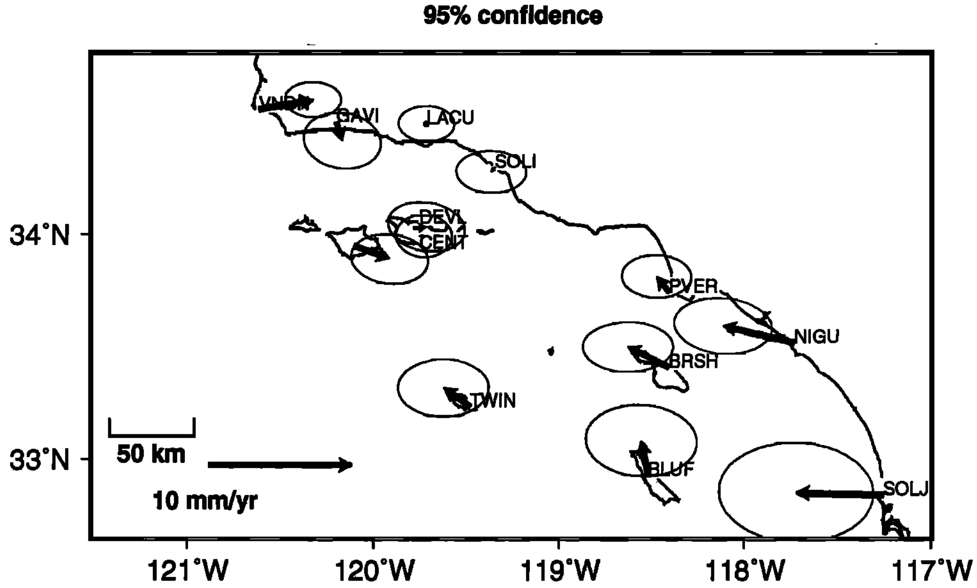

Fig. A7. Comparison of the velocity solution estimated in this study with that of LWL [*Larson and Webb*, 1992; *Larson*, this issue]. The plotted vectors are this study minus LWL, shown relative to LACU. We show 95% confidence ellipses from the LWL analysis to illustrate the relative sizes of the uncertainties for the sites. Correct confidence ellipses for the differences between the two analyses are difficult to compute because we cannot determine reliably the degree of independence of the estimates, which is a function of the data used and the a priori weight assumed for both data and parameters [*Dong*, 1993]. The two data sets differ by several GPS experiments, as well as all the VLBI data, as described in this appendix. We also use GPS data sampled every 30 s, rather than every 6 min, as used by LWL, but the effects of this difference are partially mitigated by our larger assumed measurement uncertainty and by correlations between the 30-s data samples.

after referred to as LAH]. This network was reoccupied again in 1991 (SB1), with results reported by *Larson and Webb* [1992] and *Larson* [this issue] (hereafter referred to as LWL). As part of their study, they present an independent analysis, using the GIPSY software developed at JPL [*Lichten and Border*, 1987; *Lichten*, 1990], of most of the data we collected at several of the core sites in the vicinity of the Santa Barbara Channel.

For the sites common to both studies, we calculate the differences between the velocities estimated by our joint GPS+VLBI velocity solution and that estimated by LWL using GPS data alone. In Figure A7, these differences are shown with respect to La Cumbre (LACU), near the center of the network of common stations. The difference in the north component is insignificantly different from zero with 95% confidence for all sites. For the east component, the difference is larger (3.8 mm/yr at the core station VNDN) and significant at four stations (VNDN, SOLJ, NIGU, and BRSH). The consistent sense of the difference in the east component (toward LACU in this plot) suggests the possibility of a systematic bias, which we attribute to problems in the reference frame adopted by LWL in their simpler, GPS-only strategy. The problem is most apparent at the "noncore" stations SOLJ, NIGU, and BRSH, for which both studies must rely heavily on a small number (3, 4, and 5, respectively) of occupations, including the early experiment 0 in 1986, when the number of global tracking stations was quite limited (Table 3 and *Larson et al.* [1991]). The most significant difference between the two strategies occurs at VNDN, a site where our data set is very different from the one used by LWL. At VNDN, our data set includes 150 VLBI experiments and 24 GPS occupations (in experiments 15, VF1, and VF2), which were not analyzed by LWL, while their data set includes seven USGS occupations of the MOJA-VNDN-OVRO triangle not included in our analysis.

While this sensitivity of velocity vectors to solution strategy is disturbingly large for regions as large as our entire network, the effects are less serious for relative velocities between neighboring stations, such as the lines spanning the Santa Barbara Channel. This can be seen by comparing the rate of change of distance dl/dt between stations for our GPS analysis for 1986–1992, for the GPS analysis of LWL for 1986–1991, and for the comparison of GPS measurements in 1987–1988 with trilateration measurements in 1970–1971 by LAH. Sites LACU and GAVI were common to all three studies, while two trilateration sites (DEVL and CHAF) have been tied to more convenient GPS sites within 5 km (CENT and SOLI, respectively). In our comparison, we assume that there is no motion between these pairs of stations.

The rates of change in line length for these three studies are presented in Table A3. While there is a hint of more east-west extension in the LWL results than in ours, there is no significant difference (at 90% confidence level) in dl/dt between the sites common to our and the LWL analysis. With three exceptions, there are no significant differences among the GPS–GPS and GPS–EDM line length changes. The discrepancies are for the lines DEVL–GAVI, where both our and the LWL results differ by more than two standard deviations from the LAH results, and DEVL–SNRI, where the LWL and LAH results differ. Because the GPS velocities for DEVL and SNRI, and the LAH results from GPS–EDM are all based on only two occupations, we hesitate to place much significance on these discrepancies.

That we estimate essentially the same rates in the two different intervals, with different techniques, increases our confidence in the stability of the benchmarks, as well as in our procedures for data reduction. It also suggests that the rate of deformation across the channel has not varied much over the last 20 years.

TABLE A3. Rates of Change in Line Length for the Santa Barbara Channel Estimated from GPS–GPS and GPS–Trilateration Comparisons

	dl/dt, mm/yr			Differences, mm/yr		
Line	GPS–GPS[a]	GPS–GPS[b]	GPS–EDM[c]	*c* – *a*	*c* – *b*	*a* – *b*
CENT–GAVI	0.9 ± 1.0	2.3 ± 1.3		3.7 ± 2.3	2.3 ± 2.5	–1.4 ± 1.6
DEVL–GAVI	–1.7 ± 1.1	–1.1 ± 1.5	4.6 ± 2.1	6.3 ± 2.4	5.7 ± 2.6	0.6 ± 1.9
CENT–LACU	–4.0 ± 0.6	–4.0 ± 1.0		–2.5 ± 1.8	–2.5 ± 2.0	0.0 ± 1.2
DEVL–LACU	–5.6 ± 0.9	–5.6 ± 1.2	–6.5 ± 1.7	–0.9 ± 1.9	–0.9 ± 2.1	0.0 ± 1.5
CENT–SOLI	–5.1 ± 1.0	–4.1 ± 1.5		0.0 ± 2.0	–1.0 ± 2.3	–1.0 ± 1.8
DEVL–SOLI	–4.1 ± 1.3	–2.3 ± 1.7	–5.1 ± 1.7	–1.0 ± 2.1	–2.8 ± 2.4	–1.8 ± 2.1
CENT–SNRI	2.2 ± 1.4	4.7 ± 1.7		–1.8 ± 1.8	–4.3 ± 2.0	–2.5 ± 2.2
DEVL–SNRI	0.4 ± 1.6	1.9 ± 1.9	0.4 ± 1.1	0.0 ± 1.9	–1.5 ± 2.2	–1.5 ± 2.5
LACU–SOLI	1.4 ± 0.8	1.6 ± 1.6	0.8 ± 1.4	–0.6 ± 1.6	–0.8 ±2.1	–0.2 ± 1.6
LACU–GAVI	0.6 ± 1.3	1.0 ± 1.2	0.4 ± 1.5	–0.2 ± 2.0	0.6 ± 1.9	–0.4 ± 1.8
SNRI–GAVI	–1.4 ± 1.1	–1.1 ± 1.2	4.3 ± 2.0	5.7 ± 2.3	5.4 ± 2.3	–0.3 ± 1.6
SNRI–LACU	–4.0 ± 1.2	–3.1 ± 1.3	–4.6 ± 2.3	–0.6 ± 2.6	–1.5 ± 2.6	–0.9 ± 1.8

[a] This study.
[b] *Larson and Webb* [1992].
[c] *Larsen et al.* [1993].

Acknowledgments. The global VLBI data used in our analysis were collected by the staffs of many observatories around the world and made available to us primarily through the efforts of the Goddard Space Flight Center of the National Aeronautics and Space Administration (NASA), the National Geodetic Survey (NGS) and Geodynamics Research Laboratory (GDL) of National Oceanic and Atmospheric Administration (NOAA), and the U.S. Naval Observatory (USNO). The global GPS observations were made available primarily through the efforts of GDL and the Canadian Centre for Surveying. The establishment in early 1987 of our core GPS network was made possible by collaboration offered by Will Prescott of the U.S. Geological Survey (USGS) and Bill Strange of NGS. Most of the California GPS measurements were made by the authors with invaluable assistance from our colleagues, including but not limited to Rob Clayton, Olafur Gundmundsson, Ken Hudnut, Dave Johnson, Louise Kellog, Scott King, Leslie Sonder, Hong-Kie Thio, and Bruce Worden (Caltech); John Goff and Peter Puster (MIT); Jeff Genrich, Glen Sasagawa, Catherine Hedlin, Michael Hedlin, Hadley Johnson, Nancy King (Scripps); Abe Cheng, Peng Fang, Bob Ge, Manabu Hashimoto, Naoshi Hirata, Mercedes Kim, and Li-Yu Sung (UCLA); James Stowell and Bruce Stephens (UNAVCO). We thank the understanding landowners, including the late Carey Stanton, the Nature Conservancy, and many others, for allowing us to access the bench marks on their property. The maps in the figures of this paper were generated using the public domain Generic Mapping Tools (GMT) software [*Wessel and Smith*, 1991]. This research was sponsored primarily by the National Science Foundation (grants EAR-86-18165, EAR-86-18393, EAR-86-18513, EAR-86-18542, EAR-92-08447) with supplementary funding from the NASA Crustal Dynamics Project (grants NAG5-447, NAG5-459, NAG5-538, NAG5-737, NAG5-842, NAG5-905, NAG5-1917, NAGW-2133, NAGW-2641), the U.S. Geological Survey (14-08-0001-G1673, 14-08-0001-G1950, 1434-92-G2185, 14-34-92-G2196), the Southern California Earthquake Center (USGS Cooperative Agreement 14-08-000001-A-0899), and the Air Force Office of Scientific Research (grants AFOSR-89-0400 and AFOSR-90-0339). Kurt Feigl was supported by an NSF Graduate Fellowship and an Air Force Laboratory Graduate Student Fellowship. Mark Murray and Kristine Larson were supported in part by NASA Graduate Student Fellowships. This is paper 38 of the Southern California Earthquake Center.

REFERENCES

Argus, D. F., and R. G. Gordon, Pacific-North American plate motion from very long baseline interferometry compared with motion inferred from magnetic anomalies, transform faults, and earthquake slip vectors, *J. Geophys. Res.*, *95*, 17,315–17,324, 1990.

Argus, D. F., and R. G. Gordon, Current Sierra Nevada-North America motion from very long baseline interferometry: implications for the kinematics of the western United States, *Geology*, *19*, 1085-1088, 1991.

Atwater, T., Implications of plate tectonics for the Cenozoic evolution of western North America, *Geol. Soc. Am. Bull.*, *81*, 3513–3536, 1970.

Bent, A. L., and D. Helmberger, Seismic characteristics of earthquakes along the offshore extension of the Western Transverse Ranges, California, *Bull. Seismol. Soc. Am.*, *81*, 399–422, 1991.

Bird, P., and R. W. Rosenstock, Kinematics of present crust and mantle flow in southern California, *Geol. Soc. Am. Bull.*, *95*, 946–957, 1984.

Blewitt, G., Carrier-phase ambiguity resolution for the Global Positioning System applied to geodetic baselines up to 2000 km, *J. Geophys. Res.*, *94*, 10,187–10,203, 1989.

Blewitt, G., M. B. Heflin, F. H. Webb, U. J. Lindquister, and R. P. Malla, Global coordinates with centimeter accuracy in the International Terrestrial Reference Frame using GPS, *Geophys. Res. Lett.*, *19*, 853–856, 1992.

Blewitt, G., M. B. Heflin, K. J. Hurst, D. C. Jefferson, F. H. Webb, and J. F. Zumberge, Absolute far-field displacements from the 28 June 1992 Landers earthquake sequence, *Nature*, *361*, 340–342, 1993.

Bock, Y., Continuous monitoring of crustal deformation, *GPS World*, 40–47, June, 1991.

Bock, Y., and S. Shimada, Continuously monitoring GPS networks for deformation measurements, in *Global Positioning System: An Overview, Proceedings of the International Association of Geodesy Symposium 102*, edited by Y. Bock and N. Leppard, pp. 40–56, Springer-Verlag, New York, 1990.

Bock, Y., S. A. Gourevitch, C. C. Counselman III, R. W. King, and R. I. Abbot, Interferometric analysis of GPS phase observations, *Manus. Geod.*, *11*, 282–288, 1986.

Bock, Y., D. C. Agnew, P. Fang, J. F. Genrich, B. H. Hager, T. A. Herring, K. W. Hudnut, R. W. King, S. Larsen, J. B. Minster, K. Stark, S.

Wdnowski, and F. K. Wyatt, Detection of crustal deformation from the Landers earthquake using continuous geodetic measurements, *Nature*, *361*, 337-340, 1993.

Bowie, W., Earth movements in California, *Spec. Publ. No. 106*, U.S. Coast and Geod. Survey, 1924. (Reprinted in *Reports on Geodetic Measurements of Crustal Movement, 1906–71* U.S. National Geodetic Survey, Rockville, Md., 1973.)

Bowie, W., Comparison of old and new triangulation data in California, *U. S. Coast and Geodetic Survey Spec. Publication No. 151*, 1928. Reprinted in *Reports on Geodetic Measurements of Crustal Movement, 1906–71*, U. S. National Geodetic Survey, Rockville, MD, 1973.

Burford, R. O., and P. W. Harsh, Slip on the San Andreas fault in central California from alinement arrays, *Bull. Seismol. Soc. Am.*, *70*, 1233–1261, 1980.

California Division of Mines and Geology, Preliminary fault activity map of California, Calif. Dep. of Conserv., Sacramento, 1992.

Callaway, D. C., Petroleum potential of the San Joaquin Basin, California, in *Future Petroleum Provinces of the United States: Their Geology and Potential*, edited by I. H. Crum, vol. 1, pp. 239–253, American Association of Petroleum Geologists, Tulsa, Okla., 1971.

Cande, S. C., and D. V. Kent, A new geomagnetic polarity time scale for the late Cretaceous and Cenozoic, *J. Geophys. Res.*, *97*, 13,917–13,951, 1992.

Carter, W. E., D. S. Robertson, and J. R. MacKay, Geodetic radio interferometric surveying: Applications and results, *J. Geophys. Res.*, *90*, 4577–4588, 1985.

Cheng, A., D. D. Jackson, and M. Matsu'ura, Aseismic crustal deformation in the Transverse Ranges of southern California, *Tectonophysics*, *144*, 159–180, 1987.

Clark, M. M., et al., Preliminary slip-rate table and map of late Quaternary faults of California, *U. S. Geol. Surv. Open File Report 84-106*, 1984.

Clark, T. A., et al., Precision geodesy using the Mark III very-long-baseline interferometry system, *IEEE Trans. Geosci. Remote Sens.*, *GE-23*, 438–449, 1985.

Clark, T. A., D. Gordon, W. E. Himwich, C. Ma, A. Mallama, and J. W. Ryan, Determinations of relative site motions in the western United States using Mark III very long baseline interferometry, *J. Geophys. Res.*, *92*, 12,741–12,750, 1987.

Clark, T. A., C. Ma, J. M. Sauber, J. W. Ryan, D. Gordon, D. B. Shaffer, D. S. Caprette, and N. R. Vandenberg, Geodetic measurement of deformation in the Loma Prieta, California earthquake with very long baseline interferometry, *Geophys. Res. Lett.*, *17*, 2015–2018, 1990.

Coates, R. J., H. Frey, J. Bosworth, and G. D. Mead, Space age geodesy: The NASA crustal dynamics project, *IEEE Trans. Geosci. Remote Sens.*, *GE-23*, 358–368, 1985.

Crouch, J. K., S. B. Bachman, and J. T. Shay, Post-Miocene compressional tectonics along the central California margin, in *Tectonics and Sedimentation Along the California Margin*, *Publ. 38*, edited by J. K. Crouch and S. B. Bachman, pp. 37–54, Pacific Section, Society of Economic Paleontologists and Mineralogists, Bakersfield, Calif., 1984.

Davis, J. C., *Statistics and Data Analysis in Geology*, 2nd ed., 646 pp., John Wiley, New York, 1986.

Davis, J. L., W. H. Prescott, J. L. Svarc, and K. J. Wendt, Assessment of Global Positioning System measurements for studies of crustal deformation, *J. Geophys. Res.*, *94*, 13,363–13,650, 1989.

Davis, T. L., J. Namson, and R. F. Yerkes, A cross section of the Los Angeles area: Seismically active fold and thrust belt, the 1987 Whittier Narrows earthquake and earthquake hazard, *J. Geophys. Res.*, *94*, 9644–9664, 1989.

Dehlinger, P., and B. A. Bolt, Earthquakes and associated tectonics in a part of coastal central California, *Bull. Seismol. Soc. Am.*, *77*, 2056–2073, 1988.

DeMets, C., R. G. Gordon, D. F. Argus, and S. Stein, Current plate motions, *Geophys. J. Int.*, *101*, 425–478, 1990.

Dibblee, T. W., Jr., The Rinconada and related faults in the southern Coast Ranges, California, and their tectonic significance, *U.S. Geol. Surv. Prof. Pap.*, *81*, 1977.

Dixon, T. H., An introduction to the Global Positioning System and some geological applications, *Rev. Geophys.*, *29*, 249–276, 1991.

Dixon, T., G. Blewitt, K. Larson, D. Agnew, B. Hager, P. Kroger, L. Skrumeda, and W. Strange, GPS measurements of regional deformation in California: Some constraints on performance, *Eos Trans. AGU*, *71*, 1051–1056, 1990.

Dokka, R. K., and C. J. Travis, Late Cenozoic strike-slip faulting in the Mojave desert, California, *Tectonics*, *9*, 311–340, 1990a.

Dokka, R. K., and C. J. Travis, Role of Eastern California Shear Zone in accommodating Pacific-North American plate motion, *Geophys. Res. Lett.*, *17*, 1323–1326, 1990b.

Dong, D, The horizontal velocity field in southern California from a combination of terrestrial and space-geodetic data, Ph.D. thesis, 157 pp., Mass. Inst. of Technol., Cambridge, 1993.

Dong, D. N., and Y. Bock, Global Positioning System network analysis with phase ambiguity resolution applied to crustal deformation studies in California, *J. Geophys. Res.*, *94*, 3949–3966, 1989.

Donnellan, A., A geodetic study of crustal deformation in the Ventura Basin region, southern California, Ph. D. thesis, 220 pp., Calif. Inst. of Technol., Pasadena, 1992.

Donnellan, A., B. H. Hager, R. W. King, and Thomas A. Herring, Geodetic measurement of deformation in the Ventura Basin region, southern California. *J. Geophys. Res.*, this issue.

Donnellan, A., B. H. Hager, and R. W. King, Revision of geologic rates in the Ventura Basin from space geodetic measurements, *Nature*, in press, 1993.

Eberhart-Phillips, D., M. Lisowski, and M. D. Zoback, Crustal strain near the Big Bend of the San Andreas fault: Analysis of the Los Padres-Tehachapi trilateration networks, California, *J. Geophys. Res.*, *95*, 1139–1153, 1990.

Ekström, G., and P. England, Seismic strain rates in regions of distributed continental deformation, *J. Geophys. Res.*, *94*, 10,231–10,257, 1989.

Ellsworth, W. L., Earthquake history, 1769-1989, in The San Andreas Fault System, edited by R. E. Wallace, *U. S. Geol. Surv. Prof. Pap. 1515*, 1990.

Feigl, K. L., Geodetic measurement of tectonic deformation in central California, Ph.D. thesis, 222 pp., Mass. Inst. of Technol., Cambridge, 1991.

Feigl, K. L., R. W. King, and T. H. Jordan, Geodetic measurement of tectonic deformation in the Santa Maria fold and thrust belt, California, *J. Geophys. Res.*, *95*, 2679–2699, 1990.

Feigl, K. L., R. W. King, T. A. Herring, and M. Rothacher, A scheme for reducing the effect of Selective availability on precise GPS carrier phase measurements, *Geophys. Res. Lett.*, *18*, 1289–1292, 1991.

Gold, C. M., Automated contour mapping using triangular element data structures and an interpolant over each irregular domain, *Comput. Graphics*, *11*, 170–175, 1975.

Hager, B. H., R. W. King, and M. H. Murray, Measurement of crustal deformation using the Global Positioning System, *Annu. Rev. Earth Planet. Sci.*, *19*, 351–382, 1991.

Hall, C. A., Jr., Origin and development of the Lompoc-Santa Maria pull apart basin and its relation to the San Simeon-Hosgri strike slip, western California, *Spec. Rep. Calif. Div. Mines and Geol.*, *137*, 1978.

Hall, C. A., Jr., San Luis Obispo transform fault and middle Miocene rotation of the western Transverse Ranges, California, *J. Geophys. Res.*, *86*, 1015–1031, 1981.

Harland, W. B., A. V. Cox, P. G. Llewellyn, C. A. G. Pickton, A. G. Smith, and R. Walters, *A Geologic Time Scale*, Cambridge University Press, New York, 1982.

Harris, R. A., and P. Segall, Detection of a locked zone at depth on the Parkfield California segment of the San Andreas fault, *J. Geophys. Res.*, *92*, 7945–7962, 1987.

Hauksson, E., and L. M. Jones, The July 1986 Oceanside earthquake sequence in the continental borderland, southern California, *Bull. Seismol. Soc. Am.*, *78*, 1885–1905, 1988.

Hauksson, E., et al., The 1987 Whittier Narrows earthquake in the Los Angeles metropolitan area, *Science*, *239*, 1409–1412, 1988.

Herring, T. A., GLOBK: Global Kalman filter VLBI and GPS analysis program version 3.1, Mass. Inst. of Technol., Cambridge, 1993.

Herring, T. A., et al., Geodesy by radio interferometry: Intercontinental distance determination with subdecimeter precision, *J. Geophys. Res.*, *86*, 1647–1651, 1981.

Herring, T. A., et al., Geodesy by radio interferometry: Evidence for contemporary plate motion, *J. Geophys. Res.*, *91*, 8341–8347, 1986.

Herring, T. A., J. L. Davis, and I. I. Shapiro, Geodesy by radio astronomy: the application of Kalman filtering to very long baseline interferometry, *J. Geophys. Res.*, *95*, 12,561–12,581, 1990.

Herring, T. A., D. Dong, and R. W. King, Sub-milliarcsecond determination of pole position using Global Positioning System data, *Geophys. Res. Lett.*, *18*, 1893–1896, 1991.

Hilgen, F. J., Extension of the astronomically calibrated (polarity) time scale to the Miocene/Pliocene boundary, *Earth Planet. Sci. Lett.*, *107*, 349–368, 1991.

Hornafius, J. S., B. P. Luyendyk, R. R. Terres, and M. J. Kamerling, Timing and extent of Neogene tectonic rotation in the western Transverse Ranges, California, *Geol. Soc. Am. Bull.*, *97*, 1476–1487, 1986.

Hudnut, K., J. Canias, L. Cotton, D. Jackson, R. Packard, R. Smith, G. Tayner, and W. Young, The southern California inter-county GPS project (abstract), *Eos Trans. AGU*, *72* (44), Fall Meeting suppl., 115, 1991.

Hutton, L. K., L. M. Jones, E. Hauksson, and D. D. Given, Seismotectonics of southern California, in *Neotectonics of North America Decade Map Volume 1*, edited by D. B. Slemmons, E. R. Engdahl, M. D. Zoback, and D. D. Blackwell, pp. 133–152, Geological Society of America, Boulder, Colo., 1991.

Jackson, J., and P. Molnar, Active faulting and block rotations in the western Transverse Ranges, California, *J. Geophys. Res.*, *95*, 22073–22087, 1990. (Correction, *J. Geophys. Res.*, *96*, 2203, 1991.)

Kanamori, H., and K. Satake, Broadband study of the 1989 Loma Prieta earthquake, *Geophys. Res. Lett.*, *17*, 1179–1182, 1990.

King, N. E., P. Segall, and W. Prescott, Geodetic measurements near Parkfield, California, 1959–1984, *J. Geophys. Res.*, *92*, 2727–2766, 1987.

King, R. W., and Y. Bock, Documentation for the MIT GPS analysis software: GAMIT, Mass. Inst. of Technol., Cambridge, 1993.

Larsen, S., Crustal deformation in southern California, Ph. D. thesis, 351 pp., Calif. Inst. of Technol., Pasadena, 1991.

Larsen, S. C., D. C. Agnew, and B. H. Hager, Strain accumulation in the Santa Barbara Channel: 1970–1988, *J. Geophys. Res.*, *98*, 2119–2134, 1993.

Larson, K. M., Precision, accuracy, and tectonics from the Global Positioning System, Ph.D. thesis, 269 pp., Univ. of Calif., San Diego, 1990a.

Larson, K. M., Evaluation of GPS estimates of relative positions from central California, 1986–1988, *Geophys. Res. Lett.*, *17*, 2433–2436, 1990b.

Larson, K. M., Application of the Global Positioning System to crustal defomation measurement, 3, Results from the southern California borderlands, *J. Geophys. Res.*, this issue.

Larson, K. M., and D. C. Agnew, Application of the Global Positioning System to crustal deformation measurement, 1, Precision and accuracy, *J. Geophys. Res.*, *96*, 16,547–16,565, 1991.

Larson, K. M., and F. H. Webb, Deformation in the Santa Barbara Channel from GPS measurements 1987-1991, *Geophys. Res. Lett.*, *19*, 1491–1494, 1992.

Larson, K. M., F. H. Webb, and D. C. Agnew, Application of the Global Positioning System to crustal deformation measurement, 2, The influence of errors in orbit determination networks, *J. Geophys. Res.*, *96*, 16,567–16,584, 1991.

Legg, M. R., V. Wong, and F. Saurez, Geologic structure and tectonics of the inner continental borderland of northern Baja California, in *The Gulf and Peninsular Province of the Californias*, edited by J. P. Dauphin and B. R. T. Simoneit, *AAPG Mem. 47*, Tulsa, Okla., 1989.

Lerch, F. J., S. M. Klosko, G. B. Patel, and C. A. Wagner, A gravity model for crustal dynamics (GEM-L2), *J. Geophys. Res.*, *90*, 9301–9311, 1985.

Li, V. C., and J. R. Rice, Crustal deformation in great Californian earthquake cycles, *J. Geophys. Res.*, *92*, 11,533–11,551, 1987.

Lichten, S. M., Estimation and filtering for high precision GPS applications, *Manuscr. Geod.*, *15*, 159-176, 1990.

Lichten, S. M., and J. S. Border, Strategies for high-precision Global Positioning System orbit determination, *J. Geophys. Res.*, *92*, 12,741–12,762, 1987.

Lindqwister, U. J., G. Blewitt, J. Zumberge, and F. Webb, Few millimeter precision for baselines in the California permanent GPS geodetic Array, *Geophys. Res. Lett.*, *18*, 1135–1138, 1991.

Lisowski, M., W. H. Prescott, J. C. Savage, and M. L. Johnston, Geodetic estimate of coseismic slip during the 1989 Loma Prieta, California, earthquake, *Geophys. Res. Lett.*, *17*, 1437–1440, 1990.

Lisowski, M., J. C. Savage, and W. H. Prescott, The velocity field along the San Andreas Fault in central and southern California, *J. Geophys. Res.*, *93*, 8369–8389, 1991.

Luyendyk, B. P., A model for Neogene crustal rotations, transtension, and transpression in southern California, *Geol. Soc. Amer. Bull.*, *103*, 1528-1536, 1991.

Malvern, L. E., *Introduction to Mechanics of a Continuous Medium*, 713 pp., Prentice–Hall, Englewood Cliffs, N.J., 1969.

McDougall, I., F. H. Brown, T. E. Cerling, and J. W. Hillhouse, A reappraisal of the geomagnetic polarity time scale to 4 Ma using data from the Turkana Basin, East Africa, *Geophys. Res. Lett.*, *19*, 2349–2352, 1992.

Minster, J. B., and T. H. Jordan, Vector constraints on Quaternary deformation of the western United States east and west of the San Andreas fault, *Tectonics and Sedimentation Along the California Margin*, *Publ. 38*, edited by J. K. Crouch and S. B. Bachman, pp. 1–16, Pacific Section, Society of Economic Paleontologists and Mineralogists, Bakersfield, Calif., 1984.

Minster, J. B., and T. H. Jordan, Vector constraints on western U.S. deformations from space geodesy, neotectonics and plate motions, *J. Geophys. Res.* *92*, 4798–4804, 1987.

Mount, V., and J. Suppe, State of stress near the San Andreas fault: Implications for wrench tectonics, *Geology*, *15*, 1143–1146, 1987.

Murray, M. H., Global Positioning System measurements of crustal deformation in central California, Ph.D. thesis, 310 pp., Mass. Inst. of Technol., Cambridge, 1991.

Namson, J., and T. Davis, Structural transect of the western Transverse Ranges, California: Implications for lithospheric kinematics and seismic risk evaluation, *Geology*, *16*, 675–679, 1988.

Namson, J., and T. L. Davis, Late Cenozoic fold and thrust belt of the southern Coast Ranges and Santa Maria Basin, California, *AAPG Bull.*, *74*, 467–492, 1990.

Okada, Y., Surface deformation to shear and tensile faults in a half-space, *Bull. Seismol. Soc. Am.*, *75*, 1135–1154, 1985.

Pacific Gas and Electric Company, Final Report of the Diablo Canyon Long-Term Safety Program for the Diablo Canyon Power Plant, Docket numbers 50-275 and 50-323, submitted to the Nuclear Regulatory Commission, San Francisco, 1988.

Pacheco, J., and J. Nábělek, Source mechanisms of three moderate California earthquakes of July 1986, *Bull. Seismol. Soc. Am.*, *78*, 1907–1929, 1988.

Page, B. M., Geology of the Coast Range of California, *Bull. Calif. Div. Mines Geol.*, *90*, 255–276, 1966.

Page, B. M., The southern Coast Ranges, in *The Geotectonic Development of California*, edited by W. G. Ernst, pp. 329–417, Prentice Hall, Englewood Cliffs, N.J., 1981.

Prescott, W. H., J. C. Savage, and W. T. Kinoshita, Strain accumulation in the western United States between 1970 and 1978, *J. Geophys. Res.*, *84*, 5423–5435, 1979.

Ryan, J. W., C. Ma, and D. S. Caprett, NASA Space Geodesy Program—GSFC Data Analysis—1992: Final report of the Crustal Dynamics Project VLBI Geodetic Results 1979–91, *Rep.104572*, NASA, Washington, DC., 1993.

Saastamoinen, J., Atmospheric correction for the troposphere and the stratosphere in radio ranging of satellites, in *The Use of Artificial Satellites for Geodesy*, *Geophys. Monogr. Ser.*, vol. 15, edited by S. W. Henriksen, A. Mancini, and B. H. Chovitz, pp. 247–251, AGU, Washington, D. C., 1972.

Sauber, J., Geodetic measurement of deformation in California, Ph.D. thesis, Mass. Inst. of Technol., Cambridge, 211 pp., 1988.

Savage, J. C., Equivalent strike-slip earthquake cycles in half-space and lithosphere-asthenosphere Earth models, *J. Geophys. Res.*, *95*, 4873–4879, 1990.

Savage, J. C., and R. O. Burford, Geodetic determination of relative plate motion in central California, *J. Geophys. Res.*, *78*, 832–845, 1973.

Savage, J. C., and W. H. Prescott, Geodetic control and the 1927 Lompoc, California Earthquake, *Bull. Seismol. Soc. Am.*, *68*, 1699–1703, 1978.

Savage, J. C., M. Lisowski, and W. H. Prescott, An apparent shear zone trending north-northwest across the Mojave desert into Owens Valley, eastern California, *Geophys. Res. Lett.*, *17*, 2113–2116, 1990.

Schaffrin, B., and Y. Bock, A unified scheme for processing GPS phase observations, *Bull. Géod.*, *62*, 142–160, 1988.

Scotti, O., A. Nur, and R. Estevez, Distributed deformation and block rotation in three dimensions, *J. Geophys. Res.*, *96*, 12,225–12,243, 1991.

Segall, P., and M. V. Matthews, Displacement calculations from geodetic data and the testing of geophysical deformation models, *J. Geophys. Res.*, *93*, 14,954–14,966, 1988.

Shaw, J. H., and J. Suppe, Slip rates on active blind thrust faults in the Santa Barbara Channel, Western Transverse Ranges Fold and Thrust Belt (abstract), *Eos, Trans. Amer. Geophys. Un.*, 72 (44), Fall Meeting Suppl., 443, 1991.

Shen, Z., Regional tectonic deformation in southern California, inferred from terrestrial geodesy and the Global Positioning System, Ph. D. thesis, 163 pp., Univ. Calif., Los Angeles, 1991.

Shen, Z. K., and D. D. Jackson, Global Positioning System reoccupation of early trilateration sites: tectonic deformation of the Southern Coast Ranges, *J. Geophys. Res.*, *98*, 9931–9946, 1993.

Shen, Z. K., Ge, B. X., and D. D. Jackson, Los Angeles Basin Tectonics and the 1991 Sierra Madre Earthquake (abstract), *Eos Trans. AGU, 72* (44), Fall Meeting suppl., 119, 1991.

Sieh, K. E., and R. H. Jahns, Holocene activity of the San Andreas fault at Wallace Creek, *Geol. Soc. Am. Bull.*, *95*, 883–896, 1984.

Sieh, K., et al., Near-field investigations of the Landers earthquake sequence, April to July, 1992, *Science*, *260*, 171–176, 1993.

Snay, R. A., M. W. Cline, and E. L. Timmerman, Regional deformation of the Earth model for the San Diego Region, California, *J. Geophys. Res.* *88*, 5009–5024, 1983.

Snay, R. A., M. W. Cline, and E. L. Timmerman, Horizontal crustal deformation models for California from historical geodetic data, *R. S.oc. N. Z. Bull.*, *24*, 131-140, 1986.

Snay, R. A., M. W. Cline, and E. L. Timmerman, Project REDEAM: Models for historical horizontal deformation, *NOAA Tech. Rep. NOS 125 NGS 42*, 1987.

Stein, R. S., and G. C. P. King, Seismic potential revealed by surface folding: 1983 Coalinga, California earthquake, *Science*, *224*, 869–872, 1984.

Stein, R. S., and R. S. Yeats, Hidden earthquakes, *Sci. Am.*, *260* (6), 48–57, 1989.

Sylvester, A. G., and A. C. Darrow, Structure and neotectonics of the western Santa Ynez fault system in southern California, *Tectonophysics*, *52*, 389–405, 1979.

Thatcher, W., Nonlinear strain buildup and the earthquake cycle on the San Andreas fault, *J. Geophys. Res.*, *88*, 5893–5902, 1983.

U.S. Geological Survey Staff, The Loma Prieta, California, earthquake: An anticipated event, *Science*, *247*, 286-293, 1990.

Ward, S. N., Pacific-North America plate motions: New results from very long baseline interferometry, *J. Geophys. Res.*, *95*, 21,965–21,981, 1990.

Watson, D. F., ACORD: Automatic contouring of raw data, *Comput. Geosci.*, *8*, 97–101, 1982.

Webb, F. H., Geodetic measurement of deformation in the offshore of southern California, Ph.D. thesis, 211 pp., Calif. Inst. of Technol., Pasadena, 1991.

Weldon, R., and E. Humphreys, A kinematic model of southern California, *Tectonics*, *5*, 33–48, 1986.

Wessel, P., and W. H. F. Smith, Free software helps map and display data, *Eos, Trans. AGU*, *72*, 441, 1991.

Whitten, C. A., Crustal movement in California and Nevada, *Eos Trans. Am. Geophys. Union*, *37*, 1956. (Reprinted in *Reports on Geodetic Measurements of Crustal Movement, 1906-71* U. S. National Geodetic Survey, Rockville, Md., 1973.)

Yeats, R. S., Quaternary flake tectonics of the California Transverse Ranges, *Geology*, *9*, 16–20, 1981.

Yeats, R. S., Large-scale Quaternary detachments in Ventura Basin, California, *J. Geophys. Res.*, *88*, 569–583, 1983.

Yeats, R. S., and G. J. Huftile, Alternate model for convergence across the Ventura Basin, California, *Eos, Trans. AGU*, *73*, (43), Fall Meeting suppl., 590, 1992.

Yerkes, R. F., and W. H. K. Lee, Late Quaternary deformation in the Western Transverse Ranges, California, *U.S. Geol. Surv. Circ.*, *799B*, 1979.

Zoback, M. D., et al., New evidence on the state of stress of the San Andreas fault system, *Science*, *238*, 1105–1111, 1987.

D. C. Agnew and Y. Bock, Institute of Geophysics and Planetary Physics, Scripps Institution of Oceanography, La Jolla, CA 92093.

D. Dong, A. Donnellan, and F. H. Webb, Jet Propulsion Laboratory, 4800 Oak Grove Dr., Pasadena, CA 91109.

K. L. Feigl, UPR 234, Observatoire Midi Pyrénées, 14 Ave. E. Belin, 31400 Toulouse, France.

B. H. Hager, T. A. Herring, T. H. Jordan, and R. W. King, Department of Earth, Atmospheric and Planetary Sciences, 54-620, Massachusetts Institute of Technology, Cambridge, MA 02139.

D. D. Jackson and Z. Shen, Department of Earth and Space Sciences, University of California, Los Angeles, CA 90024.

S. Larsen, Lawrence Livermore National Laboratory, L 208, Livermore, CA 94550.

K. M. Larson, Department of Aerospace Engineering, University of Colorado, Campus Box 431, Boulder, CO 80309-0431.

M. H. Murray, US Geological Survey, 345 Middlefield Rd., Menlo Park, MS 977, CA 94025.

(Received December 18, 1992;
revised August 16, 1993;
accepted August 24, 1993.)